SAPIENZA
UNIVERSITÀ DI ROMA

Testing General Relativity with Gravitational Waves from Extreme Mass-Ratio Inspirals

Scuola di dottorato Vito Volterra
Dottorato di ricerca in fisica - XXXVI ciclo

Susanna Barsanti
ID number 1871899

Advisor
Prof. Andrea Maselli
Prof. Leonardo Gualtieri
Prof. Paolo Pani

Academic Year 2022/2023

Testing General Relativity with Gravitational Waves from Extreme Mass-Ratio Inspirals

Sapienza University of Rome

This thesis has been typeset by LaTeX and the Sapthesis class.

Author's email: susanna.barsanti@uniroma1.it

Contents

Abstract

Extreme Mass Ratio Inspirals (EMRIs) are asymmetric binary systems. They are composed of a massive black hole and a stellar mass compact object, which inspirals until the plunge, emitting gravitational waves (GWs) potentially observable by future space based detectors, such as the Laser Interferometer Space Antenna (LISA). In the final year before the plunge, EMRIs complete thousands of cycles in the strong-field region around the massive black hole. Tracking such large number of orbits would allow to measure the source parameters with exquisite accuracy, and to perform precise strong-field tests of gravity. Following such quest and exploiting the scientific potential of asymmetric binaries require accurate waveforms in modified theories of gravity, to compare against General Relativity (GR) predictions. Such models are currently missing, due to the complexity of calculations beyond GR.

In this thesis we provide a key step forward, and discuss the modelling of EMRIs when the gravitational interaction is mediated by additional fundamental fields. We develop a new theoretical framework able to describe the EMRI dynamical evolution in a vast class of modified theories of gravity with extra massless and massive scalar fields. Exploiting decoupling of scales we show how, at leading order in the binary mass ratio, deviations from GR for the massive BH can be neglected such that the background spacetime can be described by the Kerr metric. In this approach all information about the underlying gravity theory is encoded by the scalar charge of the inspiralling lighter body, and by the mass of the scalar field. These two parameters fully capture the imprint of the scalar field on the emitted gravitational waves. We perform an extensive data-analysis of mock GW signals emitted by asymmetric binaries, forecasting LISA ability to constrain the scalar field parameters. Our results show that EMRIs provide golden sources to probe the existence of new fundamental fields in the Universe.

Preface

List of publications

This doctoral thesis is the outcome of three years of studies at the Sapienza University of Rome, from November 2020 to October 2023. During these three years, two scientific visits were performed at the University of Nottingham, one of which was funded by the COST Action CA16104 within the Short Term Scientific Mission (STSM) program, to collaborate with Prof. Thomas P. Sotiriou.

As a result of my doctoral studies, different scientific papers have been published, focused on the theoretical modelling of asymmetric binaries, and in particular of Extreme Mass Ratio Inspirals (EMRIs), in gravity theories with additional scalar fields:

1. A. Maselli, N. Franchini, L. Gualtieri, T. P. Sotiriou, S. Barsanti, and P. Pani, "Detecting fundamental fields with LISA observations of gravitational waves from extreme mass-ratio inspirals", Nature Astron., vol. 6, no. 4, pp. 464–470, 2022. arXiv: 2106.11325 [gr-qc];

2. S. Barsanti, N. Franchini, L. Gualtieri, A. Maselli, and T. P. Sotiriou, "Extreme mass-ratio inspirals as probes of scalar fields: Eccentric equatorial orbits around Kerr black holes", Phys. Rev. D, vol. 106, no. 4, p. 044 029, 2022. arXiv: 2203.05003 [gr-qc];

3. S. Barsanti, A. Maselli, T. P. Sotiriou, and L. Gualtieri, "Detecting Massive Scalar Fields with Extreme Mass-Ratio Inspirals", Phys. Rev. Lett., vol. 131, no. 5, p. 051 401, 2023. arXiv: 2212.03888 [gr-qc].

The results of (1) are presented in Chapters 6 and 8, those of (2) are discussed in Chapter 7. Finally, the outcome of (3) is analysed in Chapter 9. Moreover, two papers are currently in preparation:

4. M. Della Rocca, S. Barsanti, *et al.*, "Extreme mass-ratio inspirals as probes of scalar fields: Inclined circular orbits around Kerr black holes", *in preparation* ;

5. L. Speri, S. Barsanti, *et al.*, "Fast EMRI Waveform to test General Relativity", *in preparation.*

The first one improves the adiabatic EMRI model by including the orbital inclination in the inspiral description, and focuses on circular inclined orbits around rotating black holes. The second one performs a fully Bayesian analysis on equatorial eccentric EMRIs around Kerr black holes and provides constraints for the detection of scalar fields.

Finally, a study concerning the detectability of subsolar-mass primordial black holes in EMRIs has been accomplished during a visit of Dr. Valerio De Luca at Sapienza University:

6. S. Barsanti, V. De Luca, A. Maselli, and P. Pani, "Detecting Subsolar-Mass Primordial Black Holes in Extreme Mass-Ratio Inspirals with LISA and Einstein Telescope", Phys. Rev. Lett., vol. 128, no. 11, p. 111 104, 2022. arXiv: 2109.02170 [gr-qc].

Since the focus of this thesis builds around the modeling of EMRIs in beyond-GR and beyond-SM scenarios, this work is not discussed here. However, we stress that the analysis carried out in (6) was performed, in a pure-GR context, exploiting the tools developed to modeling EMRIs with additional scalar fields. The results of (6) suggest that, if the EMRI secondary is a subsolar-mass object, its mass could be measured with a subpercent accuracy by future interferometers like LISA and the Einstein Telescope. This would allow to detect a subsolar-mass black hole with high statistical confidence, providing a smoking-gun signature of its primordial origin.

Conventions

In these thesis we use geometric units in which $G = 1 = c$, where G is the gravitational constant and c is the speed of light.

Introduction

Gravitational Waves (GWs) are spacetime perturbations which propagate at the speed of light and are predicted by General Relativity (GR), which provides so far the best description of gravitational phenomena. Gravitational waves interact weakly with ordinary matter, and their observation is naturally enhanced in astrophysical events evolving in the so called strong field gravity regime, as the coalescences of black holes (BHs) and neutron stars (NSs).

The first direct detection of GWs was performed in September 2015 by the ground based interferometer LIGO [1], and opened a new era of astronomical observations which now allows to investigate our Universe in synergy with electromagnetic probes. Tests of the Einstein theory in the most extreme regime of gravity stand as one of the most exciting opportunities offered by this new window.

Currently, direct detection of GWs is performed by the ground-based inferferometers LIGO-Virgo-KAGRA, which are sensitive to signals falling in the 1Hz-KHz band [2–7]. While such instruments are reaching their designed sensitivity, a 3rd generation of ground-detectors, such as the Einstein Telescope (ET) and Cosmic Explorer (CE), is under investigation, promising an improvement in the sensitivity of current instruments of more than an order of magnitude [8, 9]. To detect signals of lower frequencies, the future space mission Laser Interferometer Space Antenna (LISA) will be launched in the mid-2030s [10]. LISA will detect signals in the $(10^{-4} - 1)$Hz frequency range, which will allow to explore an entire new class of systems. Indeed, while ground-based detectors are able to detect objects from few to hundreds of solar masses, LISA will be sensible to larger masses, including among its targets sources as supermassive black hole binaries and asymmetric binary systems.

By analyzing the emission of GWs from BHs and NSs, such compact objects can be turned into cosmic laboratories to probe physics under extreme conditions, allowing for tests of the nature of gravity and of the rich phenomenology exhibited by fundamental fields and particles, and for search of new physics beyond GR and the Standard Model of Particle Physics (SM). Indeed, searches for new fundamental physics feature very prominently among the objectives of current and future detectors [11–13].

The opportunity offered by the quality of data expected from such astrophysical observatories, together with a series of long lasting problems like the existence of spacetime singularities, of dark matter and dark energy, and the non renomarmalization of GR in quantum field theory, has motivated the quest for alternative theories of gravity, which can be tested against General Relativity [14].

One of the easiest and most common ways to go beyond our current description of gravity (and of particle physics) consists in the addition of new fundamental scalar fields, that are ubiquitous in extensions of the Standard Model and General Relativity [15–17].

However, the detection of scalar fields by means of black holes carries some issues which deal with no-hair theorems. Indeed, not only no-hair theorems hold for stationary and asymptotically flat black holes in GR [18], dictating that the black hole's spacetime only depends on the three parameters given by the black hole's mass, spin and the (astrophysically negligible) electrical charge, but they can also hold for theories with additional scalar fields. No-scalar-hair theorems have been proven for most scalar-tensor theories, which means that the scalar must be trivial and that the black hole's spacetime is described by the Kerr metric [19–23]. Evading the no-hair theorems to obtain black hole solutions with scalar hair, i.e. black holes endowed with a non-trivial scalar profile so that they can be thought as carrying a scalar charge, requires coupling the scalar to higher-order curvature reforms [24–27]. The nature of these couplings then implies that the scalar charge per unit mass of a BH is inversely proportional to its mass to some positive power, so that the more massive a BH is, the more weakly charged it is [24–34]. This provides a powerful restriction for using, for example, observations of massive BHs by LISA and 3g detectors, to probe the existence of such new fields coupled to the gravity sector.

Given this general framework, a possibility to employ black holes for the detection of new scalar fields, circumventing the issues carried by no-hair theorems, is given by Extreme Mass Ratio Inspirals (EMRIs).

EMRIs are asymmetric binary systems in which a stellar mass compact object (SCO) inspirals into a massive black hole (MBH) until the plunge. In the final year before the plunge, the little object completes thousands of orbits in the strong-field region around the massive black hole. By moving on the background spacetime given by the central object, the SCO perturbs it giving rise to gravitational waves falling in the mHz frequency band, which will be explored by the future space based detector LISA. By tracking the continuously emitted waves with LISA, it will be eventually possible to build a precise map of the binary spacetime, recovering with exquisite accuracy the source parameters and in particular the MBH properties, allowing to test its Kerr nature. This renders EMRIs golden binaries to test deviations from GR [35].

From a theoretical point of view, asymmetric binaries can be studied with the well-known relativistic perturbation theory approach, considering expansions in the mass ratio of the binary [36–39]. At leading order, the inspiralling object can be treated as a point-particle moving on the background spacetime of the MBH, described by the Kerr metric, and the inspiral is adiabatically built through a sequence of geodesics. Next orders in the binary mass ratio take into account the finite-structure of the SCO and its interaction with its own perturbations, which lead to secular deviation in the inspiral from the adiabatic model. While first and second post-adiabatic corrections are necessary to provide accurate waveform for the LISA data analysis [40], their calculations provides a formidable task which has required decades of theoretical and numerical development. The first GR waveform model containing post-adiabatic corrections has been produced only recently [41–43].

The complexity of calculations beyond GR grows very fast, due to the introduction of the new fields, and their couplings with the tensor modes. As a results, the landscape of EMRI models in extended theories of gravity is almost virgin, with no waveform model available so far.

A framework to describe EMRIs in gravity theories with additional scalar fields have been proposed in [44]. In such work, it is shown how, to model systems with large mass asymmetry in gravity theories with new scalar fields, the scaling of the

scalar hair with the BH mass turns out to be a benefit. Indeed, in such systems, the massive black hole's scalar charge can be neglected with respect to that one of the small inspiralling body. At leading order in the mass ratio q, the scalar charge of the MBH is entirely suppressed, and the MBH spacetime can be simply described with the Kerr metric. Moreover, all the deviations from GR are fully controlled by the scalar charge of the SCO, which allows to model EMRIs in a theory-agnostic manner. The presence of scalar charge of the secondary causes an extra channel of binary's energy loss through scalar waves, that are added to the gravitational ones and modify the system's dynamics with respect to the GR predictions. Analysing the effect of the presence of the scalar charge on the EMRIs dynamics and consequently on the emitted GW signal constitutes the key for the detection of the extra scalar fields.

In this picture, by following the framework presented in [44], the aim of the thesis is twofold: (i) study how the inclusion of extra scalar fields affects the EMRI dynamics and GW emission, (ii) investigate how such changes can be detected by LISA and the constraints that can be inferred on the scalar field features.

First, we focused on modeling the adiabatic EMRI inspiral. In real astrophysical scenarios, EMRIs are expected to complete generic inclined, eccentric orbits around rapidly rotating MBH. Here we present the adiabatic EMRI model with massless scalar fields for equatorial circular and equatorial eccentric orbits around Kerr black holes. For each type of orbit, we computed the gravitational and scalar emission, we built the adiabatic inspirals and modeled the emitted GW signal with the quadrupolar approximation, computing the mismatch between signals emitted in the presence and in the absence of the scalar charge, in order to obtain a first insight into the detectability of the new field.

Secondly, we performed parameter estimations over the binary systems. We applied a Fisher Information Matrix (FIM) approach to equatorial circular inspirals around rotating black holes, providing the first forecast on the LISA ability to detect new scalar fields and measure the scalar charge carried by the secondary.

Finally, EMRIs with massive scalar fields have been investigated, performing a FIM for equatorial circular inspirals around Kerr black holes, in order to explore the detectability of both the scalar charge and the mass of the scalar field.

Our results suggest how Extreme Mass Ratio Inspirals represent extremely promising sources of gravitational waves for the future Laser Interferometer Space Antenna to probe the existence of new fundamental fields.

The thesis is organized as follows.

Chapter 1 focuses on gravitational waves detection, with a first section dedicated to current detections from ground-based interferometers, a second section focused to the future space mission LISA, and the last one to one of its main target, Extreme Mass Ratio Inspirals, presenting their astrophysical features and theoretical modeling.

In Chapter 2 we provide a brief description of the alternative theories of gravity, focusing on gravity theories with additional scalar fields.

Chapter 3 is dedicated to the Kerr metric, which describes the background spacetime of our EMRI model. We focus on the characterization of the geodesic structure of such metric, dedicating the Sections 3.1.1 and 3.1.2 and to equatorial circular and equatorial eccentric, respectively.

In Chapter 4 we present a description of the EMRI modeling in General Relativity, presenting the state-of-art achievements in such scenario, and then we present the EMRI description in gravity theories with a new real and massless scalar field.

In Chapter 5 we discuss the linear perturbations of a point-particle on a Kerr background. Both the scalar field and the gravitational field perturbations are considered, for a point particle moving on the two types of orbits: equatorial circular and equatorial eccentric.

Chapters 6 and 7 present the study of the adiabatic orbital evolution together with the emitted gravitational waves modeling, for equatorial circular and equatorial eccentric inspirals. In each chapter, the first section is dedicated to the gravitational and scalar emissions, the second one to the adiabatic orbital evolution, and the last one to the construction of the GW-templates with the computation of the mismatch between signals with and without the scalar charge, to asses its effect on the emitted signal.

In Chapter 8 is presented a parameter estimation with the Fisher Information Matrix analysis applied to equatorial circular inspiral around Kerr black holes, in order to forecast the measurability of the scalar charge carried by the secondary object.

Finally, Chapter 9 is dedicated to EMRIs with additional massive scalar fields. In Section 9.1, we present the theoretical framework of the model and in Section 9.2 the massive scalar linear perturbations. The results are presented in the following sections. Section 9.3 is dedicated to the energy fluxes and Section 9.4 to the adiabatic evolution for equatorial circular trajectories. Finally, the last two sections focus on the gravitational waves emission, presenting the mismatch among signals in the presence and in the absence of the new massive field, and finally performing the fisher analysis which provides a study of the simultaneous detectability of the scalar charge and mass.

Chapter 1

Gravitational wave detection: sources, instruments and goals

This chapter is dedicated to the detection of gravitational waves (GWs). In the first section, we present a brief overview of the current state of GW detection from the ground-based instruments LIGO-Virgo-KAGRA. In the following section, we focus on the future space based detector LISA. The last section is dedicated to one of the main target of the future interferometer: Extreme Mass Ratio Inspirals.

1.1 Gravitational waves and ground-based detectors

Gravitational waves are ripples of space-time, perturbations of the gravitational field which propagate at the speed of light. They are generated in a regime in which gravity is extreme, as that one sampled by the coalescence of compact objects as black holes and neutron stars, and predicted by General Relativity.

In order to directly detect gravitational waves, the first ground-based interferometers LIGO/Virgo were built. The first GW event was detected by LIGO in September 2015 and is associated to the merger of a binary of black holes [1]. Such detection opened the first Observing Run O1, which lasted from September 2015 to January 2016. From then to now, another three observing runs were performed: O2 from November 2016 to August 2017, O3a from April 2019 to October 2019 and O3b from November 2019 to March 2020, for a total of almost a hundred of GW detections [5–7]. The fourth Observing Run O4 started on May 2023 and is still ongoing [45]. Starting from the third observing run O3, the Japanese ground-based interferometer KAGRA has joined the LIGO/Virgo detectors [4].

The LIGO-Virgo-KAGRA collaboration can detect signals in the frequency range of 1Hz-KHz. While the LIGO/Virgo detectors are reaching their full sensitivity, a 3rd generation of detectors is planned, with the Einstein Telescope and the Cosmic Explorer, which will improve of more than an order of magnitude the sensitivity of current interferometers within the 1Hz-KHz band [8, 9].

The maximum frequency of the emitted GW is related to the masses of the binary system by $f_{\max} \sim 1/M_{\rm tot}$, with $M_{\rm tot}$ being the sum of the two component masses. Such relation is obtained by considering Kepler's third law for the binary system, $f_{\rm GW} \sim \sqrt{M_{\rm tot}/r^3}$ and the orbital radius of the merge of several M. Hence, for the frequency range of 1Hz-KHz, the ground-based instruments can detect binaries with masses from few to hundreds of solar masses.

A footage of the binary systems detected so far is presented in Fig.1.1, commonly known as the "Stellar Graveyard" [46], in which compact objects detected from both gravitational waves and electromagnetic (EM) emission are shown. The LIGO-Virgo-KAGRA detections are colored in blue/orange for the binary black holes/neutron stars detection, while the electromagnetic signals are colored in pink/yellow.

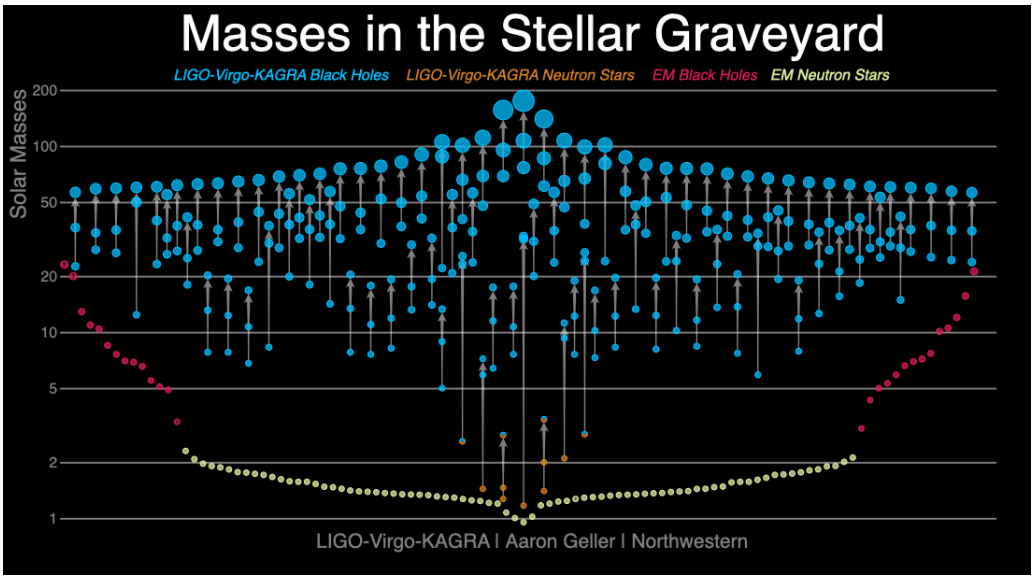

Figure 1.1. Sample of gravitational wave sources, detected with the LIGO-Virgo-KAGRA collaboration, and of electromagnetic sources. Credit: [46].

The component masses of the sources range within $\sim (1-100)M_\odot$. An observational gap however exists in the range between $\sim (2-5)M_\odot$. This gap is somehow expected since stellar formation predicts BHs masses $\gtrsim 5M_\odot$, with NSs in the range $\lesssim 3M_\odot$. Note however that some binary events detected so far by LIGO/Virgo/Kagra, with a low confidence level, may feature component masses right in this window [47].

A different theoretical mass gap is expected within $\sim (50-100)M_\odot$ due to pair-instability supernovae mechanism, which can hamper the formation of BHs in this range. For this reason, the recent observation of a binary merger with a remnant mas of $150M_\odot$ has raised considerable interest within the gravitational wave and astrophysical community [48, 49]. Such event could also provide a first hint for the existence of Intermediate Mass Black Holes (IMBHs).

In order to detect signals arising from more massive objects, i.e. emitting at lower frequencies, longer arms of the interferometers are needed, together with the avoidance of the terrestrial confusion noise. These requirements are at the base of space-born detectors.

The following section is dedicated to one of the planned future GW satellite, the Laser Interferometer Space Antenna.

1.2 The Laser Interferometer Space Antenna

The Laser Interferometer Space Antenna (LISA) is the ESA space mission planned for launch in the mid-2030s [50].

It consists in a GWs detector that will be launched in space and will follow the Earth in its orbit around the Sun. The space interferometer will have a triangular configuration, composed by three arms of 2.5 million kilometers and three identical spacecrafts in each vertex. In total, six active laser links will reflect between the three spacecrafts, inside which free falling test masses will be located and will act as mirrors reflecting the laser beam. Such configuration will allow to exploit the change in the time travel of the light-beam or the optical pathlenght of test masses which are induced by the passage of gravitational waves [10].

A depiction of the LISA orbit around the Earth is shown in Fig. 1.2.

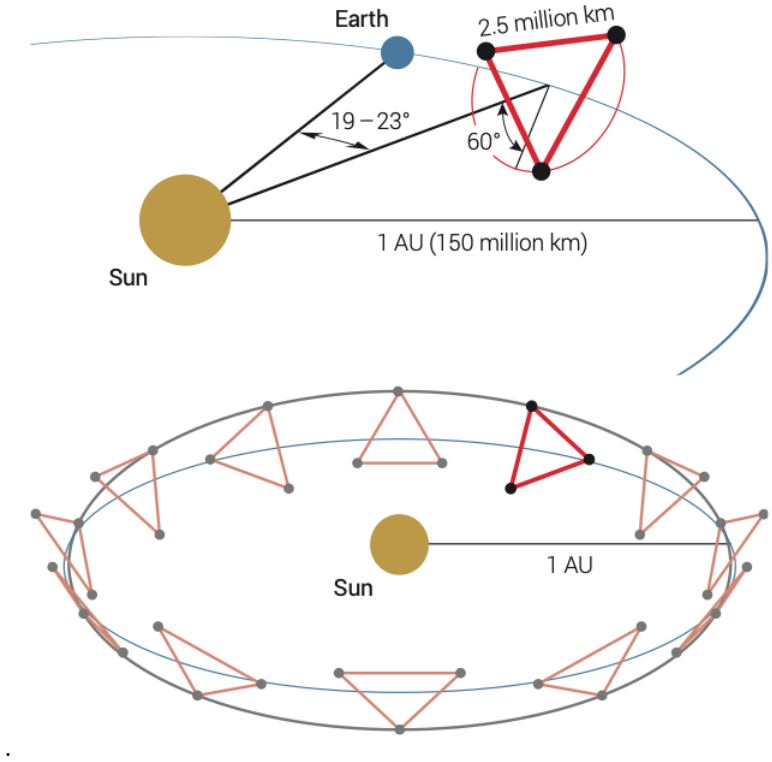

Figure 1.2. Description of the LISA orbit [10].

Flying between 50 and 65 million km from the Earth, it will scan the cosmos obtaining both polarisations of the GWs simultaneously. The length of the arms of the detector will allow to detect signals with frequencies in the $\sim (10^{-4}, 10^{-1})$ Hz range, complementary to that one of the ground based detectors. As previously mentioned, the maximum GW frequency is related to the total mass $M_{\rm tot}$ of the binary system by $f_{\rm max} \sim 1/M_{\rm tot}$, so that different frequencies mean different masses of the sources producing the waves. LISA will be the first space mission able to investigate such low frequency range and to explore the entire Universe through gravitational waves [51]. It will be able to detect signals from redshifts up to $z \sim 20$ and the loudest GWs originating from supermassive black hole binaries.

A classification of the sources that will be among the possible targets for LISA is given by [12, 52]:

- Supermassive Black Hole Binaries (SMBHBs): systems in which the mass ratio is larger than 10^{-1} and the total mass is in $(10^5, 10^7)M_\odot$;
- Intermediate-Mass Black Hole Binaries (IMBHBs): same as the SMBHBs but with total mass in $(10^2, 10^5)\,M_\odot$;
- Extreme Mass-Ratio Inspirals (EMRIs): binary sources with mass ratios in $(10^{-6}, 10^{-3})$ and total masses in $(10^3, 10^7)\,M_\odot$;
- Intermediate Mass-Ratio Inspirals (IMRIs): same as the EMRIs but with mass ratios in $(10^{-3}, 10^{-1})$;
- Stellar origin BH binaries: coalescences with sufficiently low total mass (e.g. in $(50, 500)M_\odot$) such that they could be detected both by LISA and second or third generation ground based detectors;
- Galactic Binaries: inspirals composed by white dwarfs or neutron stars within the Milky Way that produce nearly monochromatic signals;
- Stochastic Backgrounds: cosmological sources of GWs that produce a stochastic background.

Each kind of binary systems will emit GWs that will be possibly detected by the future space interferometer. A schematic representation of the characteristic strain of the emitted GW signal expected by the potential sources, together with the expected LISA sensitivity are reported in Fig.1.3 [10]. The grey shadowed area represents the confusion noise of millions of binaries, which forms the galactic background, for which the detected amplitude is modulated by the LISA motion over the year.

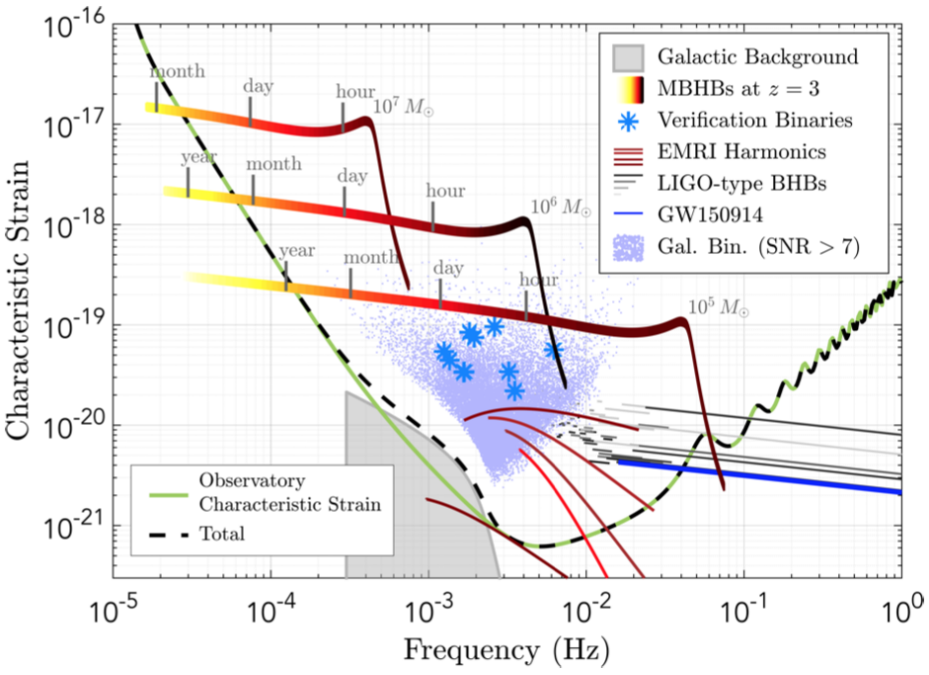

Figure 1.3. Representation of the characteristic strain of the potential LISA sources with the expected LISA sensitivity as a function of the frequency [10].

The detection of GWs coming from these sources will let us to investigate the most extreme strong-gravity regimes and to test the foundations of General Relativity, so that testing of new fundamental physics beyond GR and the Standard Model of Particle Physics is a crucial objective of the future space mission. In the following we report a classification of the different topics of the fundamental physics LISA science case, which are [12, 13]

- tests of General Relativity, probing the fundamental principles underlying GR and testing the Einstein theory by means of compact objects;
- tests of the nature of black holes, which main focus is to test the Kerr hypothesis through BHs in non-vacuum GR or Exotic Compact Objects (ECOs);
- Dark Matter and Primordial Black Holes (PBHs), focusing on two types of dark matter, i.e. new particles as axions and/or macroscopic objects as PBHs or ECOs;
- Dark energy and the ΛCDM model, focusing on cosmology test to probe the fundamental physics underlying the standard model of the Universe ΛCDM, with its extensions through dark energy and modified gravity theories;
- Other model independent tests, performing model-agnostic tests of GR;
- Astrophysical and waveform systematics, which focuses in the understanding of the error systematics from the GW modeling and from astrophysical and enivronmental effects.

In the next section, we will focus one of the main target sources of LISA, Extreme Mass Ratio Inspirals, while alternative gravity theories scenarios are left to the next chapter.

1.3 Asymmetric binaries: Extreme Mass-Ratio Inspirals

Extreme Mass Ratio Inspirals (EMRIs) are asymmetric binary systems in which the secondary is given by a stellar mass compact object (SCO), which can be a black hole, a neutron star or a white dwarf, and inspirals around the primary given by a massive black hole (MBH). Typical extreme mass ratios are $q = 10^{-3} - 10^{-6}$, where $q = m_p/M$ with $m_p \ll M$, and typical values of the component masses are $m_p = (1 - 10^2)M_\odot$ for the secondary and $M = (10^4 - 10^7)M_\odot$ for the primary.

Here we present an overview of the EMRI astrophysical characteristics and of the theoretical modeling commonly applied to such binaries.

1.3.1 Astrophysical features

Massive black holes are believed to exist at the center of most galaxies [53]. An evidence in this direction was recently given by the Event Horizon Telescope (EHT), which, in 2019 and in 2022, released the first images of two supermassive black holes, M87 and Sagittarius A*, residing respectively at the center of the M87 galaxy and of the Milky Way [54, 55]. Massive black holes are typically surrounded by a nuclear star cluster, so that Extreme Mass Ratio Inspirals form when a stellar compact object is captured from such cluster by the central MBH. From the capture, the secondary starts to inspirals around the primary in inclined, eccentric orbit and finally plunges into the MBH.

In the last year of inspiral before the plunge, the number of orbital cycles completed by the stellar mass compact object is $\sim 10^4 - 10^5$, most of which accumulate in the strong-field region of the central massive black hole [56]. During the evolution, the secondary perturbs the background spacetime of the MBH, giving rise to gravitational waves of typical frequencies lying in the mHz band, which will be possibly detected by the future space-based interferometer LISA. By tracking the continuously emitted GW signals, which encode the information of the EMRI orbit, it will be eventually possible to build a detailed map of the binary spacetime, recovering with exquisite accuracy the intrinsic source parameters, primarly determined by the GW phase. The intrinsic source parameters and their expected precision are [35]:

- redshifted component masses $M_z = (1+z)M$, with z being the redshift, with precision $\sim 10^{-6} - 10^{-4}$;
- dimensionless spin of the primary with precision $\sim 10^{-6} - 10^{-3}$.

The extrinsic parameters (luminosity distance and sky localisation) are primarily determined through the signal amplitude rather then the GW phase, and hence the large number of cycles completed by an EMRI does not translate to very high-precision measurements. Extrinsic source parameters and their expected precision are:

- luminosity distance with better than $\sim 10\%$ precision;
- sky localization with precision $\lesssim 10$ deg^2, which could significantly improve with the detection of the electromagnetic counterpart due to the interaction of the inspiralling body with the accretion disk of the MBH [57, 58].

The EMRI inspiral can accumulate signal-to-noise (SNR) ratio over several months or years, making extreme mass ratio inspirals detectable out to redshifts $z \sim 3 - 4$ [56]. A conservative SNR value for EMRIs detection is considered 30 [35, 59, 60].

Event rates for EMRIs are very uncertain [35, 59–63]. Depending on the astrophysical scenarios, a range from few to thousands EMRIs per year have been estimated by [35]. Such uncertainty is mostly due to the current uncertainties in EMRIs astrophysics, such as the population of MBHs, the distribution of the stellar cluster around them and the range of EMRIs orbits [61]. EMRIs event rate is predicted to be dominated by highly-eccentric orbits. Moreover, thanks to both evolutionary and selection effects, it is plausible that MBHs falling in the LISA band will be rapidly spinning, with $a \sim 0.9M$ or possibly even larger [35, 64].

1.3.2 Theoretical modeling

From a theoretical point of view, several methods have been developed for the modeling of binary systems of compact objects. The typical theoretical models commonly used for binary systems varies accordingly to the mass ratio of the binary and the orbital separation of its components, as shown in the schematic picture of Fig.1.4 [39]. For nearly comparable mass systems, as those sampled by the ground-based detectors, the early stages of the inspiral can be modeled with post-Newtonian (PN) and post-Minkowskian methods [65], appropriate for the low-velocity, weak-field regime, or the parametrized post-Einsteinian (ppE) approach [66]. These methods become more and more inaccurate with the decreasing of the orbital separation, so that i) numerical relativity methods are used for the late inspiral

and the merger of nearly comparable mass binaries, while ii) perturbation theory approaches and self-force methods come in hand with the increasing of the binary mass ratio, representing the most accurate theoretical modeling for Extreme Mass Ratio Inspirals [39, 67].

Fig. 1.5 shows an artistic representation of the two different binary systems: on the left, nearly comparable mass binaries during the (early) inspiral, while EMRIs are pictured on the right. The bottom panel of each image shows an artistic representation of typical GW signals emitted from the relative source, highlighting the modulation of the EMRI GW amplitude due to the orbital plane precession.

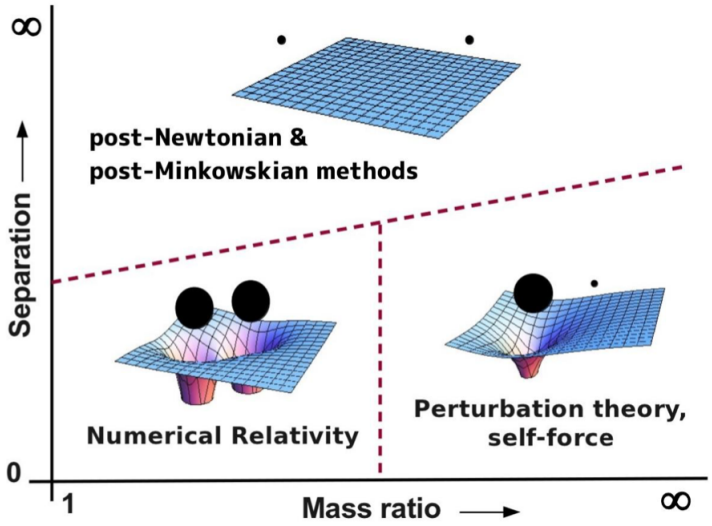

Figure 1.4. Schematic representation of the theoretical tools used to model different binary systems, depending on their orbital separation and mass ratios [39].

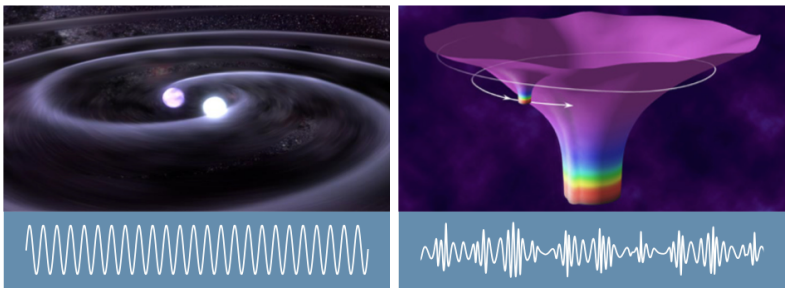

Figure 1.5. Artistic representations of comparable mass inspirals (left) and of EMRIs (right). The bottom panels of both images pictures the representative shape of the corresponding emitted GW signal. Credit:NASA and [51].

Within the framework of perturbation theory, the EMRI system is modeled considering expansions order by order in the extreme mass ratio q of the binary. During the inspiral, the secondary moves on the background spacetime of the primary, perturbing it and giving rise to gravitational waves. The energy and angular momentum loss through GWs drives the binary evolution.

At first order in the binary mass ratio, the little object is treated as a point-particle and the inspiral is built adiabatically through a sequence of geodesics orbits of the spacetime background. Within General Relativity, such background is described by the Kerr metric, which represents the vacuum solution of non-static, rotating, stationary, asymptotally flat black hole (discussed in Chapter 3). A schematic description of the complex geodesics orbits of the Kerr spacetime is shown in the left picture of Fig. 1.6, while the right pictures are relative to special resonant orbits [39]. Several works have been done which provide a model of adiabatic EMRI inspiral in GR, from simpler to more complex and fully generic orbits [68–71].

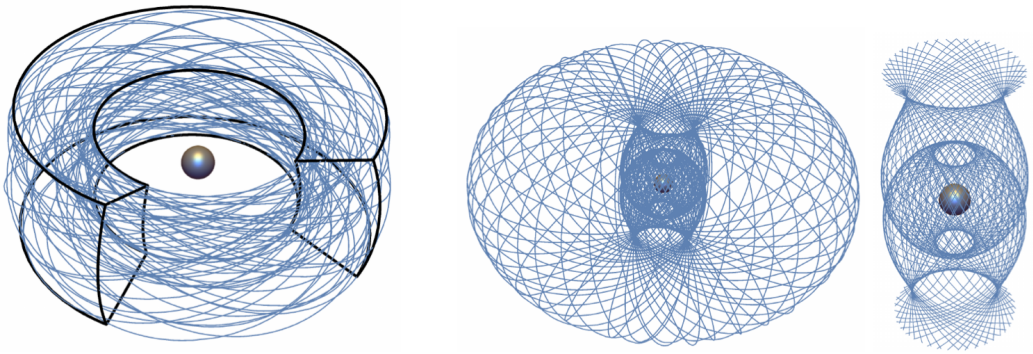

Figure 1.6. Left: Typical geodesic orbit around a Kerr black hole. The orbit ergodically fills the interior of the outlined torus-shaped region. Right: The special case of a resonant orbit, for which the motion is no longer ergodic. For clarity, the rightmost figure expands the central region of the resonant orbit. [39]

Improvements in the modeling consist in considering the next orders in the mass ratio, by taking into account the structure of the secondary object and its interaction with its own gravitational perturbations. This process, called $self-force$, leads to a secular deviation from the adiabatic inspiral. Although small, the correction induced by the self-force piles up due to the large number of orbits composing the inspiral, leading to important corrections to the orbital evolution [39, 67, 72].

In order to build accurate waveforms for the future LISA data analysis, the GW phase needs to be modeled by including all the terms (at least) up to $O(q)$, so that it is necessary to include the first and second post-adiabatic corrections, which contributes to the GW phase at $O(q^0)$ and $O(q)$, respectively, while the leading adiabatic terms contributes to the emitted GW phase at $O(q^{-1})$ [40, 73]. In addition, transient resonances of the Kerr spacetime contribute to the phase at $O(q^{-1/2})$ and need to be taken into account [74]. Significant progress has been made in this within the confine of GR, with the first waveforms containing the first post-adiabatic correction being a recent breakthrough [41–43].

As a toy model, self-force computations on a scalar charge inspiralling on the Kerr background have been performed in [75–77].

All these features are further discussed in Chapter 4, which provide the EMRIs theoretical description both in General Relativity and in alternative theories of gravity. Such theories are presented in the next chapter.

Chapter 2

Alternative theories of gravity

Modified gravity theories have been formulated with the aim of solving open problems of fundamental physics and to test General Relativity in the strong-field regime, providing new models to be compared with the predictions of the Einstein theory. In this chapter we present a brief description of the modified gravity scenarios, focusing on theories with extra scalar fields and how the presence of such fields affect black hole solutions.

2.1 Gravity theories with scalar fields

General Relativity is governed by the Einstein field equations

$$G_{\mu\nu} + \Lambda g_{\mu\nu} = 8\pi T_{\mu\nu} \ , \tag{2.1}$$

where $G_{\mu\nu}$ is the Einstein tensor, defined as $G_{\mu\nu} = R_{\mu\nu} - \frac{1}{2} g_{\mu\nu} R$, where $g_{\mu\nu}$ is the metric tensor and $R_{\mu\nu}$ and R are the Ricci tensor and the Ricci scalar, respectively. $\Lambda g_{\mu\nu}$ is the cosmological term, where Λ is the cosmological constant, and $T_{\mu\nu}$ is the stress-energy tensor describing the source-term. The Einstein equations can be obtained from the variational principle by varying the action

$$S\left[\mathbf{g}, \Psi\right] = S_{EH}\left[\mathbf{g}\right] + S_M\left[\mathbf{g}, \Psi\right] \ , \tag{2.2}$$

with respect to the metric tensor $\mathbf{g}$, where S_{EH} is the Einstein-Hilbert action given by

$$S_{EH} = \int d^4x \frac{\sqrt{-g}}{16\pi} R \ , \tag{2.3}$$

and S_M is the action of the matter fields Ψ.

Such equations arise as unique from the "uniqueness theorem" given by the Lovelock's theorem which states that [78, 79]:

In four spacetime dimensions the only divergence-free symmetric rank-2 tensor constructed solely from the metric $g_{\mu\nu}$ and its derivatives up to second differential order, and preserving diffeomorphism invariance, is the Einstein tensor plus a cosmological term.

Alternative gravity theories can be formulated abandoning one or more assumptions on which the Lovelock's theorem is based, and which build General Relativity,

so that the theorem is typically used to classify alternative theories of gravity, depending on which assumptions of the theorem they violate. Four different ways to circumvent such theories as identified in [14] are: i) addition of extra (scalar, vector and/or tensor) fields, ii) violation of the Weak Equivalent Principle (WEP), iii) violation of diffeomorphism, which leads to Lorentz violating theories and massive gravity theories, iv) inclusion of higher dimensions (> 4). A particular alternative gravity theory can belong to one or more of these classes.

However, it has been shown how the majority of the modified gravity theories can be reformulated as General Relativity with additional fundamental fields. In this scenario, looking for deviations from GR is equivalent to looking for new fundamental fields [13, 80].

This thesis focuses on extra scalar fields, considering both massless and massive scalars, which provide the most simple beyond-GR and beyond-SM scenarios with additional fields. In the following we present particular modified gravity theories with extra scalar fields, focusing on: scalar-tensor theories, f(R) theories and quadratic gravity theories. In the next section, we discuss how the presence of new scalar fields in the gravity theory affect black holes, stressing how they can be used to test GR.

Scalar-tensor gravity

In scalar-tensor theories, the gravitational sector is non-minimally coupled to one or more scalar fields, so that the Ricci scalar in the Einstein-Hilbert action is multiplied by a function of the scalar fields [80–83].

A prototype of such theories is given by the Brans-Dicke theory, described by the action

$$S = \int d^4x \frac{\sqrt{-g}}{16\pi} \left[\phi R - \frac{\omega_{BD}}{\phi} g^{\mu\nu} \partial_\mu \phi \partial_\nu \phi + V(\phi) \right] + S_M(\Psi, g_{\mu\nu}) \ , \tag{2.4}$$

in which ω_{BD} is the Brans-Dicke constant. The general form of scalar-tensor theories is given by considering such constant as a function of the scalar field, i.e. $\omega_{BD} \to \omega(\phi)$. The action is then given by

$$S = \int d^4x \frac{\sqrt{-g}}{16\pi} \left[\phi R - \frac{\omega(\phi)}{\phi} g^{\mu\nu} \partial_\mu \phi \partial_\nu \phi + V(\phi) \right] + S_M(\Psi, g_{\mu\nu}) \ , \tag{2.5}$$

which is the most general action in which one scalar field is non-minimally coupled to gravity and which is second order in the derivatives of the scalar [84, 85]. This action is referred to as the *Jordan-frame* action. With a conformal transformation $g^\star_{\mu\nu} = \phi g_{\mu\nu}$ and the scalar field redefinition $4\sqrt{\pi}\varphi d\varphi = \sqrt{2\omega(\phi) + 3} d\phi$, it is possible to move from such frame to the *Einstein-frame*, in which the scalar field minimally couples to gravity and non minimally couples to matter:

$$S = \int d^4x \frac{\sqrt{-g^\star}}{16\pi} \left[R^\star - \frac{1}{2} \partial_\mu \varphi \partial_\nu \varphi + U(\varphi) \right] + S_M(\Psi, \phi^{-1} g^\star_{\mu\nu}) \ , \tag{2.6}$$

where $U(\varphi) = V(\phi)/\phi^2$.

The most general action that can lead to second order (in time) field equations for the metric and the scalar is Horndeski gravity [86].

f(R) theories

This class of theories includes that ones in which the Einstein-Hilbert action is modified replacing the Ricci scalar with a function of it, so that the action becomes [87]

$$S = \int d^4x \frac{\sqrt{-g}}{16\pi} f(R) + S_M(\Psi, g_{\mu\nu}) \ . \tag{2.7}$$

Such theories have been explored as prototypical infrared modifications to General Relativity, proposing infrared corrections of gravity as an explanation for the cosmic acceleration, alternative to the standard ΛCDM model. However, f(R) theories are dynamically equivalent to scalar-tensor theories [80]. Indeed, considering the action

$$S = \frac{1}{16\pi G} \int d^4x \sqrt{-g} \left[f(\phi) + \varphi(R - \phi) \right] + S_M(\Psi, g_{\mu\nu}) \tag{2.8}$$

and varying it with respect to φ one gets $\phi = R$. Replacing such equation in the action leads to $f(R)$ theories. Moreover, by varying the action (2.8) with respect to ϕ one obtains $\varphi = f'(\phi)$, which leads to the dynamically equivalent action

$$S = \frac{1}{16\pi G} \int d^4x \sqrt{-g} \left[\varphi R - V(\varphi) \right] + S_M(\Psi, g_{\mu\nu}) \tag{2.9}$$

with $V(\varphi) = f(\phi) - \phi f'(\phi)$ and it falls within the Brans–Dicke theories with $\omega_{BD} = 0$.

Quadratic gravity

Quadratic gravity theories includes quadratic curvature terms in the action in order to make the theory formally renormalizable within the standard quantum field theory approach [88], in the framework of Effective Field Theory (EFT). In the following we show two examples of such theories.

1) Scalar Gauss Bonnet (sGB):

Scalar Gauss-Bonnet theories are described by the action

$$S = S_0 + \frac{\alpha_{sGB}}{4} \int d^4x \frac{\sqrt{-g}}{16\pi} f(\varphi) \mathcal{G} + S_M(\Psi, g_{\mu\nu}) \ , \tag{2.10}$$

where $\mathcal{G}$ is the scalar-Gauss Bonnet reform

$$\mathcal{G} = R^2 - 4R_{\mu\nu}R^{\mu\nu} + R_{\mu\nu\alpha\beta}R^{\mu\nu\alpha\beta} \ , \tag{2.11}$$

with $R_{\mu\nu}$ being the Ricci tensor and $R_{\mu\nu\alpha\beta}$ the Riemann invariant, and $f(\varphi)$ is a scalar function of the scalar field. Such a function describes the coupling of the scalar field to the Gauss Bonnet invariant. Of particular interest are two cases:

i) $f(\varphi) = e^{\varphi}$ of Einstein dilaton Gauss Bonnet gravity (EdGB);

ii) $f(\varphi) = \varphi$ of shift-symmetric gravity.

2) Dynamical Chern Simons gravity (dCS):

The dynamical Chern-Simons theory, a Chern-Simons theory with the kinetic term of the scalar field, is described by the action [89]

$$S = \frac{1}{16\pi G}\int d^4x\sqrt{-g}\,[R - 2\nabla_\mu\varphi\nabla^\mu\varphi - V(\varphi) + \alpha_{CS}\varphi\,{}^\star RR] + S_M(\Psi, g_{\mu\nu})\ , \quad (2.12)$$

where ${}^\star RR$ is the Pontryagin scalar defined as ${}^\star RR = \frac{1}{2}R_{\mu\nu\rho\sigma}\epsilon^{\nu\mu\lambda\kappa}R^{\rho\sigma}{}_{\lambda\kappa}$.

2.2 Black holes and scalar fields

In General Relativity, stationary and asymptotically flat black holes satisfy the no-hair theorem, dictating that a stationary black hole's spacetime in $3+1$ dimensions is described only by three parameters: its mass M, its angular momentum $J = aM$, where a is the black hole's spin, and its electrical charge Q, which, for astrophysical black holes, can be neglected [18]. Thus, the most general metric describing such solutions is given by the Kerr metric.

Modifying the gravity theory by adding fundamental scalar fields can, in general, lead to black hole solutions endowed with a scalar profile, so that they can be thought of as carrying a scalar charge. In this sense, the black hole is said to carry scalar hair and the theory to evade the no-hair theorem.

However, no-scalar-hair theorems for stationary black holes have been proven for most scalar-tensor theories, which means that the scalar must be trivial (constant) and that the black hole's spacetime is described by the Kerr metric [19–23, 90, 91]. In order to evade no-hair theorem and actually obtain black holes with non-trivial scalar profiles, the coupling between the scalar and higher order curvature invariants is required [24–27, 92, 93].

In particular, no-hair theorems have been proven for shift-symmetric scalar tensor theories [23], which are those in which the scalar enjoys symmetry under the transformation $\varphi \to \varphi +$ constant which is expected to be respected by massless scalars. Shift-symmetry prevents static, spherically symmetric and asymptotically flat black holes from acquiring scalar hair, unless a linear coupling between the scalar field and the Gauss-Bonnet invariant is considered [92, 93].

The nature of these couplings then implies that the scalar charge per unit mass of a BH is inversely proportional to its mass to some positive power, so that the BH is said to have hair of "second type". The power depends on the specific theory but the general trend is that the more massive a BH is, the more weakly charged it is [24–34].

Massive scalars, which are not covered by shift-symmetry, are essential in certain scenarios such as superradiance-induced clouds [94] or scalarization [25, 26, 95–97], which rely on the presence of a mass or of interactions that violate shift symmetry to generate scalar charge.

In this framework, EMRIs result powerful candidates to test gravity. Indeed, in such system the massive black hole is expected to be negligibly charged, while the inspiralling body is expected to carry a significant scalar charge, causing an emission in the corresponding polarisation. The extra scalar emission represents the key ingredient to investigate deviations from GR, because it leaves an imprint on the emitted GW signal by modifying the binary's dynamics.

Chapter 3

The Kerr metric

In this chapter, we present the Kerr metric with its properties, which describe the background spacetime of our EMRI model.

The Kerr metric describes the solution of a rotating, non static, stationary, axially symmetric and asymptotically flat black hole. In the $Boyer - Lindquist$ coordinates $x^\mu = (t, r, \theta, \phi)$, the Kerr metric is given by [98]

$$\mathrm{d}s^2 = -\left(1 - \frac{2Mr}{\Sigma}\right)\mathrm{d}t^2 - \frac{4aMr\sin^2\theta}{\Sigma}\mathrm{d}t\mathrm{d}\phi + \frac{\Sigma}{\Delta}\mathrm{d}r^2 + \Sigma\mathrm{d}\theta^2 + \left(r^2 + a^2 + \frac{2Ma^2r\sin^2\theta}{\Sigma}\right)\sin^2\theta\,\mathrm{d}\phi^2, \quad (3.1)$$

where $\Delta(r) \equiv r^2 - 2Mr + a^2$ and $\Sigma(r, \theta) \equiv r^2 + a^2\cos^2\theta$. The metric depends on two parameters, the mass of the black hole, M, and the spin of the black hole, a, so that $J = aM$ is the black hole angular momentum.

This solution describes the spacetime generated by a curvature singularity concealed by a horizon. The curvature singularity is given by $\Sigma = 0$, in which the curvature invariants are singular. The metric is also singular for $\Delta = 0$, but in this case the curvature invariants are regular. $\Delta = 0$ is then a coordinate singularity and its solutions are

$$r_\pm = M \pm \sqrt{M^2 - a^2}\ . \quad (3.2)$$

The solution with the " $-$ " sign gives the radius of the inner horizon, while that one with the " $+$ " sign gives the radius of the outer horizon, hereafter considered as the horizon of the black hole. Moreover, we will consider only $-M \leq a \leq M$, since a solution with spin outside this range represents a naked singularity (not covered by an event horizon) and is considered unphysical.

3.1 The geodesic structure of the Kerr metric

To model the EMRI's dynamics we need to study geodesics of the Kerr background. The geodesics equations can be found by following the $Hamilton - Jacobi$ approach. The derivative of the space-time coordinates of the inspiralling particle with respect to its proper time are given by:

$$\Sigma^2 \left(\frac{dr}{d\tau}\right)^2 = \left[E(r^2+a^2) - aL\right]^2 - \Delta\left[r^2 + (L-aE)^2 + Q\right], \tag{3.3}$$

$$\Sigma^2 \left(\frac{d\theta}{d\tau}\right)^2 = Q - \cot^2\theta L^2 - a^2\cos^2\theta(1-E^2)\ , \tag{3.4}$$

$$\Sigma\left(\frac{d\phi}{d\tau}\right) = \csc^2\theta L + aE\left(\frac{r^2+a^2}{\Delta} - 1\right) - \frac{a^2 L}{\Delta}\ , \tag{3.5}$$

$$\Sigma\left(\frac{dt}{d\tau}\right) = E\left[\frac{(r^2+a^2)^2}{\Delta} - a^2\sin^2\theta\right] + aL\left(1 - \frac{r^2+a^2}{\Delta}\right). \tag{3.6}$$

The quantities E , L and Q are the constants of motion of the particle. E and L are respectively the energy and the angular momentum per unit mass of the particle, measured at infinity, and they are associated to a spacetime symmetry, since in the $Boyer - Lindquist$ coordinate the Kerr metric is independent of t and ϕ. Q is the Carter constant, which is zero for an equatorial orbit [99].

In the following we will focus on two types of orbits: i) equatorial circular and ii) equatorial eccentric.

3.1.1 Equatorial circular geodesics

While for the Schwarzschild metric a geodesic which starts in the equatorial plane (identified by $\theta = \pi/2$) remains in the equatorial plane at later times, for the Kerr metric in general $d\theta/d\tau \neq 0$.

For equatorial and circular orbits $\theta = \pi/2$, $r(t) = r_0$, $Q = 0$ and the geodesic equations become

$$\frac{dr}{d\tau} = 0\ , \tag{3.7}$$

$$\frac{d\theta}{d\tau} = 0\ , \tag{3.8}$$

$$\Sigma\left(\frac{d\phi}{d\tau}\right) = aE\left(\frac{r^2+a^2}{\Delta} - 1\right) + \left(1 - \frac{a^2}{\Delta}\right)L\ , \tag{3.9}$$

$$\Sigma\left(\frac{dt}{d\tau}\right) = E\left[\frac{(r^2+a^2)^2}{\Delta} - a^2\right] + aL\left(1 - \frac{r^2+a^2}{\Delta}\right)\ . \tag{3.10}$$

The value of E and L_z depends on whether the orbit is prograde, which means that the particle's rotation is in the same direction of the black hole's spin, or retrograde, with the rotation of the particle opposite to that one of the black hole. The expressions of E^{pro} and L^{pro} for a prograde orbit and E^{ret} and L^{ret} for a retrograde orbit are:

$$E^{pro} = \frac{1 - 2v^2 + qv^3}{\sqrt{1 - 3v^2 + 2qv^3}} \ , \tag{3.11}$$

$$L^{pro} = rv\frac{1 - 2qv^3 + q^2v^4}{\sqrt{1 - 3v^2 + 2qv^3}} \ , \tag{3.12}$$

$$E^{ret} = \frac{1 - 2v^2 - qv^3}{\sqrt{1 - 3v^2 - 2qv^3}} \ , \tag{3.13}$$

$$L^{ret} = -rv\frac{1 + 2qv^3 + q^2v^4}{\sqrt{1 - 3v^2 - 2qv^3}} \ . \tag{3.14}$$

The functions v and q are defined as $v \equiv \sqrt{M/r}$ and $q \equiv a/M$, where $0 \leq a \leq M$ and whether the orbit is prograde or retrograde is set by the signs in the equations.

Since we are considering equatorial circular orbits, we can define the angular velocity of the particle as

$$\omega_p = \frac{d\phi}{dt} = \frac{d\phi/d\tau}{dt/d\tau} = \pm\frac{M^{1/2}}{r^{3/2} \pm aM^{1/2}} \tag{3.15}$$

where the $+$ sign holds for the prograde orbits and the $-$ sign for the retrograde ones. A circular orbit of particular interest is the equatorial innermost stable circular orbit (ISCO), which in the Kerr metric is given by [100]

$$R_{ISCO} = M\left(3 + Z_2 \pm \sqrt{(3 - Z_1)\,(3 + Z_1 + 2Z_2)}\right). \tag{3.16}$$

The positive (negative) sign is relative to retrograde (prograde) orbits. The terms Z_1 and Z_2 are given by the expressions

$$Z_1 = 1 + \sqrt[3]{1 - x^2}\left(\sqrt[3]{1 + x} + \sqrt[3]{1 - x}\right) \ , \tag{3.17}$$

$$Z_2 = \sqrt{3x^2 + Z_1^2} \ , \tag{3.18}$$

with $x = a/M$. When $x = 0$ the radius of the ISCO is $R_{ISCO} = 6M$, as expected for a Schwarzschild black hole. For a prograde orbit the increase of a causes a decreasing of R_{ISCO} until its minimun value $R_{ISCO} = M$, obtained for $a/M = 1$. Thus, for a prograde orbit in the Kerr metric, the particle can orbits closer to the central BH compared to the non-rotating case.

In our EMRI model we restricted our analysis to prograde orbits, which are expected to dominate [101, 102].

3.1.2 Equatorial eccentric geodesics

For equatorial eccentric orbits, $\theta = \pi/2$ and $Q = 0$. The geodesic equations are given by [68]

$$r^2\frac{\mathrm{d}r}{\mathrm{d}\tau} = \pm(V_r)^{1/2} = \pm\sqrt{T^2 - \Delta\left[r^2 + (L-aE)^2\right]}\ , \tag{3.19}$$

$$r^2\frac{\mathrm{d}\phi}{\mathrm{d}\tau} = V_\phi = -(aE-L) + \frac{aT}{\Delta}\ , \tag{3.20}$$

$$r^2\frac{\mathrm{d}t}{\mathrm{d}\tau} = V_t = -a(aE-L) + \frac{\left(r^2+a^2\right)T}{\Delta}\ , \tag{3.21}$$

$$\theta(\tau) = \pi/2\ , \tag{3.22}$$

where $T \equiv E\left(r^2+a^2\right) - aL$. E and L are the constant of motion, the energy and the angular momentum per unit mass of the point particle, respectively. In the following we consider bound orbits, for which $0 < E < 1$.

The motion in the radial coordinate is periodic. The coordinate can be parametrised as [70]

$$r(\chi) = \frac{p}{1+e\cos\chi}\ , \tag{3.23}$$

where (p, e) are the semilatus rectum and the eccentricity of the orbit, respectively, and χ varies monotonically from $\chi = 0$ at the periastron r_p to $\chi = \pi$ at the apastron r_a, given by

$$r_p = \frac{p}{1+e}, \qquad r_a = \frac{p}{1-e}\ . \tag{3.24}$$

The apastron and the periastron of the orbits are two turning points, i.e. such that $V_r(r_p) = V_r(r_a) = 0$. The coordinate time taken from the secondary to pass through two consecutive periastron passages defines the radial period T_r, so that $T_r = t(\chi = 2\pi) = 2t(\chi = \pi)$. A geodesic can be uniquely determined by the set of the two parameters (E, L) or equivalently by (p, e).

The energy E and the angular momentum L are then given by [70]

$$E = \left[1 - \left(\frac{M}{p}\right)(1-e^2)\left(1 - \frac{x^2}{p^2}(1-e^2)\right)\right]^{1/2}\ , \tag{3.25}$$

$$L = x + aE\ , \tag{3.26}$$

where

$$x = \left[\frac{-N - \mathrm{sign}(a)\sqrt{N^2 - 4FC}}{2F}\right]^{1/2}\ , \tag{3.27}$$

and the functions F, N, C are given by:

$$F(p,e) = \frac{1}{p^3}\left[p^3 - 2M(3+e^2)p^2 + M^2(3+e^2)^2 p - 4Ma^2(1-e^2)^2\right]\ , \tag{3.28}$$

$$N(p,e) = \frac{2}{p}\left\{\left[M^2(3+e^2) - a^2\right]p - Mp^2 - Ma^2(1+3e^2)\right\}\ , \tag{3.29}$$

$$C(p) = (a^2 - Mp)^2\ . \tag{3.30}$$

The functions $t(r)$ and $\phi(r)$ can be obtained by integrating the geodesics equations:

$$t(r) = \int_{r1}^{r}\frac{\mathrm{d}t}{\mathrm{d}\tau}\left(\frac{\mathrm{d}r}{\mathrm{d}\tau}\right)^{-1}\mathrm{d}r\ , \tag{3.31}$$

$$\phi(r) = \int_{r1}^{r}\frac{\mathrm{d}\phi}{\mathrm{d}\tau}\left(\frac{\mathrm{d}r}{\mathrm{d}\tau}\right)^{-1}\mathrm{d}r\ . \tag{3.32}$$

However, these integrals are divergent at the turning points of the orbit. To avoid this divergence, we can perform the integrals over the parameter χ:

$$\phi(\chi) = \int_0^{\chi} \mathrm{d}\chi' \frac{\tilde{V}_\phi(\chi', p, e)}{J(\chi', p, e)\tilde{V}_r(\chi', p, e)} \ , \tag{3.33}$$

$$t(\chi) = \int_0^{\chi} \mathrm{d}\chi' \frac{\tilde{V}_t(\chi', p, e)}{J(\chi', p, e)\tilde{V}_r(\chi', p, e)} \ , \tag{3.34}$$

where the functions $\tilde{V}_{t,r,\phi}$ and J are defined as

$$\tilde{V}_r(\chi, p, e) = x^2 + a^2 + 2axE - \frac{2Mx^2}{p}(3 + e\cos\chi) \ , \tag{3.35}$$

$$\tilde{V}_\phi(\chi, p, e) = x + aE - \frac{2Mx}{p}(1 + e\cos\chi) \ , \tag{3.36}$$

$$\tilde{V}_t(\chi, p, e) = a^2E - \frac{2aMx}{p}(1 + e\cos\chi) + \frac{Ep^2}{(1 + e\cos\chi)^2} \ , \tag{3.37}$$

$$J(\chi, p, e) = 1 - \frac{2M}{p}(1 + e\cos\chi) + \frac{a^2}{p^2}(1 + e\cos\chi)^2 \ , \tag{3.38}$$

where x is given in Eq.(3.27).

From the radial period T_r and the variation of ϕ in such period, the orbital frequencies Ω_r and Ω_ϕ are defined as

$$\Omega_r = \frac{2\pi}{T_r}, \qquad \Omega_\phi = \frac{\Delta\phi}{T_r} \ . \tag{3.39}$$

The phase of the emitted gravitational wave signal is related to (Ω_r, Ω_ϕ) through the frequency ω_{mn}:

$$\omega_{mn} = m\Omega_\phi + n\Omega_r \ , \tag{3.40}$$

with $(m, n) \in \mathbb{Z}$, as explained in Chapter 5.

All bound equatorial orbits have $p^2 > x^2(1 + e)(3 - e)$. Given a certain value of the spin a and of the eccentricity e, the curve

$$p_s^2 = x^2(1 + e)(3 - e) \tag{3.41}$$

defines the separatrix in the $e - p$ plane. If $e = 0$, the separatrix reduces to the ISCO in the Kerr spacetime.

Chapter 4

Extreme Mass Ratio Inspirals in General Relativity and beyond

The Kerr metric presented in the previous chapter provides the description of the background spacetime for Extreme Mass Ratio Inspirals. The primary is modeled as an isolated Kerr black hole, which is perturbed by the secondary's inspiral. In this chapter we show the EMRI description in GR, with the basis of the perturbation theory approach and of the self-force program. The last section is dedicated to the theoretical modeling of EMRIs in beyond-GR theories with additional real and massless scalar fields, while the massive scenario is left to Chapter 9.

4.1 EMRIs in General Relativity

General Relativity is described by the action

$$S\left[\mathbf{g},\Psi\right]=S_{EH}\left[\mathbf{g}\right]+S_{M}\left[\mathbf{g},\Psi\right]\ , \tag{4.1}$$

where $\mathbf{g}$ is the metric tensor, S_M is the action of the matter fields Ψ and S_{EH} is the Einstein-Hilbert action given by

$$S_{EH}=\int d^4x\frac{\sqrt{-g}}{16\pi}R\ , \tag{4.2}$$

with R being the Ricci scalar. By varying the action with respect to the metric tensor, the Einstein fields equation are obtained:

$$G_{\mu\nu}=8\pi T_{\mu\nu}, \tag{4.3}$$

where $G_{\mu\nu}$ and $T_{\mu\nu}$ are the Einstein tensor and the stress-energy tensor, respectively. The L.H.S of the equations contain the metric tensor $g_{\mu\nu}$ and its derivative, while the stress-energy tensor contains information on the matter sources.

For Extreme Mass Ratio Inspirals, asymmetric binary systems with mass ratio $q\ll 1$, the Einstein fields equation can be solved perturbatively in q in the framework of black hole perturbation theory [39, 67, 72]. With such approach, the metric is expanded order by order considering perturbations of a background metric $g^{(0)}_{\mu\nu}$,

$$g_{\mu\nu}=g^{(0)}_{\mu\nu}+qh^{(1)}_{\mu\nu}+q^2h^{(2)}_{\mu\nu}+O(q^3)\ . \tag{4.4}$$

Inserting this expansion in the Einstein tensor we obtain

$$G_{\mu\nu}[g] = G_{\mu\nu}[g^{(0)}] + q\ \delta G_{\mu\nu}[h^{(1)}] + q^2\left(\delta G_{\mu\nu}[h^{(2)}] + \delta^2 G_{\mu\nu}[h^{(1)}]\right) + O(q^3)\ , \quad (4.5)$$

where $\delta G_{\mu\nu}[h^{(i)}]$ is linear in $h^{(i)}_{\mu\nu}$ and $\delta^2 G_{\mu\nu}[h^{(i)}]$ includes $\partial h^{(i)}_{\mu\nu}\partial h^{(i)}_{\alpha\beta} + h^{(i)}_{\mu\nu}\partial^2 h^{(i)}_{\alpha\beta}$. For a background metric which is given as the solution of the vacuum Einstein equations at zeroth order in q, the stress-energy tensor is expanded as

$$T_{\mu\nu} = qT^{(1)}_{\mu\nu} + q^2 T^{(2)}_{\mu\nu} + O(q^3)\ , \quad (4.6)$$

and the zeroth order in q gives the vacuum equations

$$G_{\mu\nu}[g^{(0)}] = 0\ . \quad (4.7)$$

The solution of these equations, for the case of an axially symmetric, rotating, asymptotically flat black hole, is given by the Kerr metric. At order by order in q, we obtain different sets of differential equations.

The equations at the first order in the binary mass ratio are the linearized Einstein equations

$$\delta G_{\mu\nu}[h^{(1)}] = 8\pi T^{(1)}_{\mu\nu}\ . \quad (4.8)$$

Once $h^{(1)}$ is obtained from the first order equations, $h^{(2)}$ is obtained from the second order equations, i.e.

$$\delta G_{\mu\nu}[h^{(2)}] = 8\pi T^{(2)}_{\mu\nu} - \delta^2 G_{\mu\nu}[h^{(1)}]\ , \quad (4.9)$$

and so on.

Given a general metric $g_{\mu\nu}$ describing a spacetime, an object freely moving in it follows geodesics of such metric. If we consider the motion with respect to a background metric $g^{(0)}_{\mu\nu}$, the object motion can be modeled as a geodesics motion with respect to the background plus additional corrections due to the metric perturbations. With this interpretation, the object can be thought as experiencing an external "force", which appear in the equation of motion expanded in q as

$$\frac{D^2 z^\mu}{d\tau^2} = f^\mu_{(0)} + q f^\mu_{(1)} + q^2 f^\mu_{(2)} + O(q^3)\ , \quad (4.10)$$

where $z^\mu(\tau)$ is the perturbed worldline, τ the proper time with respect to the background metric, $D^2 z^\mu/d\tau^2$ the covariant acceleration and $f^\mu_{(n)}$ the covariant force driving the acceleration. The zeroth-order $f^\mu_{(0)}$ describes the geodesic motion and takes value zero.

The first order, linearized Einstein equations (4.8) for perturbations of a Kerr background are treated with the Newman-Penrose formalism [103] by following the Teukolsky approach [36–38], discussed in Chapter 5. The inspiralling object is skeletonized to a point-particle of mass m_p, so that the stress energy tensor is given by

$$T^{(1)}_{\mu\nu} = m_p \int \frac{\delta^{(4)}(x - y^p(\lambda))}{\sqrt{-g}} \frac{dy^p_\mu}{d\lambda}\frac{dy^p_\nu}{d\lambda} d\lambda\ , \quad (4.11)$$

where y^p is the wordline of the point-particle, λ the proper time and g the determinant of the background Kerr metric. Such a term can also be obtained by varying the

action (4.1), where the action of the matter fields S_M is given by the action of a point particle S_p with the form

$$S_p = -\int m_p \, ds = -\int m_p \sqrt{g_{\mu\nu} \frac{dy_p^\mu}{d\lambda} \frac{dy_p^\nu}{d\lambda}} d\lambda \, . \tag{4.12}$$

The complete adiabatic EMRIs description in General Relativity has been performed by [68–71].

At the next orders, the secondary object cannot be treated as a point-particle, due to divergence at the location at the particle and non-integrability issues. From the second order, the finite-size of the secondary, inspiralling object and its interaction with its own gravitational perturbations are taken into account. The secondary object is treated as a singularity of given mass and spin, carrying the body's multipole moments [104].

The *self-force* program refers to the two timescale expansion [40, 105], which considers the different two timescales that characterize EMRIs. One is the time of the orbital evolution, T_o, while the other one is the time of the inspiral, T_i, with $T_o \ll T_i$. Indeed, the time of the inspiral scales as $T_i \sim M/q = M^2/m_p$, while $T_o \sim M$ so that $T_o/T_i \sim q$ [106].

In the action-angle approach, we define the angle variables [107, 108]

$$q_\alpha \equiv (q_t, q_r, q_\theta, q_\phi) \, , \tag{4.13}$$

which describe the orbital motion of the secondary in suitable coordinates, and the integrals

$$J_i \equiv (E, L_z, Q) \, , \tag{4.14}$$

which correspond to the integral constants of the geodesic motion, i.e. the energy, angular momentum and Carter constant, without the dependence of the secondary mass. The motion of the small body around the central black hole is then described by the two sets of equations

$$\begin{cases} \dfrac{dq_\alpha}{d\lambda} & = \omega_\alpha(\mathbf{J}) + q \; g_\alpha(q_\theta, q_r, \mathbf{J}) + O(q^2) \, , \\ \dfrac{dJ_i}{d\lambda} & = q \; G_i(q_\theta, q_r, \mathbf{J}) + O(q^2) \, , \end{cases} \tag{4.15}$$

with λ a time variable.

The forcing terms g_α and G_i are due to the first order self-force and can be separated in i) an averaged part over the 2-torus parametrized by q_r and q_θ, and ii) in an oscillatory part, so that

$$G_i(q_\theta, q_r, \mathbf{J}) = \langle G_i(\mathbf{J}) \rangle + \delta G_i(q_\theta, q_r, \mathbf{J}) \, , \tag{4.16}$$

where the averaged part is defined as

$$\langle G_i(\mathbf{J}) \rangle = \frac{1}{2\pi^2} \int_0^{2\pi} dq_r \int_0^{2\pi} dq_\theta G_i(q_\theta, q_r, \mathbf{J}) d\lambda \, , \tag{4.17}$$

and the oscillatory part is defined by Eq. (4.16). The same applies to g_α. The forcing terms lead to conservative and dissipative effects on the orbital evolution. The phase of the emitted GW signal can be schematically written as [105]

$$\Phi(t_1,t_2) = \int_{t_1}^{t_2} \omega(t)dt$$
$$= \Phi_{\rm diss,1}(q^{-1}) + \Phi_{\rm RES}(q^{-1/2}) + \Phi_{\rm cons,1}(q^0) + \Phi_{\rm diss,2}(q^0) + \Phi_{\rm cons,2}(q) + O(q^2) \tag{4.18}$$

where in the parenthesis of each term the dependence of the extreme mas ratio q is shown. The leading, adiabatic, term contributes to the GW phase by $O(q^{-1})$.

The resonant term, indicated with $\Phi_{\rm RES}$, contributes to the phase at $O(q^{-1/2})$ and is due to transient resonances of the Kerr spacetime. Indeed, the forcing terms can be expanded in the Fourier series

$$G_i(q_\theta, q_r, \mathbf{J}) = \sum_{kn} G_{i;kn}(\mathbf{J}) e^{i(kq_\theta + nq_r)} \ . \tag{4.19}$$

the averaged terms $\langle G_i(\mathbf{J})\rangle$ vanishes unless $kq_\theta + nq_r = 0$. This equation is verified if $k = n = 0$, or in the case of a transient resonance, which is defined by q_θ and q_r being commensurate [61, 74, 109, 110].

In the following we present the EMRI model in theories in which the gravitational interaction is modified by an additional real and massless scalar field, stopping at the leading order in the mass ratio description.

4.2 EMRIs with scalar fields

We consider a vast class of gravity theories in which the gravitational interaction is modified by the addition of a new scalar field, which we assume to be real and massless, described by the action

$$S\left[\mathbf{g}, \varphi, \Psi\right] = S_0\left[\mathbf{g}, \varphi\right] + \alpha S_c\left[\mathbf{g}, \varphi\right] + S_M\left[\mathbf{g}, \varphi, \Psi\right] \ , \tag{4.20}$$

where $\mathbf{g}$ is the metric tensor, φ is the additional scalar field, and Ψ are the matter fields. The action $S_0\left[\mathbf{g}, \varphi\right]$ includes the Einstein-Hilbert action for the gravitational field and the kinetic term for the scalar field

$$S_0 = \int d^4x \frac{\sqrt{-g}}{16\pi}\left(R - \frac{1}{2}\partial_\mu\varphi\partial^\mu\varphi\right) \ . \tag{4.21}$$

The term $S_M\left[\mathbf{g}, \varphi, \Psi\right]$ is the action of the matter fields Ψ. Finally, $S_c\left[\mathbf{g}, \varphi\right]$ describes the non minimal coupling between the scalar and gravitational fields, where α is the fundamental coupling constant of the theory. We assume S_c to be analytic in the scalar field φ.

Theories considered and model of the primary

We consider theories described by the action (4.20) that can belong to one of the two cases:

i) the theory satisfies a no-hair theorem, so that stationary black holes are simply described by the Kerr metric;

ii) the theory evades no-hair theorems but has a dimensionful coupling constant, $[\alpha] = \text{mass}^n$ with $n \geq 2$, and the black hole solutions are continuously connected to the corresponding GR solution as $\alpha \to 0$. Examples of these theories are sGB gravity and dCS gravity. Since the black hole spacetime is continuously connected to the Kerr spacetime as $\alpha \to 0$, and since the only dimensionful scale of the Kerr metric is the mass M of the black hole, any correction to GR must depend on a dimensionless parameter ζ defined as:

$$\zeta \equiv \frac{\alpha}{M^n} \ . \tag{4.22}$$

If we describe EMRIs with $q = m_p/M \ll 1$ in these theories, for the parameter ζ we have

$$\zeta = \frac{\alpha}{M^n} = q^n \frac{\alpha}{m_p^n} = q^n \zeta_{\rm p} \ . \tag{4.23}$$

Bounds on α obtained from current astrophysical observations imply $\zeta_{\rm p} < 1$ [111]. Hence, we obtain $\zeta \ll 1$, so that any GR correction, which must depends on ζ, is suppressed by powers of the mass ratio. The primary spacetime is then adequately described by the Kerr metric to order $\mathcal{O}(q^n \zeta_{\rm p})$ in the mass ratio.

We can conclude that, for both classes of theories identified, at leading order in the mass ratio, the spacetime of the background is given by the Kerr metric, and the EMRI can be described as the motion of a point particle in Kerr spacetime. As shown in the following, at leading order in q, the modifications to General Relativity affect the motion of the inspiralling particle, but do not affect the background spacetime, given by the Kerr metric.

We remark that our approach is valid also for possible theories that do not belong to either of the two classes, but for which in the specific EMRIs the massive BH can be well approximated by Kerr (e.g. it just happens to carry a negligible scalar charge). Moreover, we stress that a theory in which the primary object of an EMRI is not described with good accuracy by the Kerr metric would exhibit larger deviations from GR in the gravitational waveform than those found in this thesis. Hence, our results can be considered as a conservative estimate.

Model of the secondary

In EMRIs we can identify two separate lengthscale relative to different spacetime regions, with one given by the spacetime around the inspiralling object and the other one of the exterior spacetime, which is the spacetime solution in the absence of the body. The lengthscale of the inspiralling body is much smaller then the lengthscale of the exterior spacetime. The secondary can then be modeled with the skeletonized approach [112–115] and treated as point-particle. The action of the matter fields S_M can be replaced by the particle action S_p, which is the integral of the scalar function $m(\varphi)$ over the worldline of the particle $y_p^\mu(\lambda)$ (in a reference frame $\{y^\mu\}$):

$$S_p = -\int m\left(\varphi\right) ds = -\int m\left(\varphi\right) \sqrt{g_{\mu\nu} \frac{dy_p^\mu}{d\lambda} \frac{dy_p^\nu}{d\lambda}} d\lambda \ , \tag{4.24}$$

where $m(\varphi)$ is a scalar function of the scalar field, to be evaluated at the location of the particle, and accounts for the coupling of the body to its scalar field environment. This approximation holds at linear order in the mass ratio. We remark that we do not make any assumptions on the nature of the secondary, which can be either a

black hole or a neutron star.

In the following, we derive the fields equations by varying the action with respect to the fields.

4.2.1 Gravitational field equation

By varying the action (4.20) with respect to the gravitational field, we obtain

$$G_{\mu\nu} = T^{\rm scal}_{\mu\nu} + \alpha T^{c}_{\mu\nu} + T^{p}_{\mu\nu} \ , \tag{4.25}$$

where $T^{\rm scal}_{\mu\nu}$ is obtained (together with $G_{\mu\nu}$) by varying S_0, and is given by

$$T^{\rm scal}_{\mu\nu} = \frac{1}{2}\partial_\mu\varphi\partial_\nu\varphi - \frac{1}{4}g_{\mu\nu}\left(\partial\varphi\right)^2 \ . \tag{4.26}$$

The term $\alpha T^{\rm c}_{\mu\nu}$ is the stress-energy tensor associated to the coupling between the scalar and the gravitational field, it is given by the variation of αS_c,

$$\alpha T^{\rm c}_{\mu\nu} = -\frac{16\pi\alpha}{\sqrt{-g}}\frac{\delta S_c}{\delta g^{\mu\nu}} \ . \tag{4.27}$$

Finally, $T^{\rm p}_{\alpha\beta}$ is the stress-energy tensor of the point particle, obtained from the variation of S_p and given by

$$T^{\rm p}_{\alpha\beta} = 8\pi\int m\left(\varphi\right)\frac{\delta^{(4)}(x-y^p(\lambda))}{\sqrt{-g}}\frac{dy^p_\alpha}{d\lambda}\frac{dy^p_\beta}{d\lambda}d\lambda \ . \tag{4.28}$$

We describe the EMRI system using perturbation theory with respect to the mass ratio $q \ll 1$. We expand the scalar field as $\varphi = \varphi_0 + \varphi_1$, where φ_0 is the constant background field, and φ_1 is the perturbation induced by the secondary.

We can then show that both the terms $T^{\rm scal}_{\mu\nu}$ and $\alpha T^{c}_{\mu\nu}$ can be neglected at leading (adiabatic) order in q, as they contribute only to higher (post-adiabatic) orders in the small-ratio expansion. Indeed, the stress-energy tensor of the scalar field (4.26) is quadratic in the perturbation φ_1, which means that the term $T^{\rm scal}_{\mu\nu}$ can be neglected. Concerning the term $\alpha T^{\rm c}_{\mu\nu}$, we see that $[S_0] = (\text{mass})^2$ and $[S_c] = (\text{mass})^{2-\rm n}$, which in an EMRI is evaluated on the background of the central black hole, where the only dimensionful scale is its mass M. Hence, we expect that

$$S_c \sim M^{-n} S_0 \ . \tag{4.29}$$

Looking then at $\alpha T^{c}_{\mu\nu}$ we see that

$$\alpha T^{c}_{\mu\nu} = -\frac{16\pi\alpha}{\sqrt{-g}}\frac{\delta S_c}{\delta g^{\mu\nu}} \sim -\frac{16\pi\alpha M^{-n}}{\sqrt{-g}}\frac{\delta S_0}{\delta g^{\mu\nu}} \ , \tag{4.30}$$

so that, since $\alpha M^{-n} = \zeta \ll 1$,

$$\alpha T^{c}_{\mu\nu} \sim \zeta G_{\mu\nu} \ll G_{\mu\nu} \ , \tag{4.31}$$

and it can be neglected.

The final field equation for the gravitational field is then given by

$$G_{\mu\nu} = T^{p}_{\mu\nu} = 8\pi\int m(\varphi)\frac{\delta^{(4)}(x-y_p(\lambda))}{\sqrt{-g}}\frac{dy^\alpha_p}{d\lambda}\frac{dy^\beta_p}{d\lambda}d\lambda \ . \tag{4.32}$$

4.2.2 Scalar field equation

The scalar field equation is obtained by varying the action (4.20) with respect to the scalar field

$$\Box\varphi + \frac{16\pi\alpha}{\sqrt{-g}}\frac{\delta S_c}{\delta\varphi} = 16\pi\int m'(\varphi)\frac{\delta^{(4)}(x-y_p(\lambda))}{\sqrt{-g}}d\lambda \ , \tag{4.33}$$

where $m'(\varphi) = dm(\varphi)/d\varphi$. Even in this case, the variation of the coupling term of the action with respect to the field can be neglected, since

$$\frac{16\pi\alpha}{\sqrt{-g}}\frac{\delta S_c}{\delta\varphi} \sim \frac{16\pi\alpha M^{-n}}{\sqrt{-g}}\frac{\delta S_0}{\delta\varphi} \sim \zeta\Box\varphi \ll \Box\varphi \ , \tag{4.34}$$

so that the scalar field equation is given by

$$\Box\varphi = 16\pi\int m'(\varphi)\frac{\delta^{(4)}(x-y_p(\lambda))}{\sqrt{-g}}d\lambda \ . \tag{4.35}$$

The two functions $m(\varphi)$ and $m'(\varphi)$ are evaluated at the value of the scalar field in the location of the particle, which in our case is φ_0, and are determined uniquely by the properties of the secondary. Considering the scalar field equation in a region inside the world-tube of the inspiralling body but far away enough to have a metric which can be written as a perturbation of flat spacetime, the equation (4.35) become:

$$\Box\varphi = 0 \ . \tag{4.36}$$

Thus, in a reference frame $\{\tilde{x}^\mu\}$ centered on the body, the scalar field can be written as:

$$\varphi = \varphi_0 + \frac{m_p d}{\tilde{r}} + O\left(\frac{m_p^2}{\tilde{r}^2}\right) \ , \tag{4.37}$$

where d is the dimensionless scalar charge of the body. Inserting the solution (4.37) inside equation (4.35) and evaluating it at the center of the particle $\tilde{r} = 0$, we obtain

$$\frac{m'(\varphi_0)}{m_p} = -\frac{d}{4} \ . \tag{4.38}$$

Furthermore, since in the weak-field limit the (tt)-component of the particle's stress energy tensor, given by

$$T^{\mathrm{p}\ tt} = 8\pi m(\varphi_0)\delta^{(3)}(x^i - y_p^i(\lambda)) + O\left(\frac{m_p}{\tilde{r}}\right) \ , \tag{4.39}$$

reduces to the matter density of the particle,

$$\rho = m_p\ \delta^{(3)}\left(x^i - y_p^i(\lambda)\right) \ , \tag{4.40}$$

we obtain the relation

$$m(\varphi_0) = m_p \ . \tag{4.41}$$

Hence, replacing the relations (4.38) and (4.41) for the scalar function $m(\varphi)$ in the field equations (4.32) and (4.35), we finally obtain the field equations for the gravitational and the scalar field, given respectively by

$$G_{\mu\nu} = T^{p}_{\mu\nu} = 8\pi m_p \int \frac{\delta^{(4)}(x - y_p(\lambda))}{\sqrt{-g}} \frac{dy_p^{\alpha}}{d\lambda} \frac{dy_p^{\beta}}{d\lambda} d\lambda \ , \tag{4.42}$$

$$\Box\varphi = -4\pi d m_p \int \frac{\delta^{(4)}(x - y_p(\lambda))}{\sqrt{-g}} d\lambda \ . \tag{4.43}$$

These equations are the key ingredients of our approach, and lead to fundamental results. The gravitational field equations, Eqs. (4.42), coincide with those of the GR case (see Eqs. (4.8) and (4.11)). The scalar field equation (4.43), instead, has a source term whose magnitude is controlled by the dimensionless scalar charge carried by the secondary. Therefore, all changes in the EMRI evolution given by the extra scalar field are *uniquely* and *universally* specified by the value of d. For many gravity theories, the latter can be uniquely mapped to the theoretical parameters which control deviations from GR. As we will show in the chapters relative to the parameter estimation analyses, in such cases, future measurements of d with LISA observations, can be translated to constraints on the fundamental parameters that characterize beyond GR theories [116].

The presence of the source term in the scalar field equation causes the emission of extra energy flux, which affects the EMRIs evolution. The gravitational and scalar emissions are computed by solving both the fields in linear perturbation theory, as explained in the next chapter.

We remark that our study considers the leading order in the binary mass ratio only. A first investigation which extends our approach in the EMRI modeling with scalar fields to higher corrections has been recently carried out by [117].

Chapter 5

Linear perturbation theory

In the previous chapter we derived the fields equations for the gravitational and scalar field,

$$G_{\mu\nu} = 8\pi m_p \int \frac{\delta^{(4)}(x - y_p(\lambda))}{\sqrt{-g}} \frac{dy_p^\alpha}{d\lambda} \frac{dy_p^\beta}{d\lambda} d\lambda \ , \tag{5.1}$$

and

$$\Box\varphi = -4\pi d m_p \int \frac{\delta^{(4)}(x - y_p(\lambda))}{\sqrt{-g}} d\lambda \ , \tag{5.2}$$

respectively. In this chapter, we solve such equations in linear perturbation theory. We follow the Teukolsky approach based on the Newman-Penrose formalism which considers perturbations of the curvature. Starting from the Teukolsky equation for a general perturbation with spin s, we first focus on the scalar perturbation with $s = 0$, and then to the gravitational ones with $s = -2$.

5.1 The Teukolsky equation

A general linear field perturbation satisfies the Teukoslsky equation [37]

$$\begin{aligned}
&\left[\frac{\left(r^2+a^2\right)^2}{\Delta} - a^2\sin\theta^2\right]\partial_0^2\psi^{(s)} + \frac{4aMr}{\Delta}\partial_0\partial_\phi\psi^{(s)} + \left[\frac{a^2}{\Delta} - \frac{1}{\sin\theta^2}\right]\partial_\phi^2\psi^{(s)} \\
&- \Delta^{-s}\partial_r\left(\Delta^{s+1}\partial_r\psi^{(s)}\right) - \frac{1}{\sin\theta}\partial_\theta\left(\sin\theta\partial_\theta\psi^{(s)}\right) - 2s\left[\frac{a\left(r-M\right)}{\Delta} + i\frac{\cos\theta}{\sin\theta^2}\right]\partial_\phi\psi^{(s)} \\
&- 2s\left[\frac{2M(r^2-a^2)}{2\Delta} - r - ia\cos\theta\right]\partial_0\psi^{(s)} + (s^2\cot\theta^2 - s)\psi^{(s)} = 4\pi\Sigma T^{(s)} \ ,
\end{aligned} \tag{5.3}$$

where the field $\psi^{(s)}$ stands for the tensorial ($s = -2$) and scalar ($s = 0$) perturbation, respectively,

$$\psi^{(-2)} = (r - ia\cos\theta)^4\,\Psi_4 \ , \qquad \psi^{(0)} = \varphi \ . \tag{5.4}$$

The quantity Ψ_4 is known in the Newman-Penrose formalism as one of the Weyl scalars, a contraction of the Weyl tensor (i.e. the Riemann tensor in vacuum) on

a null tetrad [118]. Ψ_4 describes the only two radiative degrees of freedom and contains all the information regarding the gravitational radiation.

Indeed, considering a gravitational wave on a flat space-time, far from the source, propagating along the z-axis, so that

$$R_{0i0j} = -\frac{1}{2}\ddot{h}^{TT}_{ij} \tag{5.5}$$

where $h^{TT}_{11} = -h^{TT}_{22} = h_+$ and $h^{TT}_{12} = h^{TT}_{21} = h_\times$. The superscripts indicate the transverse traceless gauge, while the "+" and "×" indicate the plus and cross polarization, respectively. The other components of the Riemann tensor vanish. The Weyl scalar Ψ_4 then becomes

$$\Psi_4(r \to \infty) = \frac{1}{2}\left(\ddot{h}_+ - i\ddot{h}_\times\right) \ . \tag{5.6}$$

The source term $T^{(s)}$ is related to the source terms of Eqs. (5.1)-(5.2).

The Teukolsky equation is solved by separating the radial and the angular dependence of both the field perturbation and the source term, and considering the Fourier Transform

$$\psi^{(s)}(t, r, \theta, \phi) = \int \mathrm{d}\omega \sum_{\ell m} \tilde{R}^{(s)}_{\ell m}(r, \omega) S^{(s)}_{\ell m}(\theta, \omega) e^{im\phi} e^{-i\omega t} \ , \tag{5.7}$$

$$4\pi\Sigma T^{(s)} = \int \mathrm{d}\omega \sum_{\ell m} \tilde{J}^{(s)}_{\ell m}(r, \omega) S^{(s)}_{\ell m}(\theta, \omega) e^{im\phi} e^{-i\omega t} \ . \tag{5.8}$$

By inserting these expressions in the Teukolsky equation (5.3), two decoupled equations are obtained, one for the angular and one for the radial dependence of the perturbation. The angular one is given by

$$\left[\frac{1}{\sin\theta}\frac{\mathrm{d}}{\mathrm{d}\theta}\left(\sin\theta\frac{\mathrm{d}}{\mathrm{d}\theta}\right) - \gamma^2\sin^2\theta - \frac{(m + s\cos\theta)^2}{\sin^2\theta} - 2\gamma s\cos\theta + s + 2m\gamma + {}_s\lambda_{\ell m}\right] S^{(s)}_{\ell m}(\theta, \gamma) = 0 \ , \tag{5.9}$$

where $\gamma = a\omega$ and ${}_s\lambda_{\ell m}$ is the spheroidal eigenvalue. The functions $S^{(s)}_{\ell m}$ are known as the spin-weighted spheroidal harmonics, and, for real values of γ, they satisfy the following orthogonality relation

$$\int S^{(s)}_{\ell m}(\theta, \gamma) e^{im\phi} S^{(s)\star}_{\ell' m'}(\theta, \gamma) e^{-im'\phi} \mathrm{d}\Omega = \delta_{\ell\ell'}\delta_{mm'} \ . \tag{5.10}$$

The superscript "$\star$" indicates the complex conjugate and $d\Omega = \sin\theta d\theta d\phi$. The radial equation is given by

$$\Delta^{-s}\frac{\mathrm{d}}{\mathrm{d}r}\left[\Delta^{s+1}\frac{\mathrm{d}\tilde{R}^{(s)}_{\ell m}}{\mathrm{d}r}\right] + \left[\frac{K^2 - 2is(r-M)K}{\Delta} + 4is\omega r - {}_s\lambda_{\ell m}\right]\tilde{R}^{(s)}_{\ell m} = \tilde{J}^{(s)}_{\ell m} \ , \tag{5.11}$$

where $K = (r^2 + a^2)\omega - ma$ and ${}_s\lambda_{\ell m}$ is the spheroidal eigenvalue of Eq. (5.9). The radial function is solved introducing the auxiliary function

$$Y(\omega, r) \equiv \Delta^{s/2}\sqrt{r^2 + a^2}\tilde{R}(\omega, r) \ , \tag{5.12}$$

that reduce the radial equation to a standard Schroedinger-like equation

$$\frac{\mathrm{d}^2}{\mathrm{d}r_\star^2}Y + V(\omega)Y = J_Y \ , \tag{5.13}$$

where the toirtoise coordinate $r_\star$ is defined as

$$\frac{\mathrm{d}r_\star}{\mathrm{d}r} = \frac{r^2+a^2}{\Delta} \tag{5.14}$$

and the expression for the potential is given in Eq. (5.18) and (5.48) for the scalar and gravitational case respectively.

The spheroidal harmonics and their eigenvalue can be obtained with the Leaver method [119]. In our works, we computed them by making use of the Black Hole Perturbation Toolkit, which implemented such method using the software `Mathematica` [120, 121].

In the following sections, we will present separately first the scalar and then the gravitational radial perturbation.

5.2 Scalar perturbations

The radial equation (5.11) for the scalar perturbation with $s = 0$ becomes

$$\frac{\mathrm{d}}{\mathrm{d}r}\left(\Delta\frac{\mathrm{d}\tilde{R}_{\ell m}(r,\omega)}{\mathrm{d}r}\right) + \left(\frac{K^2}{\Delta} - \lambda_{\ell m}\right)\tilde{R}_{\ell m}(r,\omega) = \tilde{J}_{\ell m} \ , \tag{5.15}$$

with $K = (r^2+a^2)\omega - ma$ and $\lambda_{\ell m}$ the angular eigenvalue of Eq. (5.9) with $s = 0$. In the following we drop the multipolar indexes (ℓ, m) for simplicity, unless specified differently. In order to solve the radial equation we use the auxiliary function

$$Y(\omega, r) \equiv \sqrt{r^2+a^2}\tilde{R}(\omega, r) \ , \tag{5.16}$$

so that Eq. (5.15) becomes

$$\frac{\mathrm{d}^2}{\mathrm{d}r_\star^2}Y + V(\omega)Y = J_Y \ , \tag{5.17}$$

where the potential $V(\omega)$ and the source term J_Y are given by

$$V(\omega) = \frac{K^2 - \lambda\Delta}{(r^2+a^2)^2} - G^2 - \frac{\mathrm{d}G}{\mathrm{d}r_\star} \ , \tag{5.18}$$

$$J_Y = \tilde{J}\frac{\Delta}{(a^2+r^2)^{3/2}} \ , \tag{5.19}$$

with $G = r\Delta/(r^2+a^2)^2$ and $r_\star$ is the tortoise coordinate defined by (5.14).

The master equation Eq. (5.17) has the form of a Schroedinger equation with a source term. In perturbation theory, it is solved with the Green functions method, finding the homogeneous solutions first and then integrating them over the source term to find the general solution. The behaviour of the homogeneous master equation at the horizon and at infinity is given by

$$\begin{cases} \dfrac{\mathrm{d}^2}{\mathrm{d}r_\star^2}Y + k^2 Y = 0 & \text{for } r \to r_+ \ , \\ \dfrac{\mathrm{d}^2}{\mathrm{d}r_\star^2}Y + \omega^2 Y = 0 & \text{for } r \to \infty \ , \end{cases} \tag{5.20}$$

where $k = \omega - m\Omega_+$ and Ω_+ is the angular velocity of the horizon, i.e. $\Omega_+ = \frac{a}{2Mr_+}$, with $r_+ = M + \sqrt{M^2 - a^2}$ (see Eq. (3.2)). The homogeneous solutions Y_-/Y_+ which satisfy the conditions of purely ingoing/outgoing wave at the horizon/infinity have the following asymptotic behaviour:

$$\begin{cases} Y_- = e^{-ikr_\star} & \text{for } r \to r_+ \ , \\ Y_- = A_{\rm in} e^{-i\omega r_\star} + A_{\rm out} e^{i\omega r_\star} & \text{for } r \to \infty \ , \end{cases} \tag{5.21}$$

$$\begin{cases} Y_+ = B_{\rm in} e^{-ikr_\star} + B_{\rm out} e^{ikr_\star} & \text{for } r \to r_+ \ , \\ Y_+ = e^{i\omega r_\star} & \text{for } r \to \infty \, . \end{cases} \tag{5.22}$$

The general solution for $Y(\omega, r)$ is then obtained by integrating the former over J_Y:

$$Y = Y_+ \int_{-\infty}^{r_\star} \frac{Y_- J_Y \mathrm{d}r_\star}{W_Y} + Y_- \int_{r_\star}^{+\infty} \frac{Y_+ J_Y \mathrm{d}r_\star}{W_Y} \ , \tag{5.23}$$

where $W_Y = Y_+' Y_- - Y_+ Y_-'$, is the Wronskian and primes denote derivatives with respect to $r_\star$. From Eq. (5.16) we also obtain the asymptotic behavior of $\tilde{R}_{-,+}$:

$$\begin{cases} \tilde{R}_- = \dfrac{e^{-ikr_\star}}{2Mr_+} & \text{for } r \to r_+ \ , \\ \tilde{R}_- = \dfrac{A_{\rm in}}{r} e^{-i\omega r_\star} + \dfrac{A_{\rm out}}{r} e^{i\omega r_\star} & \text{for } r \to \infty \ , \end{cases} \tag{5.24}$$

$$\begin{cases} \tilde{R}_+ = \dfrac{B_{\rm in}}{2Mr_+} e^{-ikr_\star} + \dfrac{B_{\rm out}}{2Mr_+} e^{ikr_\star} & \text{for } r \to r_+ \ , \\ \tilde{R}_+ = \dfrac{e^{i\omega r_\star}}{r} & \text{for } r \to \infty \ . \end{cases} \tag{5.25}$$

A general solution for $\tilde{R}$ can be constructed as in (5.23).

The function Y at infinity and at horizon is then given by

$$\begin{cases} Y(r \to \infty) & = e^{i\omega r_\star} \displaystyle\int_{-\infty}^{+\infty} \frac{Y_- J_Y \mathrm{d}r_\star}{W_Y} \ , \\ Y(r \to r_+) & = e^{-ikr_\star} \displaystyle\int_{-\infty}^{+\infty} \frac{Y_+ J_Y \mathrm{d}r_\star}{W_Y} \ . \end{cases} \tag{5.26}$$

Finally, we define the amplitudes

$$\delta\varphi^{+,-}_{\ell m\omega} = \int_{-\infty}^{+\infty} \frac{Y_{-,+} J_Y \mathrm{d}r_\star}{W_Y} \ , \tag{5.27}$$

which will be used for the computations of the energy and angular momentum fluxes. Before providing the expresisons for such quantities, in the following we focus on the source terms.

5.2.1 Source term for the scalar perturbations

The source term of the scalar field equation Eq. (5.2) is related to the right hand side of the Teukolsky equation (5.3) and can be simplified as

$$\begin{aligned} 4\pi\Sigma T^{(0)} &= -4\pi\Sigma dm_p \int \frac{\delta^{(4)}(x - y_p(\lambda))}{\sqrt{-g}} d\lambda \\ &= -4\pi\Sigma dm_p \int \frac{\delta(t - t_p(\lambda))\delta(r - r_p(\lambda))\delta(\theta - \theta_p(\lambda))\delta(\phi - \phi_p(\lambda))}{\sqrt{-g}} \frac{d\lambda}{dt} dt \\ &= -4\pi dm_p \frac{\delta(r - r_p(t))\delta(\theta - \theta_p(t))\delta(\phi - \phi_p(t))}{\sin\theta \dot{t}} \ , \end{aligned}$$

where $\dot{t} = dt/d\lambda$ is given in Eq. (3.10) and the determinant of the Kerr metric is $g = -\Sigma^2 \sin^2\theta$.

The functions $r_p(t)$, $\theta_p(t)$ and $\phi_p(t)$ describe the orbit of the inspiralling particle. We consider equatorial circular and equatorial eccentric geodesics.

Circular equatorial orbit

For equatorial circular geodesics, the radial and the polar coordinate are fixed $r_p(t) = r_p$, $\theta_p(t) = \pi/2$, and the azimuthal coordinate ϕ is given by $\phi(t) = \omega_p t$, where ω_p is given in Eq. (3.15). Hence, the source term becomes

$$4\pi\Sigma T^{(0)} = -4\pi dm_p \frac{\delta(r - r_p)\delta(\theta - \pi/2)\delta(\phi - \omega_p t)}{|\sin\theta|\dot{t}} .$$

The term $\tilde{J}_{\ell m}$ of Eq. (5.8) is found projecting the source term on the spheroidal harmonics and applying the inverse Fourier transform, i.e.

$$\begin{aligned} \tilde{J}_{\ell m}(\omega, r) &= \frac{1}{2\pi} \int\int \ 4\pi\Sigma T^{(0)} \ S^{\star}_{\ell m}(\theta) e^{-im\phi} e^{i\omega t} d\Omega \ dt \\ &= -4\pi dm_p \frac{S^{\star}_{\ell m}(\pi/2)\delta(\omega - m\omega_p)\delta(r - r_p)}{\dot{t}} \ . \end{aligned} \tag{5.28}$$

The term J_Y can be directly obtained by replacing (5.28) onto Eq. (5.19). Substituting it into (5.27), we find the amplitudes that can be written introducing the terms $\delta\varphi^{+,-}_{\ell m}$ as

$$\delta\varphi^{+,-}_{\ell m\omega} = \delta\varphi^{+,-}_{\ell m}\delta(\omega - m\omega_p) \ . \tag{5.29}$$

The terms $\delta\varphi^{+,-}_{\ell m}$ are then used to compute the scalar emission.

Eccentric equatorial orbit

For equatorial eccentric geodesics, $\theta_p(t)$ is fixed to $\pi/2$, while $r_p(t)$ remains a function of the coordinate time. As done for the circular case, we obtain the terms $\tilde{J}_{\ell m}$ by projecting the source term on the spheroidal harmonics and applying the inverse fourier transform

$$\tilde{J}_{\ell m} = -2d \int_{-\infty}^{+\infty} \frac{m_p \delta[r - r_p(t)]}{\dot{t}} S^{\star}_{\ell m} e^{i[\omega t - m\phi_p(t)]} \mathrm{d}t \ , \tag{5.30}$$

where the spheroidal harmonics $S^{\star}_{\ell m}$ are computed at $\theta = \pi/2$. We find J_Y with Eq. (5.19) and we replace it in the amplitudes (5.27) so that

$$\delta\varphi^{-,+}_{\ell m\omega} = \int_{-\infty}^{+\infty} I^{-,+}\left[r_p(t)\right] e^{i[\omega t - m\phi_p(t)]} dt, \tag{5.31}$$

with

$$I^{-,+}\left[r_p(t)\right] = \left[\frac{Y_{-,+}}{W_Y}\frac{-2dm_p}{(a^2+r^2)^{1/2}}\frac{S^{\star}_{\ell m}}{\dot{t}}\right]_{r=r_p(t)} . \tag{5.32}$$

Finally, we define the functions

$$\alpha(t)^{-,+} = I^{-,+}[r(t)]e^{-im[\phi(t)-\Omega_\phi t]} . \tag{5.33}$$

They are periodic in r with period T_r, and thus they can be expanded as a Fourier series as

$$\alpha(t)^{-,+} = \sum_{n=-\infty}^{+\infty} \hat{\alpha}^{-,+}_n e^{-in\Omega_r t} . \tag{5.34}$$

The frequencies Ω_i with $i = (\phi, r)$ are defined in Eq. (3.39) of Chapter 3. Replacing the expression of $I[r_p(t)]$ in terms of the Fourier expansion of $\alpha(t)$ in Eq. (5.31) and performing the time integral we finally obtain

$$\delta\varphi^{-,+}_{\ell m\omega} = \sum_{n=-\infty}^{+\infty} \delta\hat{\varphi}^{-,+}_{\ell mn}\delta(\omega - \omega_{mn}) , \tag{5.35}$$

where $\omega_{mn} = m\Omega_\phi + n\Omega_r$. The coefficients $\delta\hat{\varphi}^{-,+}_{\ell mn} = 2\pi\alpha_n$ are given by the integral

$$\delta\hat{\varphi}^{-,+}_{\ell mn} = \frac{2\pi}{T_r}\int_0^{T_r} \alpha(t)e^{in\Omega_r t}\mathrm{d}t . \tag{5.36}$$

Substituting the expression (5.33) for $\alpha(t)$ and changing the integration variable from t to χ (defined in Chapter 3) yields:

$$\begin{aligned}\delta\hat{\varphi}^{-,+}_{\ell mn} =& \Omega_r \int_0^{2\pi} \mathrm{d}\chi \frac{\tilde{V}_t(\chi) I^{-,+}(\chi)}{\tilde{J}(\chi)\sqrt{\tilde{V}_r(\chi)}} e^{i[\omega_{mn}t(\chi) - m\phi(\chi)]} \\ =& \Omega_r \int_0^{\pi} \mathrm{d}\chi \frac{\tilde{V}_t(\chi) I^{-,+}(\chi)}{\tilde{J}(\chi)\sqrt{\tilde{V}_r(\chi)}} \left[e^{i[\omega_{mn}t(\chi) - m\phi(\chi)]} + e^{-i\omega_{mn}t(\chi) + im\phi(\chi)}\right] .\end{aligned} \tag{5.37}$$

The amplitudes $\delta\hat{\varphi}^{-,+}_{\ell mn}$ computed through Eq. (5.37) are needed to compute the energy and angular momentum fluxes emitted by the binary.

Due to symmetries in the Teukolsky equation (5.11), the amplitudes $\delta\hat{\varphi}^{+,-}_{\ell mn}$ satisfy the relation

$$\delta\hat{\varphi}^{+,-}_{\ell,-m,-n} = (-1)^\ell \bar{\delta\hat{\varphi}}^{+,-}_{\ell,m,n} , \tag{5.38}$$

where the overbar denotes the complex conjugate.

5.2.2 Energy and angular momentum scalar fluxes

The energy flux associated to the scalar field can be derived through the effective stress-energy tensor for φ, as previously done *e.g.* in [75] and which coincides with the Isaacson tensor in GR [122, 123]. The stress-energy tensor for the scalar field is given in Eq. (4.26) and the energy flux reads:

$$\dot{E}^{\pm}_{\rm scal} = \frac{{\rm d}E^{\pm}_{\rm scal}}{{\rm d}t} = \mp\Delta \int T^{\rm scal}_{tr} {\rm d}\Omega \ , \tag{5.39}$$

where $T^{\rm scal}_{tr} = (16\pi)^{-1}\varphi_{,t}\varphi^{\star}_{,r}$ and the upper (lower) sign indicates the emission at infinity (horizon).

The time derivative of $\varphi = \sum_{\ell,m}\varphi_{\ell m}$ is simply given by $(\varphi_{\ell m})_{,t} = -i\omega_{mn}\varphi_{\ell m}$ (see Eq. (5.7)), while to compute the derivatives with respect to the radial coordinate we note that, for equatorial eccentric orbits,

$$\begin{cases} Y_{\ell m} = \delta\varphi^{+}_{\ell m\omega} e^{i\omega r} & \text{for } r \to \infty \ , \\ Y_{\ell m} = \delta\varphi^{-}_{\ell m\omega} e^{-ikr_\star} & \text{for } r \to r_+ \ , \end{cases} \tag{5.40}$$

therefore

$$\begin{cases} (\varphi^{\star}_{\ell m})_{,r} = -i\omega_{mn}\varphi^{\star}_{\ell m} & \text{for } r \to \infty \ , \\ (\varphi^{\star}_{\ell m})_{,r} = ik_{mn}\dfrac{r^2+a^2}{\Delta}\varphi^{\star}_{\ell m} & \text{for } r \to r_+ \ . \end{cases} \tag{5.41}$$

Using these relations and the orthogonality condition of the spheroidal functions (5.10) we obtain the energy fluxes for the scalar field in the frequency domain:

$$\dot{E}^{(+)}_{\rm scal} = \frac{1}{16\pi}\sum_{\ell,m,n} \omega^2_{mn} |\delta\hat{\varphi}^{+}_{\ell mn}|^2 \ , \tag{5.42}$$

$$\dot{E}^{(-)}_{\rm scal} = \frac{1}{16\pi}\sum_{\ell,m,n} \omega_{mn}k_{mn} |\delta\hat{\varphi}^{-}_{\ell mn}|^2 \ , \tag{5.43}$$

with $k_{mn} \equiv \omega_{mn} - m\Omega_+$.

$$\dot{L}^{(+)}_{\rm scal} = \frac{1}{16\pi}\sum_{\ell,m,n} m\omega_{mn} |\delta\hat{\varphi}^{+}_{\ell mn}|^2 \ , \tag{5.44}$$

$$\dot{L}^{(-)}_{\rm scal} = \frac{1}{16\pi}\sum_{\ell,m,n} mk_{mn} |\delta\hat{\varphi}^{-}_{\ell mn}|^2 \ . \tag{5.45}$$

Expressions for equatorial circular orbits can be straightforwardly obtained from the previous ones, replacing ω_{mn} with $m\omega_p$, k_{mn} with $k \equiv m\omega_p - m\Omega_+$, the amplitudes $\delta\hat{\varphi}^{-}_{\ell mn}$ with $\delta\varphi_{\ell m}$ of Eq. (5.29).

5.3 Gravitational perturbations

The radial equation (5.11) for the gravitational perturbation with $s = -2$ becomes

$$\Delta^2 \frac{\rm d}{{\rm d}r}\left(\frac{1}{\Delta}\frac{{\rm d}\tilde{R}_{\ell m\omega}}{{\rm d}r}\right) + \left(\frac{K^2 + 4i(r-M)K}{\Delta} - 8i\omega r - \lambda\right)\tilde{R}_{\ell m\omega}(r) = I_{\ell m\omega}(r) \ , \tag{5.46}$$

with $K = (r^2 + a^2)\omega - ma$ and λ is the angular eigenvalue of Eq.(5.9) with $s = -2$. The source term $I_{\ell m\omega}$ corresponds to $\tilde{J}_{\ell m}$ of Eq. (5.11) and it is treated in Section 5.3.1.

As done for the scalar case, we define the auxiliary function

$$Y = \Delta^{-1}\sqrt{r^2 + a^2}\tilde{R} \,, \tag{5.47}$$

so that the homogeneous radial equation takes the form of the Schroedinger-like equation

$$\frac{d^2}{dr_\star^2}Y + \frac{K^2 + 4i(r-M)K - \Delta(8i\omega r + \lambda)}{(r^2+a^2)^2 - G^2 - dG/dr_\star}Y = 0, \tag{5.48}$$

where G is defined as

$$G \equiv \frac{-2(r-M)}{r^2+a^2} + \frac{r\Delta}{(r^2+a^2)^2}, \tag{5.49}$$

and $r_\star$ is defined in (5.14).

The homogeneous solutions Y_-, which satisfies the condition of purely ingoing wave at the horizon, and Y_+, which satisfies the condition of purely outgoing wave at infinity, have the following asymptotic behaviour:

$$\begin{cases} Y_- = \tilde{B}^{hole}_{\ell m\omega}\Delta e^{-ikr_\star} & \text{for } r \to r_+ \,, \\ Y_- = \dfrac{B^{in}_{\ell m\omega}}{r^2}e^{-i\omega r_\star} + B^{out}_{\ell m\omega}r^2 e^{i\omega r_\star} & \text{for } r \to \infty \,, \end{cases} \tag{5.50}$$

$$\begin{cases} Y_+ = \tilde{D}^{in}_{\ell m\omega}\Delta e^{-ikr_\star} + \tilde{D}^{out}_{\ell m\omega}\Delta e^{ikr_\star} & \text{for } r \to r_+ \,, \\ Y_+ = D^{\infty}_{\ell m\omega}r^2 e^{i\omega r_\star} & \text{for } r \to \infty \,, \end{cases} \tag{5.51}$$

where $k = \omega - m\Omega_+$ and $\Omega_+ = a/(2Mr_+)$. From the relation (5.47) between $\tilde{R}$ and Y we obtain the boundary condition for the homogeneous solutions:

$$\begin{cases} \tilde{R}^-_{\ell m\omega} = B^{hole}_{\ell m\omega}\Delta^2 e^{-ikr_\star} & \text{for } r \to r_+ \,, \\ \tilde{R}^-_{\ell m\omega} = \dfrac{B^{in}_{\ell m\omega}}{r}e^{-i\omega r_\star} + B^{out}_{\ell m\omega}r^3 e^{i\omega r_\star} & \text{for } r \to \infty \,, \end{cases} \tag{5.52}$$

$$\begin{cases} \tilde{R}^+_{\ell m\omega} = D^{in}_{\ell m\omega}\Delta^2 e^{-ikr_\star} + D^{out}_{\ell m\omega}e^{ikr_\star} & \text{for } r \to r_+ \,, \\ \tilde{R}^+_{\ell m\omega} = D^{\infty}_{\ell m\omega}r^3 e^{i\omega r_\star} & \text{for } r \to \infty \,. \end{cases} \tag{5.53}$$

where $B^{hole}_{\ell m\omega} = \tilde{B}^{hole}_{\ell m\omega}/(2Mr_+)$, $D^{in(out)}_{\ell m\omega} = \tilde{D}^{in(out)}_{\ell m\omega}/(2Mr_+)$. Finally, the general solution for $\tilde{R}_{\ell m\omega}$ is given by $\tilde{R}_{\ell m\omega}(r) = Z^-_{\ell m\omega}(r)\tilde{R}^+_{\ell m\omega}(r) + Z^+_{\ell m\omega}(r)\tilde{R}^-_{\ell m\omega}(r)$ where, following [68],

$$Z^-_{\ell m\omega}(r) = \frac{1}{2i\omega B^{in}_{\ell m\omega}D^{\infty}_{\ell m\omega}}\int_{r_+}^{r} \mathrm{d}r' \frac{\tilde{R}^-_{\ell m\omega}(r')I_{\ell m\omega}(r')}{\Delta(r')^2} \,, \tag{5.54}$$

$$Z^+_{\ell m\omega}(r) = \frac{1}{2i\omega B^{in}_{\ell m\omega}D^{\infty}_{\ell m\omega}}\int_{r}^{\infty} \mathrm{d}r' \frac{\tilde{R}^+_{\ell m\omega}(r')I_{\ell m\omega}(r')}{\Delta(r')^2} \,. \tag{5.55}$$

Defining $Z^-_{\ell m\omega} \equiv Z^-_{\ell m\omega}(r \to \infty)$, $Z^+_{\ell m\omega} \equiv Z^+_{\ell m\omega}(r \to r_+)$, the asymptotic radial solutions read:

$$\tilde{R}_{\ell m\omega}(r \to \infty) = Z^-_{\ell m\omega}D^{\infty}_{\ell m\omega}r^3 e^{i\omega r_\star} \,, \tag{5.56}$$

$$\tilde{R}_{\ell m\omega}(r \to r_+) = Z^+_{\ell m\omega}B^{hole}_{\ell m\omega}\Delta^2 e^{-ikr_\star} \,. \tag{5.57}$$

It is convenient to absorb the factors $D^{\infty}_{\ell m\omega}$ and $B^{hole}_{\ell m\omega}$ into $Z^{-}_{\ell m\omega}$ and $Z^{+}_{\ell m\omega}$, such that:

$$Z^{-}_{\ell m\omega}(r) = \frac{1}{2i\omega B^{in}_{\ell m\omega}} \int_{r_+}^{r} \mathrm{d}r' \frac{\tilde{R}^{-}_{\ell m\omega}(r') I_{\ell m\omega}(r')}{\Delta(r')^2} \ , \tag{5.58}$$

$$Z^{+}_{\ell m\omega}(r) = \frac{B^{hole}_{\ell m\omega}}{2i\omega B^{in}_{lm\omega} D^{\infty}_{\ell m\omega}} \int_{r}^{\infty} \mathrm{d}r' \frac{\tilde{R}^{+}_{\ell m\omega}(r') I_{lm\omega}(r')}{\Delta(r')^2} \ , \tag{5.59}$$

and

$$\tilde{R}_{\ell m\omega}(r \to \infty) = Z^{-}_{\ell m\omega} r^3 e^{i\omega r_\star} \ , \tag{5.60}$$

$$\tilde{R}_{\ell m\omega}(r \to r_+) = Z^{+}_{\ell m\omega} \Delta^2 e^{-ikr_\star} \ . \tag{5.61}$$

The coefficients $Z^{-,+}_{\ell m\omega}$ are needed to calculate the energy flux at horizon and at infinity. However, since in Eq. (5.52) the outgoing solution grows with a coefficient r^4 relative to the ingoing coefficient, the ingoing solution is completely swamped, and obtaining $B^{in}_{\ell m}$ is extremely challenging. The reason for this difficulty is that the potential $V(r)$ in Eq. (5.46) of the Teukolsky equation is long ranged. Sasaki & Nakamura [124] found a solution to this problem by transforming the Teukolsky equation into an equation featuring a short-ranged potential. Other possible methods to solve the Teukolsky equation are the Mano-Suzuki-Takasugi method [125] and an approach that makes use of a hyperboloidal foliation [126, 127].

5.3.1 Source term for the gravitational perturbations

The source term for the gravitational perturbations is given by

$$I_{\ell m\omega}(r) = 4 \int d\Omega dt \frac{\Sigma}{\rho^4} (B'_2 + B'^{*}_2) S_{\ell m\omega}(\theta) e^{-im\phi} e^{i\omega t}, \tag{5.62}$$

with

$$B'_2 = -\frac{\rho^8 \bar{\rho}}{2} L_{-1} \left[\rho^{-4} L_0 \left(\rho^{-2} \bar{\rho}^{-1} T_{nn}\right)\right] - \frac{\Delta^2 \rho^8 \bar{\rho}}{2\sqrt{2}} L_{-1} \left[\rho^{-4} \bar{\rho}^2 J_+ \left(\rho^{-2} \bar{\rho}^{-2} \Delta^{-1} T_{n\bar{m}}\right)\right], \tag{5.63}$$

$$B'^{*}_2 = -\frac{\Delta^2 \rho^8 \bar{\rho}}{2\sqrt{2}} J_+ \left[\rho^{-4} \bar{\rho}^2 \Delta^{-1} L_{-1} \left(\rho^{-2} \bar{\rho}^{-2} T_{n\bar{m}}\right)\right] - \frac{\Delta^2 \rho^8 \bar{\rho}}{4} J_+ \left[\rho^{-4} J_+ \left(\rho^{-2} \bar{\rho} T_{\bar{m}\bar{m}}\right)\right], \tag{5.64}$$

and $\rho = 1/(r - ia\cos\theta)$, $\bar{\rho} = 1/(r + ia\cos\theta)$. The two operators J_+ and L_s, together with its hermitian conjugate $L^{\dagger}_s$, are defined as:

$$J_+ = \partial_r + \frac{iK(r)}{\Delta}, \tag{5.65}$$

$$L_s = \partial_\theta + m\csc\theta - a\omega\sin\theta + s\cot\theta, \tag{5.66}$$

$$L^{\dagger}_s = \partial_\theta - m\csc\theta + a\omega\sin\theta + s\cot\theta. \tag{5.67}$$

The functions B'_2 and B'^{*}_2 depend on the stress-energy tensor of the inspiralling particle, which is given in (4.11). Integrating it in dt, it becomes

$$T^{\alpha\beta}(r,\theta,\phi,t) = m_p \frac{u^\alpha u^\beta}{\Sigma \sin\theta \dot{t}} \delta[r - r(t)]\delta[\theta - \theta(t)]\delta[\phi - \phi(t)], \tag{5.68}$$

where $\dot{t}$ is given in (3.6). The components T_{nn}, $T_{n\bar{m}}$ and $T_{\bar{m}\bar{m}}$ present in the eq. (5.63) and (5.64) are obtained by projecting the stress-energy tensor $T^{\alpha\beta}$ onto the Newman-Penrose null tetrad legs $\mathbf{n}$, $\bar{\mathbf{m}}$: $T_{nn} = T^{\alpha\beta} n_\alpha n_\beta$, *etc.* The components of the null tetrad legs are given by [118]:

$$n_\alpha = \frac{1}{2}\left(\frac{\Delta}{\Sigma}, 1, 0, -\frac{a\Delta \sin^2\theta}{\Sigma}\right), \tag{5.69}$$

$$\bar{m}_\alpha = \frac{\rho}{2}\left(ia\sin\theta, 0, \Sigma, -i(r^2+a^2)\sin\theta\right). \tag{5.70}$$

Hence, the components of the projected stress-energy tensor are given by:

$$T_{ab} = \frac{C_{ab}}{\sin\theta}\delta[r - r(t)]\delta[\theta - \theta(t)]\delta[\phi - \phi(t)], \tag{5.71}$$

where the coefficients C_{ab} are

$$C_{nn} = \frac{m_p}{4\Sigma^3 \dot{t}}\left[E(r^2+a^2) - aL_z\right]^2, \tag{5.72}$$

$$C_{n\bar{m}} = -\frac{m_p \rho}{2\sqrt{2}\Sigma^2 \dot{t}}\left[E(r^2+a^2) - aL_z\right]\left[i\sin\theta\left(aE - \frac{L_z}{\sin^2\theta}\right) + \Sigma\frac{d\theta}{d\tau}\right], \tag{5.73}$$

$$C_{\bar{m}\bar{m}} = \frac{m_p \rho^2}{2\Sigma \dot{t}}\left[i\sin\theta\left(aE - \frac{L_z}{\sin^2\theta}\right) + \Sigma\frac{d\theta}{d\tau}\right]. \tag{5.74}$$

As written, the sign of $d\theta/d\tau$, which square is given in Eq.(3.4), is ambiguous, depending on whether θ is increasing or decreasing. However, in the following we will focus on equatorial orbits only, for which $d\theta/d\tau = 0$.

In the following, we consider the three different types of orbits and we present the analytic form of the source term in the three cases.

Circular equatorial orbit

For the equatorial circular case $r_p(t) = r_p$, $\theta_p(t) = \pi/2$, and $\phi(t) = \omega_p t$, where ω_p is given in Eq.(3.15). Hence, the source term becomes

$$I_{\ell m\omega}(r) = \int dt \Delta^2 e^{i[\omega t - m\omega_p]}\left[\left[A_{nn0} + A_{n\bar{m}0} + A_{\bar{m}\bar{m}0}\right]\delta(r - r_p) + \right.$$
$$\left. \partial_r\left(\left[A_{n\bar{m}1} + A_{\bar{m}\bar{m}1}\right]\delta(r - r_p)\right) + \partial_r^2\left[A_{\bar{m}\bar{m}2}\ \delta(r - r_p)\right]\right], \tag{5.75}$$

with

$$A_{nn0} = -\frac{2\rho^{-2}\bar{\rho}^{-1}C_{nn}}{\Delta^2} L_1^\dagger \left(\rho^{-4} L_2^\dagger(\rho^3 S_{\ell m})\right) \ , \tag{5.76}$$

$$A_{n\bar{m}0} = -\frac{2\sqrt{2}\rho^{-3}C_{n\bar{m}}}{\Delta}\left[\left(\frac{iK}{\Delta}+\rho+\bar{\rho}\right) L_2^\dagger S_{\ell m} - \left(\frac{K}{\Delta}\right) a\sin\theta S_{\ell m}(\bar{\rho}-\rho)\right] \ , \tag{5.77}$$

$$A_{\bar{m}\bar{m}0} = -S_{\ell m}\rho^{-3}\bar{\rho}C_{\bar{m}\bar{m}}\left[-\left(\frac{K}{\Delta}\right)^2 + 2i\rho\frac{K}{\Delta} - i\partial_r\left(\frac{K}{\Delta}\right)\right] \ , \tag{5.78}$$

$$A_{n\bar{m}1} = \frac{2\sqrt{2}\rho^{-3}C_{n\bar{m}}}{\Delta}\left[L_2^\dagger S_{\ell m} + ia\rho\sin\theta(\bar{\rho}-\rho)S_{\ell m}\right] \ , \tag{5.79}$$

$$A_{\bar{m}\bar{m}1} = -2S_{\ell m}\rho^{-3}\bar{\rho}C_{\bar{m}\bar{m}}\left(\rho+\frac{iK}{\Delta}\right) \ , \tag{5.80}$$

$$A_{\bar{m}\bar{m}2} = -S_{\ell m}\rho^{-3}\bar{\rho}C_{\bar{m}\bar{m}} \ , \tag{5.81}$$

and the C coefficients are given in Eqs. (5.72)-(5.74) with $\theta = \pi/2$ and $d\theta/d\tau = 0$. By inserting the expression of $I_{\ell m\omega}$ in (5.59) and (5.58) and integrating in the radial and the time coordinate, we obtain the final form of the amplitudes $Z^{-,+}_{\ell m}$ for equatorial circular orbits:

$$Z^-_{\ell m\omega} = \frac{\pi\delta(\omega-m\omega_p)}{i\omega B^{in}_{\ell mk}}\Bigg[R^-_{\ell m\omega}\left(A_{nn0}+A_{n\bar{m}0}+A_{\bar{m}\bar{m}0}\right) - \frac{dR^-_{\ell m\omega}}{dr}\left(A_{n\bar{m}1}+A_{\bar{m}\bar{m}1}\right) + \frac{d^2R^-_{\ell m\omega}}{dr^2}A_{\bar{m}\bar{m}2}\Bigg] \ , \tag{5.82}$$

$$Z^+_{lm\omega} = -\frac{\pi c_0\delta(\omega-m\omega_p)}{4i\omega^3 d_{\ell m}B^{in}_{\ell m}}\Bigg[R^+_{\ell m\omega}\left(A_{nn0}+A_{n\bar{m}0}+A_{\bar{m}\bar{m}0}\right) - \frac{dR^+_{\ell m\omega}}{dr}\left(A_{n\bar{m}1}+A_{\bar{m}\bar{m}1}\right) + \frac{d^2R^+_{\ell m\omega}}{dr^2}A_{\bar{m}\bar{m}2}\Bigg] \ . \tag{5.83}$$

Here the functions $R^{-,+}_{lm}$ and their derivatives are calculated at $r = r_p$.

Eccentric equatorial orbit

For equatorial eccentric geodesics $\theta_p(t) = \pi/2$. Hence, the source term becomes [70]

$$Z^{-,+}_{\ell m\omega} = \frac{m_p}{2i\omega B^{in}}\int_{-\infty}^{\infty} \mathrm{d}t e^{i\omega t - im\phi(t)} I^{-,+}_{\ell m\omega}[r(t),\theta(t)] \ , \tag{5.84}$$

where

$$I^{-,+}_{\ell m\omega} = \Bigg[R^{in,up}_{\ell m\omega}\{A_{nn0}+A_{\bar{m}n0}+A_{\bar{m}\bar{m}0}\} - \frac{dR^{in,up}_{\ell m\omega}}{dr}\{A_{\bar{m}n1}+A_{\bar{m}\bar{m}1}\} + \frac{d^2R^{in,up}_{\ell m\omega}}{dr^2}A_{\bar{m}\bar{m}2}\Bigg]_{r=r(t),\theta=\theta(t)} \ . \tag{5.85}$$

Introducing u as the inverse of the orbital radius, so that $u(\chi,p,e)=(1+e\cos\chi)/p$, the coefficients A are given by

$$\begin{aligned}
A_{\bar{m}n0}(u) =&\frac{2}{\sqrt{\pi}}\frac{C_{\bar{m}n}}{u(1-2Mu+a^2u^2)^2}\left[2a^2u^3+\left[ia(a\omega-m)-4M\right]u^2+2u+i\omega\right]\\
&\times\left[\frac{\partial S}{\partial\theta}(\pi/2)+(a\omega-m)S_{\ell m}(\pi/2)\right]\,,\\
A_{\bar{m}\bar{m}0}(u) =&\frac{1}{\sqrt{2\pi}}\frac{C_{\bar{m}\bar{m}}S(\pi/2)}{u^2(1-2Mu+a^2u^2)^2}\Big\{-2ia^3(a\omega-m)u^5+a(a\omega-m)\{6iM\\
&+a(a\omega-m)\}u^4-4ia(a\omega-m)u^3+2\omega\{iM+a(a\omega-m)\}u^2-2i\omega u+\omega^2\Big\}\,,\\
A_{\bar{m}n1}(u) =&\frac{2}{\sqrt{\pi}}\frac{C_{\bar{m}n}}{u(1-2Mu+a^2u^2)}\left[\frac{\partial S}{\partial\theta}(\pi/2)+(a\omega-m)S(\pi/2)\right]\,,\\
A_{\bar{m}\bar{m}1}(u) =&-\sqrt{\frac{2}{\pi}}\frac{C_{\bar{m}\bar{m}}S(\pi/2)}{u^2(1-2Mu+a^2u^2)}\left[a^2u^3+\{ia(a\omega-m)-2M\}u^2+u+i\omega\right]\,,\\
A_{\bar{m}\bar{m}2}(u) =&-\frac{1}{\sqrt{2\pi}}\frac{C_{\bar{m}\bar{m}}S(\pi/2)}{u^2}\,,\\
A_{nn0}(u) =&-\sqrt{\frac{2}{\pi}}\frac{C_{nn}}{(1-2Mu+a^2u^2)^2}\Big\{-2ia\left(\frac{\partial S}{\partial\theta}(\pi/2)+(a\omega-m)S(\pi/2)\right)u\\
&+\frac{\partial^2 S}{\partial\theta^2}(\pi/2)+2(a\omega-m)\frac{\partial S}{\partial\theta}(\pi/2)+\{(a\omega-m)^2-2\}S(\pi/2)\Big\}\,,
\end{aligned}\tag{5.86}$$

where

$$\begin{aligned}
C_{nn}(\chi,p,e) =&\frac{J(\chi,p,e)}{4p^4\tilde{V}_t(\chi,p,e)}\left[p^2E-ax(1+e\cos\chi)^2+ep\sin\chi\sqrt{\tilde{V}_r(\chi,p,e)}\right]^2\,,\\
C_{\bar{m}n}(\chi,p,e) =&\frac{ixJ(\chi,p,e)}{2\sqrt{2}p^3\tilde{V}_t(\chi,p,e)}(1+e\cos\chi)\Big[p^2E-ax(1+e\cos\chi)^2+\\
&ep\sin\chi\sqrt{\tilde{V}_r(\chi,p,e)}\Big]\,,\\
C_{\bar{m}\bar{m}}(\chi,p,e) =&-\frac{x^2J(\chi,p,e)}{2p^2\tilde{V}_t(\chi,p,e)}(1+e\cos\chi)^2\,.
\end{aligned}$$

The terms $J(\chi,p,e)$, $\tilde{V}_t(\chi,p,e)$ and $\tilde{V}_r(\chi,p,e)$ are given in Chapter 3, Eq. (3.38). Finally, we note that recasting Eq. (5.84) in term of the variable χ, the integral can be written as

$$\begin{aligned}
Z^{+,-}_{\ell mn}=\frac{m_p\Omega_r}{2i\omega_{mn}B^{in}}\int_0^\pi \mathrm{d}\chi\frac{\tilde{V}_t(\chi)}{J(\chi)\sqrt{\tilde{V}_r(\chi)}}\Big[&I^{+,-}_{\ell m\omega(+)}(r(\chi))e^{i\omega_{mn}t(\chi)-im\phi(\chi)}+\\
&I^{+,-}_{\ell m\omega(-)}(r(\chi))e^{-i\omega_{mn}t(\chi)+im\phi(\chi)}\Big]\,,
\end{aligned}\tag{5.87}$$

where the subscripts $(\pm)$ imply the substitution $\sin\chi \to \pm\sin\chi$ in the functions $I^{+,-}_{\ell m\omega}$.

Due to symmetries in the Teukolsky equation (5.11), the amplitudes $Z^{+,-}_{\ell mn}$ satisfy the relation

$$Z^{+,-}_{\ell,-m,-n} = (-1)^{\ell}\bar{Z}^{+,-}_{\ell,m,n} \ , \tag{5.88}$$

where the overbar denotes the complex conjugate.

5.3.2 Energy and angular momentum gravitational fluxes

The gravitational energy flux can be computed in terms of the Isaacson stress-energy tensor [128], and is given by

$$\left(\frac{\mathrm{d}^2E}{\mathrm{d}A\mathrm{d}t}\right)^{\mathrm{rad}}_{r\to\infty} = \frac{1}{16\pi}\left\langle \left(\frac{\partial h_+}{\partial t}\right)^2 + \left(\frac{\partial h_\times}{\partial t}\right)^2 \right\rangle \ , \tag{5.89}$$

where the brackets $\langle ...\rangle$ denote an average over a region of spacetime large compered with the wavelenght of the radiation, and the plus and cross polarizations h_+ and $h_\times$ are obtained from the evaluation of the Weyl scalar Ψ_4 at infinity, see Eq. (5.6). The expression for Ψ_4 is found combining Eqs. (5.4) and (5.7), with $R_{\ell m\omega}$ in the limit $r\to\infty$ is given in Eq. (5.60).

The final expressions for the energy and angular momentum fluxes at infinity are then given by

$$\left(\frac{dE}{dt}\right)^{rad}_{r\to\infty} = \sum_{\ell mn}\frac{|Z^-_{\ell mn}|^2}{4\pi\omega^2_{mn}} \ , \tag{5.90}$$

$$\left(\frac{dL}{dt}\right)^{rad}_{r\to\infty} = \sum_{\ell mn}\frac{m|Z^-_{\ell mn}|^2}{4\pi\omega^3_{mn}} \ . \tag{5.91}$$

The frequencies ω_{mn} are written in Eq. (3.40) and the amplitude Z^- in Eq.(5.87).

The fluxes at the horizon can be calculated by measuring the rate at which the event horizon's area increases as radiation falls into it, following the prescription of [129] as described in [37]. The result reads:

$$\left(\frac{dE}{dt}\right)^{rad}_{r\to r_+} = \sum_{\ell mn}\alpha_{\ell mn}\frac{|Z^+_{\ell mn}|^2}{4\pi\omega^2_{mn}} \ , \tag{5.92}$$

$$\left(\frac{dL}{dt}\right)^{rad}_{r\to r_+} = \sum_{\ell mn}\alpha_{\ell mn}\frac{m|Z^+_{\ell mn}|^2}{4\pi\omega^3_{mn}} \tag{5.93}$$

where the coefficients $\alpha_{\ell mn}$ are given by

$$\alpha_{\ell mn} = \frac{256(2Mr_+)^5 k_{mn}(k^2_{mn}+4\epsilon^2)(k^2_{mn}+16\epsilon^2)\omega^3_{mn}}{|C_{\ell mn}|^2} \ , \tag{5.94}$$

with $k_{mn} = \omega_{mn} - m\Omega_+$,

$$\epsilon = \frac{\sqrt{M^2-a^2}}{4Mr_+} \ , \tag{5.95}$$

and

$$|C_{\ell mn}|^2 = [(\lambda+2)^2 + 4a\omega_{mn} - 4a^2\omega_{mn}^2](\lambda^2 + 36ma\omega_{mn} - 36a^2\omega_{mn}^2) + (2\lambda+3)(96a^2\omega_{mn}^2 - 48ma\omega_{mn}) + 144\omega_{mn}^2(M^2-a^2) \ . \tag{5.96}$$

The total energy and angular momentum fluxes are given by the sum of the gravitational and scalar terms at horizon $(-)$ and at infinity $(+)$:

$$\dot{C}_{\rm GW} = \sum_{i=+,-} [\dot{C}^{(i)}_{\rm grav} + \dot{C}^{(i)}_{\rm scal}] \ = \dot{C}_{\rm grav} + \dot{C}_{\rm scal} \ , \tag{5.97}$$

where $C \in [E, L]$, $\dot{C}_{\rm grav} \equiv \dot{C}^{(+)}_{\rm grav} + \dot{C}^{(-)}_{\rm grav}$, $\dot{C}_{\rm scal} \equiv \dot{C}^{(+)}_{\rm scal} + \dot{C}^{(-)}_{\rm scal}$ and the dot indicates the time derivative.

Finally, because of the linear dependence of the source term from the scalar charge, it is worth to remark that the total scalar flux for a given scalar charge simply scales with d as

$$\dot{C}_{\rm scal} = d^2 \dot{\bar{C}}_{\rm scal} \ ,$$

where $\dot{\bar{C}}_{\rm scal}$ only depends on (p, e, a).

With the approach of linear perturbation theory, we showed how to compute the emission through gravitational and scalar waves which arise from the motion of the inspiralling object on the Kerr background. The following two chapters are dedicated to the numerical computation of the fluxes and their use to build the EMRI adiabatic orbital evolution and the emitted GW signals, for equatorial circular and eccentric inspirals.

Chapter 6

EMRIs with massless scalar fields: Circular equatorial orbits

Here, we present a model of EMRIs with massless scalar field in circular orbits around Kerr black holes. We compute the energy emission through gravitational and scalar waves, which is presented in the first section. In the second one, we build the adiabatic EMRI's orbital evolution, and we asses how the presence of the scalar charge affects the binary dynamics. Finally, in the last section, we model the gravitational wave templates and we compute the the mismatch from signals emitted with and without the scalar charge, in order to estimate the LISA capability to detect the new scalar field.

6.1 Energy emission

Both the gravitational and scalar energy fluxes for circular orbits have been computed with the software `Mathematica` [121] by making use of the Black Hole Perturbation Toolkit [120], which allows to rapidly generate fluxes with high accuracy. The total energy emission is given by the sum of the gravitational and the scalar flux at the horizon $(-)$ and at infinity $(+)$:

$$\dot{E}_{\rm GW} = \sum_{i=+,-} [\dot{E}^{(i)}_{\rm grav} + \dot{E}^{(i)}_{\rm scal}] \ = \dot{E}_{\rm grav} + \dot{E}_{\rm scal} \ , \tag{6.1}$$

where, $\dot{E}_{\rm grav} \equiv \dot{E}^{(+)}_{\rm grav} + \dot{E}^{(-)}_{\rm grav}$ and $\dot{E}_{\rm scal} \equiv \dot{E}^{(+)}_{\rm scal} + \dot{E}^{(-)}_{\rm scal}$. We stress that both the gravitational and the scalar fluxes of the EMRI with mass ratio q scale as q^2. Moreover, we define $\dot{\bar{E}}_{\rm scal}$ such that

$$\dot{E}_{\rm scal} = d^2 \dot{\bar{E}}_{\rm scal} \ , \tag{6.2}$$

so that $\dot{\bar{E}}_{\rm scal}$ only depends on $(r/M, a/M)$.

The results are shown in Figs. 6.1 and 6.2.

The top panel of Fig. 6.1 shows the behaviour of the total scalar energy flux, normalized with the mass ratio, as a function of the circular orbit's radius for different values of the scalar charge d and for a primary spin $a = 0.9M$. The behavior of $\dot{E}_{\rm scal}$ is qualitatively similar to that shown in [44], where the central BH is non-spinning.

As for the gravitational emission, the scalar flux increases monotonically with the shrinking of the orbit.

The bottom panel of Fig. 6.1 shows the ratio between the scalar and gravitational components of the GW flux, for the same binary configurations of the top picture. The ratio decreases as the orbital radius shrinks, with the gravitational contribution growing in time faster than the scalar contribution, at small separation.

Figure 6.1 also shows that for $d > 0.01$ the scalar flux $\dot{E}_{\rm scal}$ ranges between 0.1% and 1% of the gravitational flux $\dot{E}_{\rm grav}$. Therefore, we expect the scalar charge to induce a significant contribution on the EMRI evolution when integrated over the all inspiral phase, which is investigated in the next section.

Fig. 6.2 shows the ratio $\dot{E}_{\rm scal}/\dot{E}_{\rm grav}$, rescaled by d^2, as a function of the primary BH spin, and the absolute value of $\dot{E}_{\rm scal}$. It is interesting to note that while for a fixed radius r/M, larger a/M lead to slightly smaller values of the scalar flux (this is also true for the gravitational component), the overall emission increases due to the larger range of frequencies spanned by the binary. Indeed, for higher spins, the inspiralling body can reach values of the orbital radius closer to the MBH's horizon before plunging. From the bottom panel of the figure we also observe that for a fixed orbital radius, the ratio between the scalar and the gravitational flux slightly increases with the increasing of the MBH's spin.

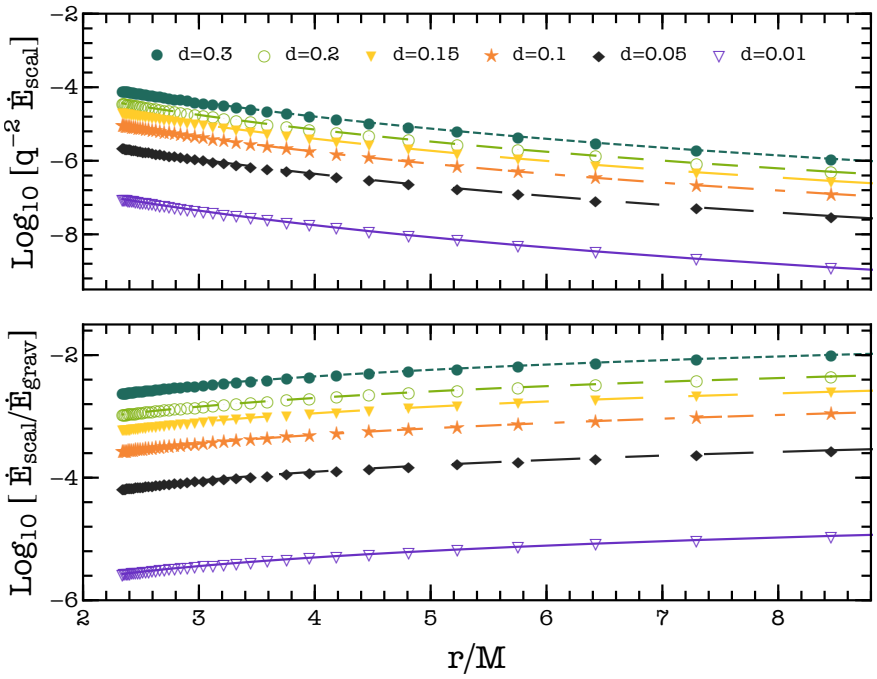

Figure 6.1. (Top) Scalar energy flux, normalized with the mass-ratio, as a function of the orbital radius, for different values of the scalar charge. The spin of the primary is $a/M = 0.9$. (Bottom) Ratio of the scalar and gravitational energy flux as a function of the orbital radius for different values of the scalar charge, and $a/M = 0.9$.

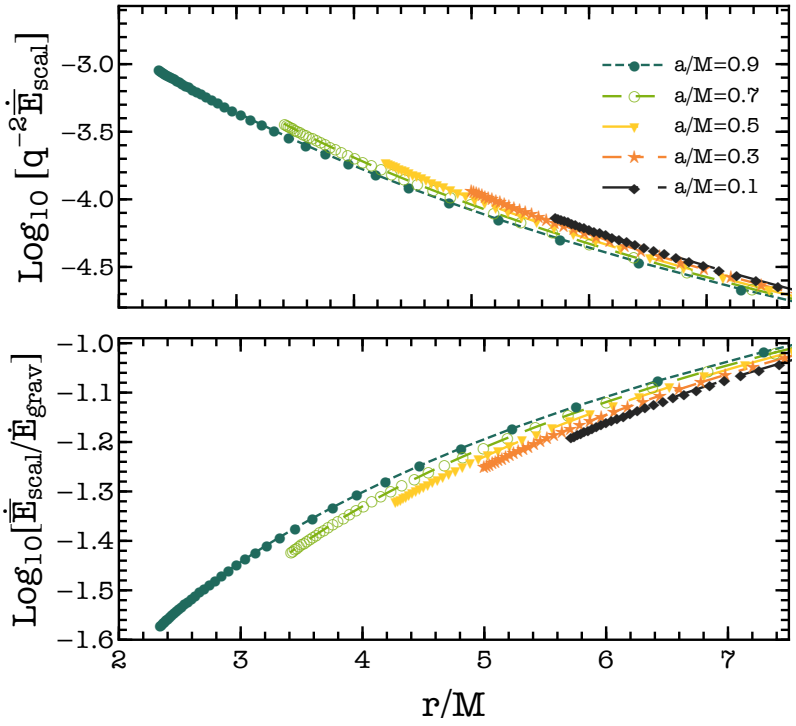

Figure 6.2. Same as Fig. 6.1 for different values of the primary spin a/M.

6.2 Orbital evolution

At leading order in the mass ratio (adiabatic order), the inspiral is driven by the energy emission through gravitational and scalar waves. For the integral of motion E relative to each geodesic we can impose the balance law:

$$\dot{E} = -\dot{E}_{GW}. \tag{6.3}$$

The time and phase field equation are then given by:

$$\frac{dr}{dt} = -\dot{E}\frac{dr}{dE_{\rm orb}} \quad , \quad \frac{d\Phi}{dt} = \omega_{\rm p} \ , \tag{6.4}$$

where $E_{\rm orb}$ is the orbital energy of the particle, given by Eq. (3.11), and $\omega_{\rm p}$ is the frequency of the particle related to the orbital radius and MBH's spin from Eq.(3.15). By integrating such equations, we obtain the time evolution of $(r(t), \phi(t))$. The presence of the scalar charge affects such evolution accelerating the EMRI coalescence due to the extra scalar energy emission.

The emitted GW signal is related to the orbital phase evolution, which means that the presence of a scalar charge will then introduce a dephasing of the GW-template, which could be possibly detected by the space interferometers if it is above a certain threshold. By following [130] and [131], such threshold is given by,

$$\Delta\Psi_{thr} \simeq \frac{\sqrt{D-1}}{\rho} \tag{6.5}$$

where D is the number of intrinsic parameter of the binary source, and ρ the signal to noise ratio (SNR) of the signal. The intrinsic parameters for our EMRI systems are

$\vec{\theta} = \{M, m_p, a/M, d_L, \theta_S, \phi_S, \theta_L, \phi_L, r_0, \phi_0, d\}$, where (r_0, ϕ_0) are the initial radius and phase, d_L is the luminosity distance of the binary source, $(\theta_S, \phi_S, \theta_L, \phi_L)$ are angles which identify the source location and the angular momentum of the secondary, as further explained in the next section. The number of intrinsic parameters is then $D \simeq 10$[1]. For $D \simeq 10$ and $\rho = 30$, which is a conservative SNR value for EMRIs detection [35, 59], we can reasonably and indicatively consider $\Delta\Psi_{thr} = 0.1$ rad.

The dephasing represents a preliminary assessment of the detectability of the scalar charge. A more quantitative analysis is provided by the *faithfulness* among GW signals, a quantity indicating how much two signals differ, as discussed in Section 6.3.2. Finally, in order to determine the actual constraints on the scalar charge, a more sophisticated study is required, based on the Fisher matrix approach. Such study is presented in Chapter 8.

Having fixed a certain time of observation $T_{\rm obs}$, we define the accumulated dephasing between inspirals with and without the scalar charge as

$$\Delta\Psi_\phi = 2\int_0^{T_{\rm obs}} \Delta\Omega_\phi \mathrm{d}t \ , \tag{6.6}$$

where

$$\Delta\Omega_\phi = \omega_{\rm p}^{d} - \omega_{\rm p}^{d=0}. \tag{6.7}$$

Hence, for a fixed binary configuration, we compared the EMRI evolution obtained with and without the scalar charge. A single inspiral is built by fixing

- the binary parameters $(M, m_p, a/M, d)$;
- the initial position of the secondary (r_0, ϕ_0);
- the time of observation $T_{\rm obs}$.

For each inspiral, we fixed $\phi_0 = 0$ and r_0 such that the secondary object reaches the plunge after $T_{\rm obs}$, where we defined the position of the plunge as

$$r_{\rm plunge} = r_{\rm ISCO} + \delta r \ , \tag{6.8}$$

and we adopted the conservative choice of $\delta r = 0.1M$, which is more conservative than the transition region between the inspiral and the plunge as described elsewhere [132, 133].

To model the EMRI evolution, we wrote a `Mathematica` notebook which integrates the equations Eqs (6.4).

6.2.1 Results

The results are summarized in the four density plot of Fig. 6.3, where the white dashed line indicates the threshold of phase resolution of 0.1 rad.

In the top two panels the dephasing is shown for different values of the scalar charge and of the observation time before the plunge, $(d, T_{\rm obs}) = (0.01, 6 \text{ months})$ and $(d, T_{\rm obs}) = (0.005, 12 \text{ months})$, as a function of the binary component masses. All binaries with $M \lesssim 3 \times 10^6 M_\odot$ lead to a dephasing larger than the detectability threshold of 0.1 radians, with the values of the dephasing $\Delta\Psi_\phi$ being almost

[1]The "$\simeq$" sign is due to the presence or the absence of the scalar charge. Moreover, by considering equatorial eccentric inspirals the initial eccentricity is also added to the set of parameters.

insensitive to the mass of the secondary. In both cases, with further six months of observation time (i.e., $T_{\rm obs} = 6$ months for $d = 0.01$ and $T_{\rm obs} = 12$ months for $d = 0.005$) all the binary configurations up to $M \simeq 10^7\, M_\odot$ and $m_p \simeq 100\, M_\odot$ are above the threshold.

In the left bottom panel we study how the dephasing changes as a function of the scalar charge and of the mass of the primary, for $m_p = 10 M_\odot$, $T_{\rm obs} = 12$ months and $a/M = 0.9$. The plot shows that the accumulated phase difference can be significant, especially for binaries with a massive BH of $M \lesssim 10^6 M_\odot$ for which $\Delta\Psi_\phi$ can be larger than 10^3 radians.

Finally, the last (right bottom) panel of Figure 6.3 shows how $\Delta\Psi_\phi$ changes by varying the spin of the primary and the scalar charge of the secondary. The masses of the binary are $(M, m_p) = (10^6, 10) M_\odot$ and the time of observation is $T_{\rm obs} = 12$ months. For a fixed scalar charge, the dephasing increases with the increasing of the primary spin. For $a/M = 0.1(0.9)$, $\Delta\Psi_\phi$ is larger then the threshold of 0.1 radians for $d \gtrsim 0.0033(0.0023)$, respectively. This result is consistent with those of Ref. [134], where the increase of the dephasing with the spin of the primary was discussed.

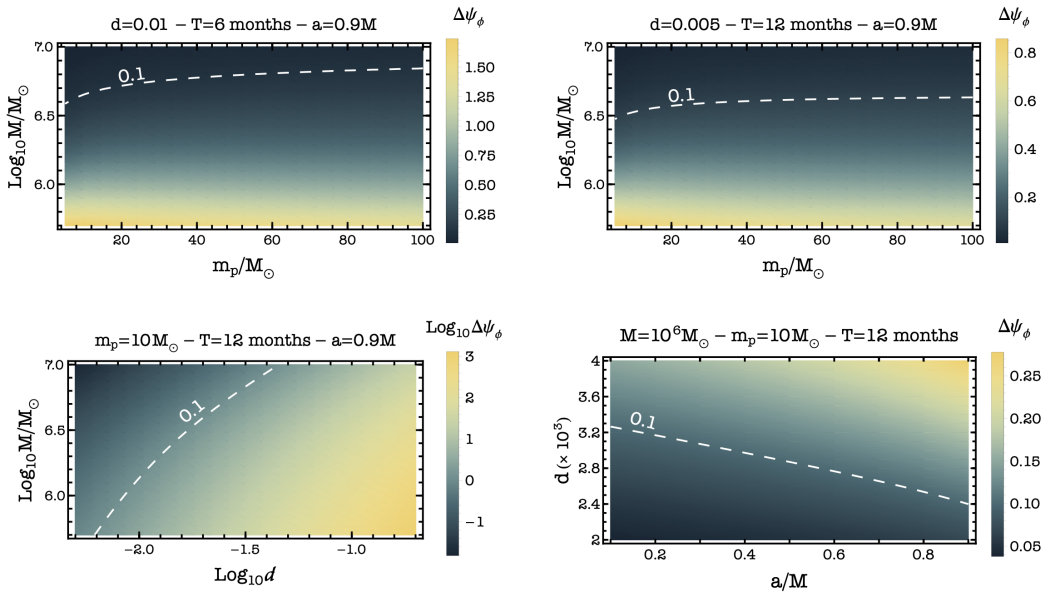

Figure 6.3. Quadrupolar gravitational wave dephasing $\Delta\Psi_\phi$, i.e difference in the GW phase evolution of EMRIs with and without scalar charge. First and second panels show $\Delta\Psi_\phi$ as a function of the binary component masses and refer to EMRIs with $(d, T_{\rm obs}) = (0.01, 6$ months$)$ and $(d, T_{\rm obs}) = (0.005, 12$ months$)$, respectively, for $a/M = 0.9$. Third and fourth panels show the dephasing as a function of (M, d) and of $(d, a/M)$, respectively, for $T_{\rm obs} = 12$ months of observation and $m_{\rm p} = 10 M_\odot$. The dashed white line in each plot identifies the detectability threshold of 0.1 radian for a GW event with SNR of 30 observed by LISA.

6.3 Gravitational wave signals

From the EMRIs evolution it is possible to build the GW signals.

In the linear perturbation theory approach, the GW model is given by the fully relativistic Teukolsky waveforms [68–71]. However, such waveforms result to be computationally expensive. Other several templates have been implemented for

the EMRI modeling, which result in easier computations and can be generated quickly, but which still capture the main features of true waveforms. Among these models there are the Analytical Kludge (AK) [135], which refers to the quadrupolar approximation and is built considering a Post-Newtonian (PN) inspiral, the Numerical Kludge (NK), which builds the trajectory numerically and also consider higher multipoles then the quadrupole [136], and Augmented Analytical Kludges (AAK) [137, 138]. Recently, a collection of tools named Fast EMRI Waveforms (FEW) [139, 140] have been implemented to build EMRI GW signals combining the speed of the kludge models with the accuracy of self-force models [41–43]. For now, FEW is available for fully-relativistic EMRI waveforms for eccentric inspiral around Schwarzschild black holes and improved AAK for generic Kerr inspirals.

Here we adopt the Analytic Kludge, shown below, adapting the template to the fully-relativistic inspirals. Finally, in Section 6.3.2 we compute the faithfulness among GW signals with and without the scalar charge carried by the secondary and we show the obtained results.

6.3.1 The analytic template

We refer to the analytic template presented in [135], which builds GW signals within the quadrupolar approximation and in which the evolution between geodesics is driven by PN formulas. Here, we improve such template by adapting it to our fully-relativistic EMRI inspirals.

In the transverse-traceless gauge, the metric perturbation $h_{ij}^{\rm TT}$ far from the source is given by

$$h_{ij}^{\rm TT} = \frac{2}{d_L}\left(P_{il}P_{jm} - \frac{1}{2}P_{ij}P_{lm}\right)\ddot{I}_{lm} \ , \tag{6.9}$$

where d_L is the source luminosity distance, $P_{ij} = \delta_{ij} - n_i n_j$ is the projection operator onto the wave unit direction n_j, where δ_{ij} is the Kronecker delta. The second time derivative of the mass quadrupole moment $\ddot{I}_{ij}$, is given in terms of the source stress-energy tensor

$$I_{ij} = \int d^3x T^{tt}(t, x^i)x^i x^j = m_p z^i(t) z^j(t) \ , \tag{6.10}$$

where $T^{tt}(t, x^i) = m_p \delta^{(3)}(x^i - z^i(t))$, x^i are Cartesian spatial coordinates, and $z^i(t)$ is the worldline of the secondary object in these coordinates [136]. The strain $h(t)$ produced by the GW and measured by the detector is obtained by combining the plus and cross polarisation and the detector pattern functions. For LISA, a detector of three arms composing an equilateral triangle, the strain is given by [141]

$$h(t) = \frac{\sqrt{3}}{2}\left[h_+(t)F_+(t) + h_\times(t)F_\times(t)\right] \ , \tag{6.11}$$

where the factor $\sqrt{3}/2$ is due to the 60° angle between the arms of the interferometer and

$$h_+ = -\frac{1}{2}\left(\ddot{I}_{11} - \ddot{I}_{22}\right)\left(1 + \cos^2\iota\right) = \mathcal{A}\cos[2\Phi(t) + 2\Phi_0]\left(1 + \cos^2\iota\right) \ , \tag{6.12}$$

$$h_\times = 2\ddot{I}_{12}\cos\iota = -2\mathcal{A}\sin[2\Phi(t) + 2\Phi_0]\cos\iota \ , \tag{6.13}$$

$\mathcal{A} = 2m_p \left[M\omega(t)\right]^{2/3}/d_L$ and ι is the inclination angle between the binary orbital angular momentum and the line of sight. The functions $F_{+,\times}$ are the detector pattern functions. The triangle configuration of LISA can be effectively described as a network of two L-shaped detectors, with the second detector rotated by 45° with respect to the first one, so that the pattern functions $F_{\rm I,II}^{+,\times}$ are given by [141]

$$\begin{aligned} F_{\rm I}^{+} =& \frac{1+\cos^2\theta}{2}\cos 2\phi\cos 2\psi - \cos\theta \sin 2\phi \sin 2\psi \ , \\ F_{\rm I}^{\times} =& \frac{1+\cos^2\theta}{2}\cos 2\phi\sin 2\psi + \cos\theta \sin 2\phi \cos 2\psi \ , \\ F_{\rm II}^{+,\times} =& F_{\rm II}^{+,\times}(\theta, \phi - \pi/4, \psi) \ , \end{aligned} \tag{6.14}$$

where the subscripts I and II refer to the single L-shaped detector.

The angles (θ, ϕ, ψ) are all defined in the detector reference frame, and vary in time due to the LISA motion. The first two describe the location of the binary in the sky, while ψ is the polarization angle. These angles can be expressed in terms of (θ_S, Φ_S) and (θ_L, Φ_L), which identify respectively the source location and the angular momentum $\hat{L}$ of the secondary, both in an ecliptic-based system. The expressions for $(\theta(t), \phi(t))$ are given by [141, 142]:

$$\begin{aligned} \cos\theta(t) =& \frac{1}{2}\cos\theta_S - \frac{\sqrt{3}}{2}\sin\theta_S\cos[\phi_t - \phi_S] \ , \\ \phi(t) =& \alpha_0 + \phi_t + \tan^{-1}\left[\frac{\sqrt{3}\cos\theta_S + \sin\theta_S\cos[\phi_t - \phi_S]}{2\sin\theta_S\sin[\phi_t - \phi_S]}\right] \ , \end{aligned} \tag{6.15}$$

where $\phi_t = \bar{\phi}_0 + 2\pi(t/T)$, $T = 1$ year and $(\bar{\phi}_0, \bar{\alpha}_0)$ specify the orbital and rotational phase of the detector when $t = 0$, and are set to zero. The polarization angle can be expressed as

$$\psi(t) = \tan^{-1}\frac{\hat{L}\cdot\hat{z} - (\hat{L}\cdot\hat{N})(\hat{z}\cdot\hat{N})}{\hat{N}\cdot(\hat{L}\times\hat{z})} \ , \tag{6.16}$$

with $\hat{z}\cdot\hat{N} = \cos\theta_S$ and

$$\hat{L}\cdot\hat{N} = \cos\theta_L\cos\theta_S + \sin\theta_L\sin\theta_S\cos[\phi_L - \phi_S] \ , \tag{6.17}$$

$$\hat{L}\cdot\hat{z} = \frac{1}{2}\cos\theta_{\rm L} - \frac{\sqrt{3}}{2}\sin\theta_L\cos[\phi_t - \phi_L] \ , \tag{6.18}$$

$$\begin{aligned} \hat{N}\cdot(\hat{L}\times\hat{z}) =& \frac{1}{2}\sin\theta_{\rm L}\sin\theta_{\rm S}\sin[\phi_{\rm L} - \phi_{\rm S}] - \frac{\sqrt{3}}{2}\cos\phi_t\left[\cos\theta_{\rm L}\sin\theta_{\rm S}\sin\phi_{\rm S} - \cos\theta_{\rm S}\right. \\ & \left.\sin\theta_{\rm L}\sin\phi_{\rm L}\right] - \frac{\sqrt{3}}{2}\sin\phi_t\left[\cos\theta_{\rm S}\sin\theta_{\rm L}\cos\phi_{\rm L} - \cos\theta_{\rm L}\sin\theta_{\rm S}\cos\phi_{\rm S}\right] \ . \end{aligned} \tag{6.19}$$

Here we choose $(\theta_S, \phi_S, \theta_L, \phi_L) = (\pi/2, \pi/2, \pi/4, \pi/4)$.

Finally, the gravitational wave signal also acquires a modulation due to the LISA orbital motion [136]. We correct for this effect by modifying the phase of the waveform as

$$\Phi(t) \to \Phi(t) + \Phi'(t){\rm R}_{\rm AU}\sin(\theta_S)\cos(2\pi t/T - \phi_s) \ , \tag{6.20}$$

where $\rm R_{AU}$ is the astronomical unit and T = 1 year.

6.3.2 Faithfullness analysis

Given two GW signals h_1 and h_2, we can compute the *faithfulness* $\mathcal{F}[h_1, h_2]$ among them, a quantity that can be used to estimate how much the two signals differ [143–145]. The faithfulness is defined as the noise-weighted inner product of the two signals, normalized with the SNR of the two signals and maximised over time and phase offsets (t_c, ϕ_c) between them, i.e.

$$\mathcal{F}[h_1, h_2] = \max_{\{t_c, \phi_c\}} \frac{\langle h_1 | h_2 \rangle}{\sqrt{\langle h_1 | h_1 \rangle \langle h_2 | h_2 \rangle}} \ , \tag{6.21}$$

with $\langle h_1 | h_2 \rangle$ being the noise-weighted inner product of the two signals in the frequency domain,

$$\langle h_1 | h_2 \rangle = 4\Re \int_{f_{\rm min}}^{f_{\rm max}} \frac{\tilde{h}_1(f) \tilde{h}_2^\star(f)}{S_n(f)} {\rm d}f \ , \tag{6.22}$$

where $\tilde{h}(f)$ indicates the Fourier transform of the signal h and S_n the power spectral density (PSD) of LISA detector. The signal to noise ratio (SNR) of a signal h is defined as $\rho = \sqrt{\langle h | h \rangle}$. The minimum integration frequency is set to $f_{\rm min} = 10^{-4}$Hz, while $f_{\rm max} = f_{\rm Ny}$, with $f_{\rm Ny}$ being the Nyquist frequency.

Two signals result to be distinguishable by LISA if $\mathcal{F} \lesssim \mathcal{F}_{\rm thr}$, which means that the two waveforms are significantly different and don't provide a faithful description of one another. The value of $\mathcal{F}_{\rm thr}$ is given by [145]

$$\mathcal{F}_{\rm thr} = 1 - \frac{D-1}{2\rho^2}, \tag{6.23}$$

where D is the number of parameters. We computed the faithfulness between templates with and without the scalar charge, so that, for a circular inspiral, $D \simeq 10$ and, by assuming an SNR $\rho = 30$, the two signals result to be distinguishable by LISA if $\mathcal{F} \lesssim 0.988$.

The LISA power spectral density

The noise spectral density for LISA is obtained from Cornish & Robson [146], who provide an accurate analytic fit for the detector noise. The PSD consists of two parts: the instrumental and the confusion noise produced by unresolved galactic binaries, i.e.

$$S_n(f) = S_n^{\rm Ins}(f) + S_n^{\rm WDN}(f) \ . \tag{6.24}$$

where

$$S_n^{\rm Ins}(f) = A_1 \left(P_{\rm OMS} + 2[1 + \cos^2(f/f_\star)] \frac{P_{\rm acc}}{(2\pi f)^4} \right) \left(1 + \frac{6}{10} \frac{f^2}{f_\star^2} \right) \ ,$$

$A_1 = \frac{10}{3L^2}$, $L = 2.5$Gm, $f_\star = 19.09$mHz, while

$$P_{\rm OMS} = (1.5 \times 10^{-11} {\rm m}^2 \left[1 + \left(\frac{2{\rm mHz}}{f} \right)^4 \right] \ {\rm Hz}^{-1} \ ,$$

$$P_{\rm ACC} = (3 \times 10^{-15} {\rm ms}^{-2})^2 \left[1 + \left(\frac{0.4{\rm mHz}}{f} \right)^2 \right] \times \left[1 + \left(\frac{f}{8{\rm mHz}} \right)^4 \right] \ {\rm Hz}^{-1} \ .$$

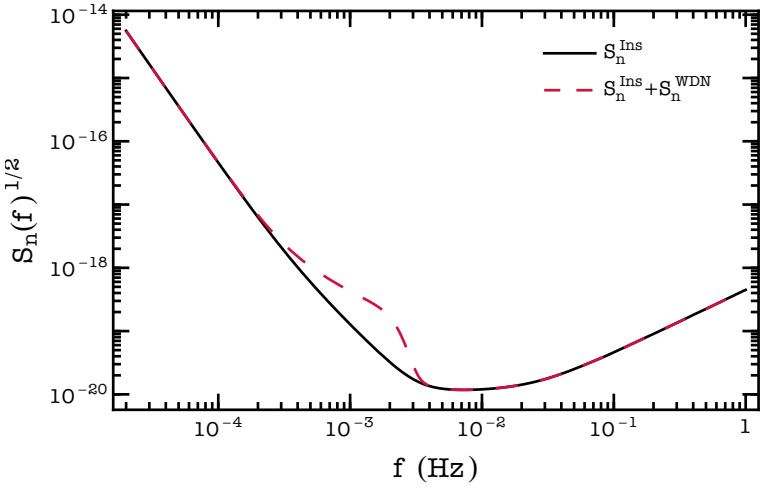

Figure 6.4. Noise spectral density for LISA as a function of the frequency, with and without the confusion noise produced by unresolved galactic white dwarf binaries (WDN).

For the white dwarf contribution

$$S_n^{\rm WDN} = A_2 f^{-7/3} e^{-f^\alpha + \beta f \sin(\kappa f)} [1 + \tanh(\gamma(f_k - f))] \ {\rm Hz}^{-1} \ ,$$

with the amplitude $A_2 = 9 \times 10^{-45}$, and the coefficients $(\alpha, \beta, \kappa, \gamma, f_k) = (0.171, 292, 1020, 1680, 0.00215)$. The analytic fit is plotted in Fig. 6.4 as a function of frequency.

6.3.3 Results

The results of the faithfulness analysis are reported in Fig. 6.5, which shows the faithfulness $\mathcal{F}$ between the plus polarization of two GW signals emitted by binaries with and without the charge, as a function of the scalar charge. Two different time of observation, 6 and 12 months, are considered. The horizontal continuous line in the figure represents the threshold value beyond which the two signals can be distinguished, $F_{\rm thr} = 0.988$ for $\rho = 30$. For 12 months of observation, the faithfulness is below the threshold set by $\rho = 30$ for $d \gtrsim 0.01$, while, by reducing $T_{\rm obs}$ to 6 months, two signals with $\rho = 30$ result distinguishable by LISA for $d \gtrsim 0.05$.

The analysis carried out so far highlights two important aspects: (i) the scalar charge provides a significant shift in the phase of the GW signal emitted by EMRIs, (ii) the dephasing induces a mismatch in the template with respect to the zero-charge case, which can potentially lead to a severe loss of events and to a bias in the estimation of the waveform parameters [144]. This suggests that one year of LISA observations of EMRIs may be able to reveal the presence of a scalar charge as small as $d \sim 0.05 - 0.01$.

Given these very promising results, we improved the EMRI model by considering equatorial eccentric inspirals, making it closer to real astrophysical scenarios (next chapter) and we performed a parameter estimation over the binary system by making use of the Fisher Information Matrix analysis (Chapter 8).

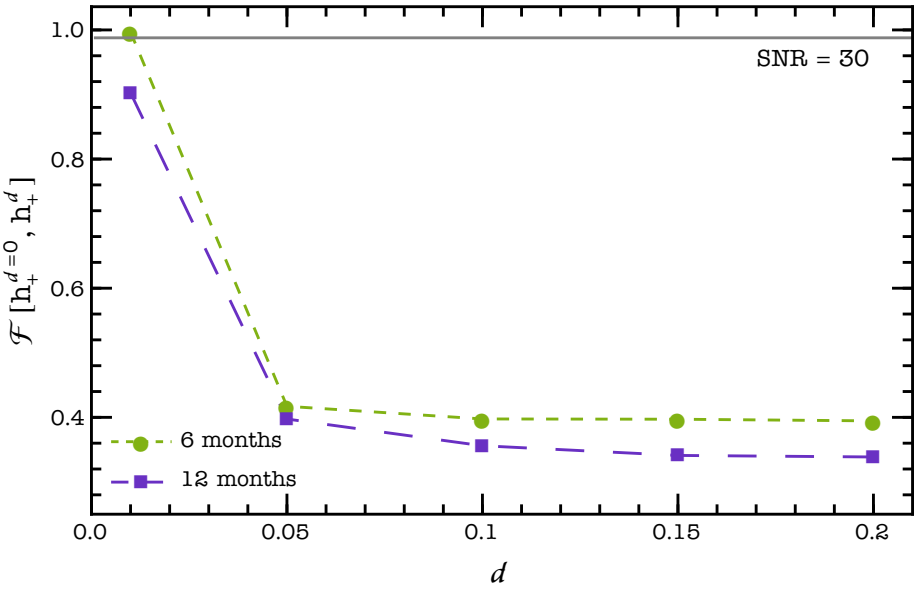

Figure 6.5. Faithfulness between the GW plus polarization computed with and without the scalar charge, with $d = 0$ and $d \neq 0$, as a function of the latter and for different signal durations. The signal duration is measured in months (6 or 12) before the plunge. The horizontal line identifies the threshold of distinguishability, $\mathcal{F} \lesssim 0.988$, set up by SNR of 30.

Chapter 7

EMRIs with massless scalar fields: Eccentric equatorial orbits

This chapter presents the study of the EMRI evolution considering equatorial eccentric adiabatic inspirals. The analysis is analogous to that one presented in Chapter 6 for circular orbits. In Section 7.1 we present the energy and angular momentum emission which drives the adiabatic orbital evolution, which is presented in the next section. Finally, in Section 7.3 we build the EMRI template and compute the faithfulness among the signals.

7.1 Energy and angular momentum emission

The energy and angular momentum fluxes for equatorial eccentric orbits are computed from Eqs. (5.91) - (5.93) by building a `Mathematica` code for both the gravitational and scalar emission. The expression for the total emission is given in (5.97):

$$\dot{C}_{\rm GW} = \sum_{i=+,-} [\dot{C}^{(i)}_{\rm grav} + \dot{C}^{(i)}_{\rm scal}] \ = \dot{C}_{\rm grav} + \dot{C}_{\rm scal} \ ,$$

where $C \in [E, L]$, $\dot{C}_{\rm grav} \equiv \dot{C}^{(+)}_{\rm grav} + \dot{C}^{(-)}_{\rm grav}$, $\dot{C}_{\rm scal} \equiv \dot{C}^{(+)}_{\rm scal} + \dot{C}^{(-)}_{\rm scal}$ and $\dot{C}_{\rm scal} = d^2\bar{\dot{C}}_{\rm scal}$.

7.1.1 Numerical implementation

For the fluxes computation, we have exploited some of the numerical routines implemented in the Black Hole Perturbation Toolkit (BHPT) [120], and in particular the Teukolsky package to calculate the homogeneous solutions of the Teukolsky equation. At the time of our study, the BHPT was implemented to obtain fluxes for circular orbits only, so that we built an independent `Mathematica` code for the integration over the source terms for the eccentricity-dependent perturbations and the corresponding fluxes. We have checked that for $e = 0$ our code reproduces the fluxes obtained by the BHPT with great accuracy. Comparisons with previous results for eccentric EMRIs in GR are discussed in Appendix A. We also used the KerrGeodesics package of the BHPT for the orbital frequencies computation.

We have computed $\left(\dot{E}^{(\pm)}, \dot{L}^{(\pm)}\right)$ for different values of (e, p) and assuming $a = 0.2M$ and $a = 0.9M$ for the primary spin. Note that it is plausible that MBHs

falling in the LISA band will be rapidly spinning, with $a \sim 0.9M$ or possibly even larger [35]. We have sampled the eccentricity between $0.1 \leq e \leq 0.5$ in steps of $\Delta e = 0.1$. These choices lead to an eccentricity at the plunge in agreement with standard expectation, a flat distribution in $e \in [0, 0.2]$ [35]. To make the grid in p denser close to the separatrix, where orbital parameters vary more rapidly, for the semi-latus we have taken 41 points uniformly spaced in the new variable $u = (p - 0.9p_s)^{-1/2}$, within $[u(p_{\rm min}), u(p_{\rm max})]$, where $p_{\rm max} = p_{\rm min} + 10M$ and $p_{\rm min} = p_s + 0.03M$, with p_s being the value of p at the separatrix as a function of e (see Eq. (3.41)). Then, from the inverse relation $p(u)$, we have obtained a non-uniform grid for the semi-latus rectum. In this way, if one considers the grid in $(e, p - p_s)$, the initial and the final values of $p - p_s$ are the same for each values of the eccentricity, i.e. $0.03M$ and $10.03M$, respectively. This is optimal for a two dimensional interpolation with `Mathematica`, which can be performed only on a structured grid.

For each point in the (e, p) plane we have computed the total flux by summing over the three indexes (ℓ, m, n) [1]:

$$\dot{C} = \sum_{\ell m n} \dot{C}_{\ell m n} = \sum_{\ell_{\rm min}}^{\ell_{\rm max}} \sum_{m=-\ell}^{m=+\ell} \left(\dot{C}_{\ell m 0} + 2 \sum_{n=1}^{n_{\rm max}} \dot{C}_{\ell m n} \right) , \tag{7.1}$$

where $C \in [E, L]$ and the $\ell = 0, 1$ components are due to the scalar flux only, while both scalar and gravitational fluxes contribute to the $\ell \geq 2$ components. The factor 2 in Eq. (7.1) accounts for a symmetry in the fluxes, for which the flux with $(l, -m, -n)$ is the same as the flux with (l, m, n), see Eqs. (5.38) and (5.88).

In our code we have chosen $\ell_{\rm max} = (8, 10)$ respectively for $s = (0, -2)$. These values are such that, for a primary spin of $a = 0.9M$ and eccentricity $e = 0.5$, the relative difference in the flux between $\ell_{\rm max}$ and $\ell_{\rm max} - 1$ is less than 2% for the innermost p of the grid, while for the outermost is less than 0.01%. For $e = 0.1$ the relative difference is less than 1% for the innermost p and less than 0.001% for the outermost.

The value for $n_{\rm max}$ is chosen such that the fractional change in the sum (7.1) is smaller than 10^{-4} for three consecutive values of n. This choice is motivated by the behavior of the energy flux spectrum as a function of (e, n). Indeed, we observe that for low eccentricities the flux has a peak at small values of n, rapidly decreasing afterwards. On the other hand, for larger values of e the spectrum shows relative maxima before reaching the absolute peak, located at higher n compared to the low-eccentricity case. This behaviour is shown in Fig. 7.1 where we plot $\dot{E}^{(+)}_{\ell m n}$ as a function of n for different values of the eccentricity and for the $\ell = m = 2$ (top raw) and $\ell = m = 5$ (bottom raw) modes. The flux at the horizon and the gravitational fluxes show the same qualitative behaviour.

After computing the fluxes for each point of the grid, we have performed an interpolation using a built-in `Mathematica` function over the grid in the two parameters $(e, p - p_s)$. In order to estimate the errors introduced by the interpolation, we computed also the fluxes in points outside the grid, and estimated the relative difference between the interpolated and the computed fluxes. The relative difference between them turns out to be $\lesssim 0.2\%$ for points fluxes closer to the separatrix and it grows for larger values of p, up to $\sim 6 - 7\%$ for the furthermost points. Numerical values for the fluxes obtained for different points outside our grid are listed in Tables

[1] We remind that the index n is associated to the radial motion, with period T_r, see Chapter 3.

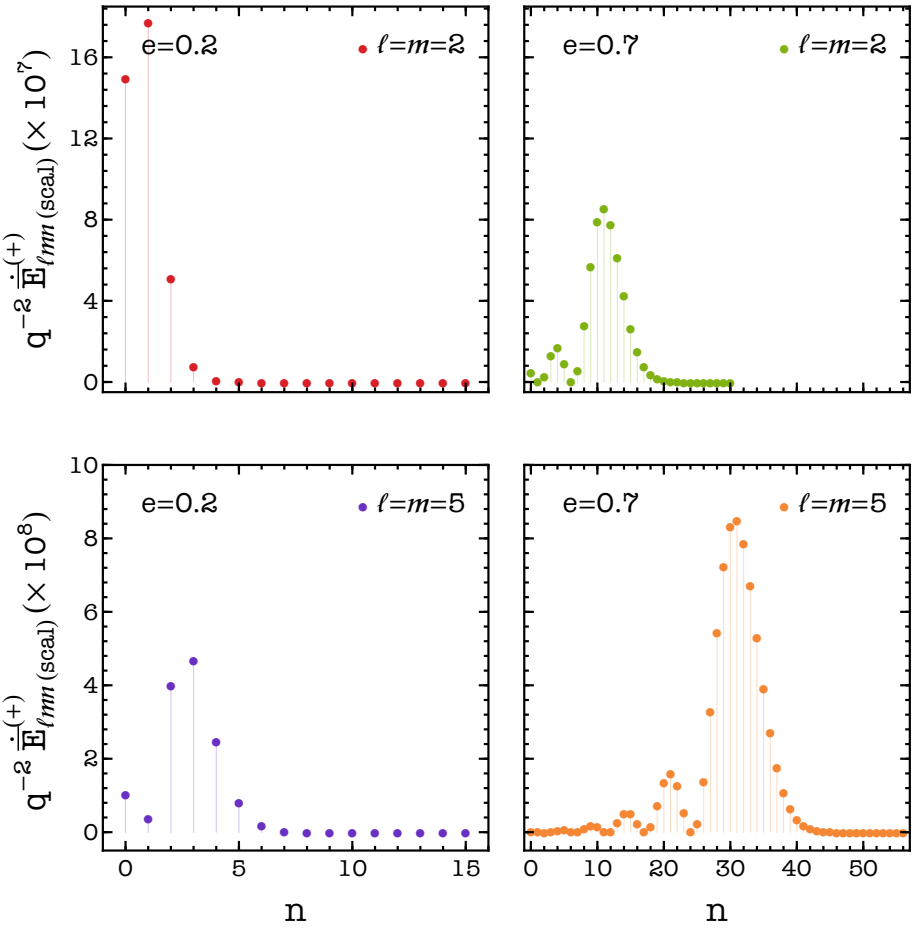

Figure 7.1. Harmonic components of the scalar energy flux at infinity as a function of n, for orbital configurations with $p/M = 7$, $e = 0.2$ (left column) and $e = 0.7$ (right column). Top and bottom panels show the $\ell = m = 2$ and $\ell = m = 5$ components of the flux, respectively. The MBH spin is $a/M = 0.9$.

.

A.1 and A.2 of Appendix A.

7.1.2 Results

The results of the total energy and angular momentum fluxes are summarized in Fig. 7.3, which shows the behaviour of the ratio between the scalar and gravitational emission for the energy (top raw) and angular momentum (bottom raw) fluxes, as a function of the semilatus rectum p/M. The left column shows the fluxes relative to a primary spin $a/M = 0.2$, while the right column to $a/M = 0.9$. The inset in each panel provides the absolute value of $\dot{E}_{\rm scal}$ and $\dot{L}_{\rm scal}$.

As was the case for circular orbits discussed in the previous chapter, for a given value of the eccentricity the ratio between the scalar and the gravitational components decreases for smaller p, due to the faster growth of $\dot{E}_{\rm grav}$ and $\dot{L}_{\rm grav}$. This behavior is also confirmed by the analyses of the harmonic components shown in Fig. 7.2 for $e \neq 0$. Moreover, for fixed p, while the absolute value of $\dot{E}_{\rm scal}$ grows with the eccentricity, the relative difference with respect to the gravitational flux becomes smaller. Note that the value of the separatrix increases for higher eccentricity. However, the periastron of the last stable orbit decreases for higher eccentricity, so that a more eccentric orbit can lead the particle closer to the MBH horizon.

As shown in Fig. 7.2, for large orbital separation, the dipole $\ell = m = 1$ scalar mode approaches the quadrupolar $\ell = m = 2$ (scalar) component, with the latter increasing steeply for smaller separations. The monopole component $\ell = m = 0$ is excited only for eccentric orbits and shows a similar steep increase, although it remains subdominant and starts decreasing before the plunge.

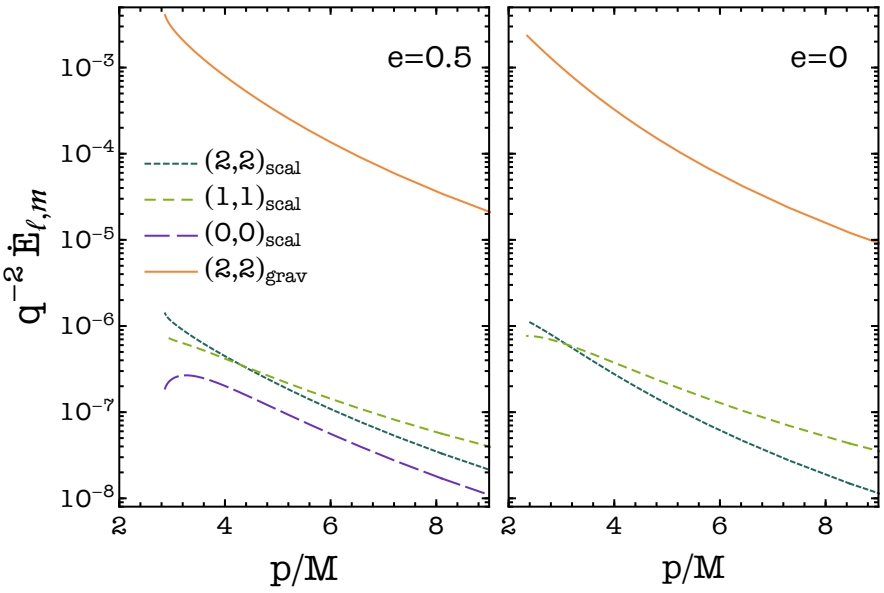

Figure 7.2. Harmonic components of the gravitational and scalar energy flux, normalized with the mass-ratio, with $d = 0.1$ as a function of the semi-latus rectum, for eccentric (left panel) and circular (right panel) orbits. The MBH's spin is $a/M = 0.9$. We only show the dominant modes, i.e. the $\ell = (0, 1, 2)$ coefficients and, for the eccentric orbit, we sum over the index n. In the gravitational sector only $\ell \geq 2$ modes are present, while in the scalar sector the dipole contribution is excited. The monopole contribution of the scalar sector is only excited in the eccentric case.

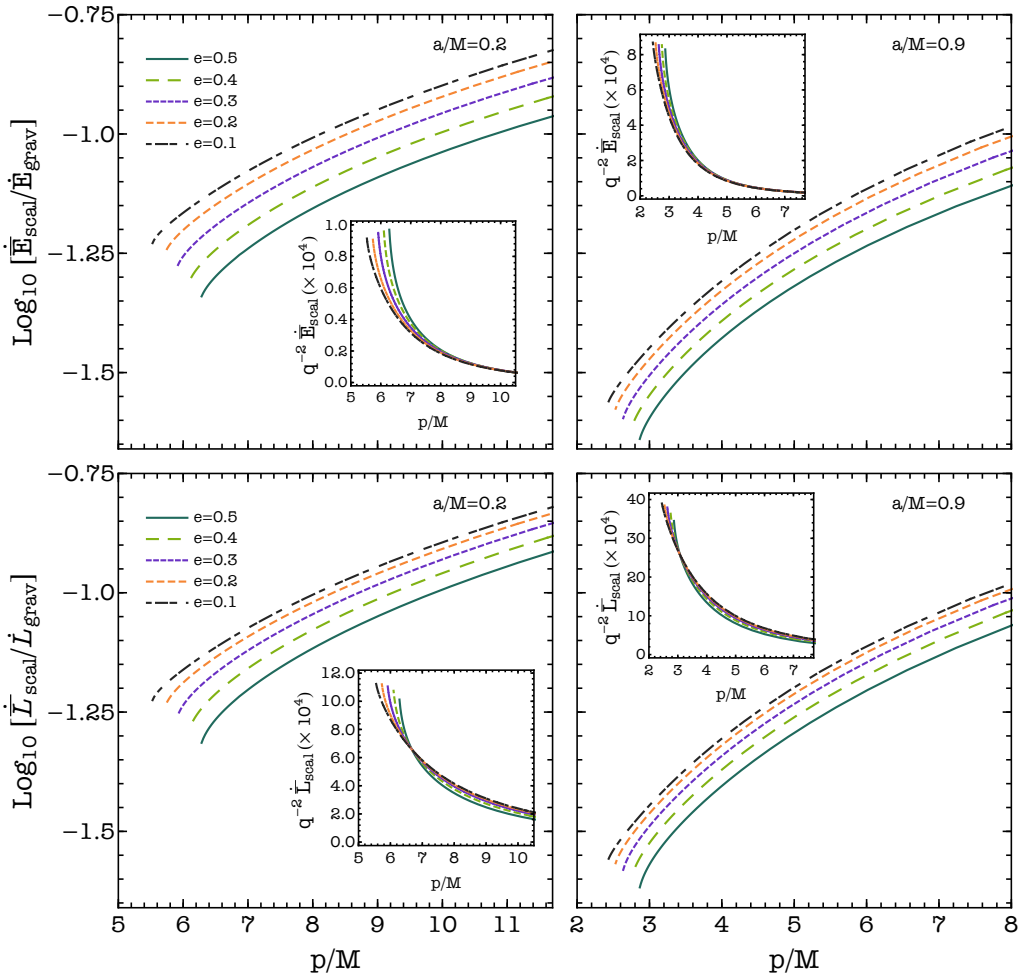

Figure 7.3. Ratio between the scalar and gravitational energy (top panels) and angular momentum (bottom panels) fluxes as a function of the semi-latus rectum p, for different values of the eccentricity and a fixed spin of $a = 0.2M$ (left panels) and $a = 0.9M$ (right panels). The inset within each plot shows the absolute value of the scalar component, normalized with the mass ratio. We assume $d = 1$ for all the configurations.

7.2 Orbital evolution

Having computed the fluxes, we proceeded by building the binary evolution. The The adiabatic orbital evolution is built by imposing the balance law

$$\dot{C} = -\dot{C}_{\rm GW} \ , \tag{7.2}$$

with $C = (E, L)$. The rate of change in time of the integrals of motion (E, L) is related to the rate of change of of change of the eccentricity and of the semi-latus rectum (e, p) by [70]

$$\dot{E} = E_{,p}\dot{p} + E_{,e}\dot{e} \quad , \quad \dot{L} = L_{,p}\dot{p} + L_{,e}\dot{e} \ , \tag{7.3}$$

so that

$$\dot{p} = (L_{,e}\dot{E} - E_{,e}\dot{L})/H \quad , \quad \dot{e} = (E_{,p}\dot{L} - L_{,p}\dot{E})/H \ , \tag{7.4}$$

with $H = E_{,p}L_{,e} - E_{,e}L_{,p}$.

To solve the differential equations we built a `Mathematica` code, obtaining the time evolution of (e, p) and that on of the orbital frequencies related to each geodesics, $\Omega_i(e(t), p(t))$, with $i = \phi, r$. We then define the phases associated to each frequencies,

$$\Psi_i = \int_0^{T_{\rm obs}} \Omega_i dt \quad (i = \phi, r) \, , \tag{7.5}$$

and the quadrupolar dephasing obtained by comparing evolutions with and without the scalar charge:

$$\Delta\Psi_i = 2\int_0^{T_{\rm obs}} \Delta\Omega_i {\rm d}t \qquad i = \phi, r \ , \tag{7.6}$$

where

$$\Delta\Omega_i = \Omega_i^d - \Omega_i^{d=0}. \tag{7.7}$$

A single inspiral is built by fixing

- the binary parameters $(M, m_p, a/M, d)$;
- the initial position of the secondary $(p_0, e_0, \Psi_\phi^{\rm in}, \Psi_r^{\rm in})$;
- the time of observation $T_{\rm obs}$.

For each inspiral considered, we fixed $\Psi_i^{\rm in} = 0$ with $i = \phi, r$, the apastron to $r_a = 11M$ and we considered different choices of the initial periastron r_p. The initial semi-latus rectum and eccentricity (p_0, e_0) are then obtained by the initial apastron and periastron. Each inspiral is then evolved until the plunge, where we defined the position of the plunge as

$$\begin{aligned} &p_{\rm fin} = p_{\rm min}(e_{\rm fin}) \ , \ \text{where} \\ &p_{\rm min}(e_{\rm fin}) = p_{\rm s}(e_{\rm fin}) + 0.11M \end{aligned} \tag{7.8}$$

and $p_{\rm s}$ is the semi-latus rectum of the separatrix.

7.2.1 Results

The results of the accumulated dephasing are shown in Fig. 7.4. In the top panel, the qudrupolar dephasing corrisponding to the Ψ_ϕ phase is plotted as a function of the time of observation for several inspirals with the same initial apastron $r_a = 11M$ and different choices of the periastron r_p, up to the plunge. The scalar charge has been fixed to $d = 0.01$. The initial and final values of the periastron and eccentricity of each inspiral with $d = 0.01$ are provided in Table 7.1. The bottom panel is analogous to the upper one, but for the Ψ_r phase.

We observe that, by increasing the initial periastron, i.e. by reducing the initial eccentricity, the time it takes for the secondary to reach the plunge grows, leading to larger values of the accumulated dephasing. However, for a given time of observation, $\Delta\Psi_\phi$ is larger for inspirals with higher e_{in}.

In order to assess the detectability by LISA, we plot the $\Delta\Psi_\phi = 0.1\,\text{rad}$ threshold, corresponding to the minimum phase potentially resolvable by the detector for a binary observed with a SNR of 30 (note that $\Delta\Psi_r \ll \Delta\Psi_\phi$ and thus gives a negligible contribution to the dephasing), see Eq. (6.5).

After 4-6 months of observation all the considered inspirals lead to a dephasing larger then the threshold. Values of the scalar charge > 0.01 will also lead to larger dephasing. We provide some reference values of the latter after 12 months of evolution for different choices of d in Table 7.1. The steep variation in $\Delta\Psi_r$ at the end of the evolution appears to be due the orbital eccentricity, whose time derivative changes signs close to the plunge. That eccentricity grows as one approaches the plunge has already been pointed out in the literature, see *e.g.* [70]. While $e(t)$ increases, the change of Ψ_r (defined in Eq. (7.5)) for $d \neq 0$ becomes smaller then the one for $d = 0$, $\Delta\Psi_r$ acquires a negative sign and ends up counterbalancing the dephasing accumulated until the turning-point.

While after several months of observation the difference in the phase evolution between inspirals computed both with and without the scalar field's influence leads to accumulated dephasings larger then the LISA threshold, the EMRI trajectories in the (p, e) plane relative to such inspirals do not show significant differences, for the small values of d considered in our work. A more quantitative analysis on the scalar charge detectability is provided in the next section, in which an estimate of the mismatch among GW templates computed with and without the scalar charge is provided.

r_p^{in}/M	e_{in}	r_p^{fin}/M	e_{fin}
3.667	0.49997	2.18606	0.18945
4	0.47	2.19251	0.18185
5.5	0.33	2.19721	0.17846
7	0.22	2.19756	0.17812
7.5	0.19	2.19759	0.17809
7.9	0.16	2.19761	0.17807
11	0	2.789	0

Table 7.1. Values of the initial and final periastron and eccentricity for the inspirals of Fig. 7.4

$e_{\rm in}$	d	$\Delta\Psi_\phi$	$\Delta\Psi_r$
0.22	0.01	0.88	0.5
	0.05	21	12
	0.1	88	48
0.33	0.01	4	1.5
	0.05	105	38
	0.1	423	151

Table 7.2. Values of the accumulated dephasings after 12 months of evolution for three different values of the scalar charge $d = (0.01, 0.05, 0.1)$, for a primary spin $a/M = 0.9$. The initial apastron is fixed to $r_a = 11M$, as for the plots in Fig. 7.4.

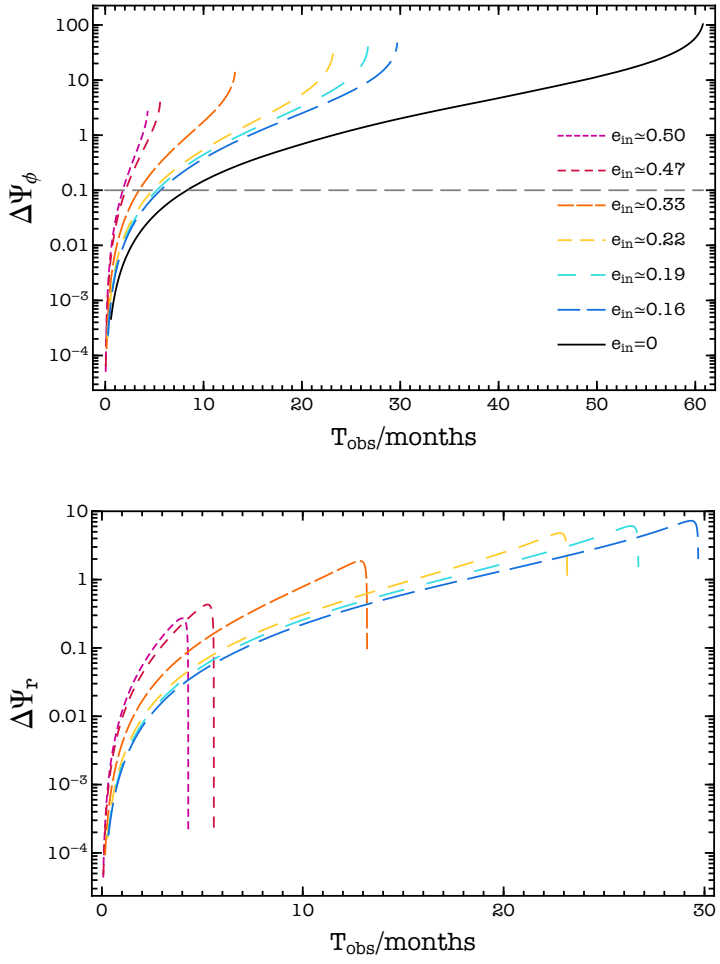

Figure 7.4. Azimuthal (top) and radial (bottom) quadrupolar dephasing as a function of the observation time, assuming spin $a = 0.9M$. The curves refer to inspirals with initial apastron $r_a = 11M$ and different values of the initial periastron, which correspond to initial eccentricities within $e \simeq [0, 0.5]$. We fix the scalar charge to $d = 0.01$. The horizontal line in the top panel identifies the threshold for phase resolution by LISA for a binary observed with signal to SNR of 30 [131]. Although this is not visible in the semi-logarithmic scale, the first two curves in the bottom panel reach negative values.

7.3 Gravitational waves templates

As done for the circular inspiral, we build the gravitational wave template by adapting the analytical kludge of [135], which is based on the quadrupolar waveforms derived by Peters and Mathews [147] and include the effects of pericenter precession, Lense-Thirring precession, and inspiral from radiation reaction computed with Post Newtonian formulae, to the fully-relativistic equatorial eccentric evolution. Then, we compute the faithfulness among signals produced by EMRIs with and without the scalar charge.

7.3.1 The analytic template

The strain amplitude for LISA can be written as a sum of harmonics

$$h_\alpha(t) = \sum_n h_{\alpha,n}(t) \quad , \quad \alpha = (\mathrm{I}, \mathrm{II}), \tag{7.9}$$

where the index α runs on the two independent LISA detectors, as explained in the previous chapter, an the n-th harmonic can be written as

$$h_{\alpha,n}(t) = \frac{\sqrt{3}}{2}\left[F^+_\alpha(t)A^+_n(t) + F^\times_\alpha(t)A^\times_n(t)\right] \ , \tag{7.10}$$

where $F^{+,\times}_\alpha$ are the LISA pattern function, given in Eqs. (6.14) of Chapter 6, and $A^{+,\times}_n$ are the amplitudes, relative to the plus (+) and cross (×) polarization, whose expressions are given by

$$A^+_n = -[1 + (\hat{L}\cdot\hat{N})^2][a_n\cos(2\gamma) - b_n\sin(2\gamma)] + [1 - (\hat{L}\cdot\hat{N})^2]c_n \ , \tag{7.11}$$

$$A^\times_n = 2(\hat{L}\cdot\hat{N})[b_n\cos(2\gamma) + a_n\sin(2\gamma)] \ . \tag{7.12}$$

The angle $\gamma(t)$ measures the direction of pericenter with respect to $\hat{x} = [-\hat{N} + \hat{L}(\hat{L}\cdot\hat{N})]/[1 - (\hat{L}\cdot\hat{N})^2]^{1/2}$. In our case, in which we consider only equatorial orbits, we relate γ to Ψ_r by $\cos(\gamma) = \cos(\gamma_0)\cos(\Psi_r)$, where γ_0 measures the direction of the initial position of the pericenter with respect to $\hat{x}$, and Ψ_r is the angle in the orbital plane defined in (7.5). We chose $\gamma_0 = \pi/4$. Peters and Mathews [147] showed that the coefficients (a_n, b_n, c_n) are given by

$$\begin{aligned} a_n = &-n\mathcal{A}\big[J_{n-2}(ne) - 2eJ_{n-1}(ne) + (2/n)J_n(ne) + 2eJ_{n+1}(ne) \\ &- J_{n+2}(ne)\big]\cos[n\Phi(t)] \ , \end{aligned} \tag{7.13}$$

$$b_n = -n\mathcal{A}(1-e^2)^{1/2}[J_{n-2}(ne) - 2J_n(ne) + J_{n+2}(ne)]\sin[n\Phi(t)] \ , \tag{7.14}$$

$$c_n = 2\mathcal{A}J_n(ne)\cos[n\Phi(t)] \ , \tag{7.15}$$

where J_n is the Bessel function of the first kind, $\mathcal{A} = (2\pi\nu M)^{2/3}\mu/d_L$, with $2\pi\nu = \mathrm{d}\Phi/\mathrm{d}t$ and d_L being the source luminosity distance. In this work we fix $\Phi = \Psi_\phi$, such that $2\pi\nu = \Omega_\phi$.

The waveform templates have been implemented summing over the harmonics with $\ell = 2$ and different values of n:

$$h(t) = \sum_{n=1}^{\bar{n}} h_n(t) \ . \tag{7.16}$$

Each term is a sum over $m = -2, \dots, 2$. We consider contributions up to $\bar{n} = 10$. We have checked that the relative difference between the faithfulness computed with this setup, and including a further component, i.e. with $\bar{n} = 11$ is $\ll 0.1\%$.

The GW signals were computed for EMRIs evolution of 1 year before the plunge, with both in the presence and in the absence of the scalar charge of the secondary. The plunge is defined as in Eqs. (7.8) of the previous section. We then computed the faithfulness between the two plus polarization of the two signals, for different values of the scalar charge, and considering a circular and an equatorial eccentric evolution.

7.3.2 Results

The results are shown in Fig. 7.5, in which the faithfulness is plotted as a function of d. The dark green triangles are relative to eccentric inspirals with $e_{\rm fin} = 0.18$, such that the plunge is located at $(p_{\rm fin}/M, e_{\rm fin}) \simeq (2.59, 0.18)$. In particular, for $d = 0$ the initial position is given by $(p_{\rm in}/M, e_{\rm in}) \simeq (7.071, 0.492)$. The light green dots are relative to the circular ones.

The horizontal red dashed line represent the threshold of detectability for LISA. As explained in Chapter 6, Section 6.3.2, such threshold can be computed as $\mathcal{F}_{\rm thr} = 1 - (D-1)/(2\rho^2)$, with D being the numbers of intrinsic parameters of the binary system and ρ the SNR of the emitted GW signals. For the equatorial eccentric case, $D \simeq 11$, so that, for GW signals with $\rho = 30$, we obtain $\mathcal{F}_{\rm thr} = 0.994$.

For $d \gtrsim 0.01$ the faithfulness for both the circular and the eccentric inspiral is well below the threshold, while for lower values of the scalar charge the faithfulness increases reaching the threshold. Moreover, for eccentric inspirals the latter the distinguishability increases, leading to a smaller mismatch between the the templates.

While more sophisticated analysis is required to determine the actual constraints on d that can be inferred by EMRI on eccentric orbits, the dephasing and faithfulness results provide a strong indication that LISA should be able to constrain or detect even small values of the scalar charge. Moreover, Fig. 7.5 suggests that the inclusion of the eccentricity in the analysis improves the distinguishability of the scalar charge, at least for $d \gtrsim 0.01$.

Our results are consistent with [148], which also performed a Fisher analysis on equatorial eccentric EMRIs.

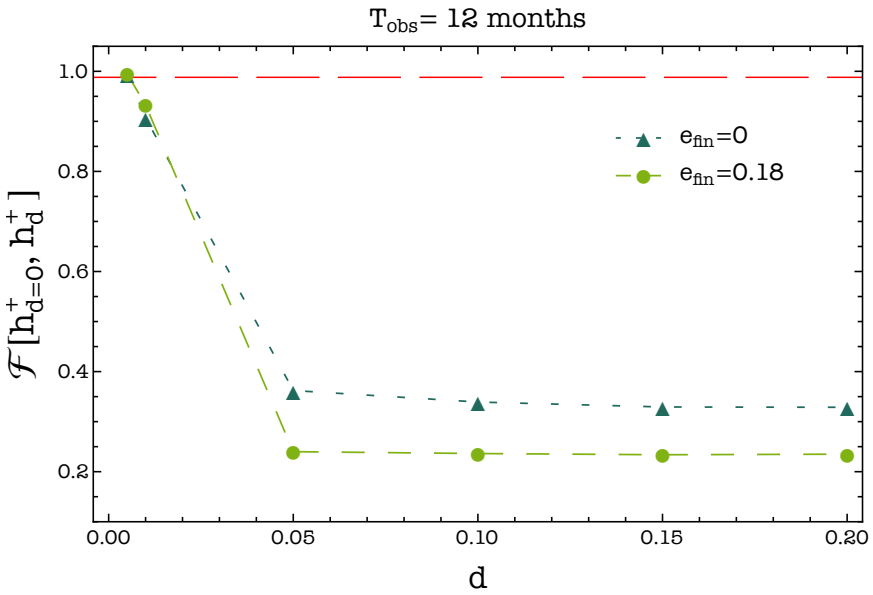

Figure 7.5. Faithfulness between the plus polarization of two GW waveforms computed with $d = 0$ and $d \neq 0$, as a function of the scalar charge, for a circular (dark triangles) and an eccentric (light dots) inspiral. The MBH's spin is $a/M = 0.9$, while the time of observation is fixed to 12 months. The dashed line corresponds to the threshold below which the two templates are distinguished by LISA for a binary observed with SNR of 30 [145].

Chapter 8

Fisher Information Matrix analysis for equatorial circular EMRIs

The Fisher Information Matrix formalism (FIM) is a method of parameter estimation for gravitational waves [149–151]. In this chapter, we present FIM analysis over EMRI prototypes with massless scalar fields in which the secondary performs 1 year of evolution in circular equatorial orbits around a rotating massive black hole, before plunging into it. A parameter estimation with the FIM methods was also performed for massive scalar fields and circular EMRIs. Such results are presented in Chapter 9.

8.1 FIM methods

The EMRI binaries taken into consideration are described by a set of parameters $\vec{\theta} = \{M, m_p, a/M, d_L, \theta_S, \phi_S, \theta_L, \phi_L, r_0, \phi_0, d\}$, where: (M, m_p) are the masses of the primary and secondary object, respectively, (r_0, ϕ_0) are the initial radius and phase, d_L is the luminosity distance of the binary source, $(\theta_S, \phi_S, \theta_L, \phi_L)$ are angles which identify the source location and the angular momentum of the secondary, d is the scalar charge carried by the inspiralling body.

In the limit of large signal-to-noise ratio ρ, the posterior probability distribution of the source parameters, assuming flat or Gaussian priors on $\vec{\theta}$, given a certain observation $o(t)$, can be approximated by a multivariate Gaussian distribution centred around the true values with covariance given by the inverse of the Fisher Information matrix Γ_{ij} [149–151]:

$$\log p(\vec{\theta}|s) \propto \log p_0(\theta) - \frac{1}{2}\Delta_i \Gamma_{ij} \Delta_j \ , \tag{8.1}$$

where p_0 is the parameter's prior distribution, $\Delta^i = \theta^i - \hat{\theta}^i$ is the shift between the measured and the true values $\hat{\theta}_i$, and the Fisher Information Matrix Γ_{ij} is defined as

$$\Gamma_{ij} = \left\langle \frac{\partial h}{\partial \theta_i} \middle| \frac{\partial h}{\partial \theta_j} \right\rangle_{\theta=\hat{\theta}} \ . \tag{8.2}$$

The $\langle ... \rangle$ brackets indicate the inner product, defined in Eq. (6.22), while h is the gravitational wave template.

By defining the inverse of the Fisher matrix $\mathbf{\Sigma} = \mathbf{\Gamma}^{-1}$, the diagonal and off-diagonal components provide the statistical errors on $\vec{\theta}$ and correlation coefficients among parameters, respectively, i.e.:

$$\sigma_i = \Sigma_{ii}^{1/2} \quad , \quad c_{\theta_i\theta_j} = \Sigma_{ij}^{1/2}/(\sigma_{\theta_i}\sigma_{\theta_j}) \ . \tag{8.3}$$

Given the two-interferometer configuration for the LISA detector (see Chapter 6), we can define a total SNR $\rho = \sqrt{\rho_{\rm I}^2 + \rho_{\rm II}^2}$, and a total covariance matrix of the binary parameters obtained by inverting the sum of the Fisher matrices $\sigma_{\theta_i}^2 = (\Gamma_{\rm I} + \Gamma_{\rm II})_{ii}^{-1}$.

8.2 Numerical implementation

We performed the fisher analysis for circular inspiral with 1 year of evolution before the plunge, defined in Eq. (6.8). We considered EMRI prototypes composed by a central MBH with a mass $M = 10^6 M_\odot$ and spin $a/M = 0.9$, and by a secondary object with $m_p = 10 M_\odot$ and different values of the scalar charge. The source angles were fixed to $\theta_S = \phi_S = \pi/2$ and $\theta_L = \phi_L = \pi/4$.

The sensitivity to small changes during the inspiral, along with the long and computationally expensive waveforms, render parameter estimation of EMRIs a challenging task that requires high precision methods [152]. In the following we present the numerical implementation of the analysis, performed with `Mathematica` [121].

8.2.1 Fluxes and GW templates

We make use of the Black Hole Perturbation Toolkit [120] for the computation of the tensor and scalar energy fluxes. In both cases we have summed multipole contributions up to $\ell = 10$ (see Chapter 5). Fluxes have been sampled as a function of the orbital radius on a grid of 100 equally spaced points within $r \in [8, 2.4]M$, with 300 digits of input precision. Moreover, in order to perform spin derivatives we have computed $\dot{E}$ sampling 11 points of a/M in uniform steps of $\Delta a/M = 0.02$ symmetrically around $a/M = 0.9$. Given that the dependence on the scalar charge can be factored out analytically from the fluxes the overall gravitational wave luminosity which sources the EMRI phase evolution, needs to be numerically interpolated only along the radial coordinate and the spin, namely

$$\dot{E}(r, a/M, d) = \dot{E}_{\rm grav}(r, a/M) + d^2 \dot{E}_{\rm scal}(r, a/M) \ . \tag{8.4}$$

The waveform $h(t)$ has been sampled in the time domain fixing the step $\Delta t = T_{\rm obs}/(2^N - 1)$ such that $1/\Delta t = 2 f_{\rm max}$, where the observation time is $T_{\rm obs} = 1$ year and $f_{\rm max}$ corresponds to the ISCO frequency of a test body in the Kerr background. For the EMRI configurations considered, with $M = 10^6 M_\odot$, $\mu = 10 M_\odot$ and $a/M = 0.9$, this yields $f_{\rm max} \simeq 0.01457$Hz with $\Delta t \simeq 30$ seconds, and a Nyquist frequency of $f_{\rm Ny} = 1/(2\Delta t) \simeq 0.01663$Hz. Before applying the Fourier transform to $h(t = n\Delta t)$ for $n = 0, \dots N-1$, we have tapered the waveform with a Tukey window $w[n]$ to avoid boundary effects:

$$w[n] = \begin{cases} \sin\left[\frac{n\pi}{\tau(1-N)}\right]^2 & 0 \le n \le \frac{\tau(N-1)}{2} \ , \\ 1 & \frac{\tau(N-1)}{2} \le n \le (N-1)(1-\frac{\tau}{2}) \ , \\ \sin\left[\frac{(1+n-N)\pi}{\tau(1-N)}\right]^2 & (N-1)(1-\frac{\tau}{2}) \le n \le N-1 \ . \end{cases}$$

The parameter τ which controls the magnitude of the sinusoidal lobes has been fixed to $\tau = 0.05$. We have performed the Fisher matrix analysis without the Tukey window as well and this has led to a mild improvement of a factor ~ 2 for the errors of the waveform parameters.

8.2.2 Waveform derivatives

Since waveforms are generated fully numerically in the time domain, derivatives appearing in the Fisher matrix are also numerical. We used a centered 11- and 9-point stencil for $(M, m_p, a/M, d, r_0)$ and $(\theta_{\rm S}, \phi_{\rm S}, \theta_{\rm L}, \phi_{\rm L})$ [153, 154], while for the luminosity distance d_L and the initial phase ϕ_0 analytical expressions of $\partial h/\partial\theta_i$ can be computed. In our 11×11 parameter space, inversion of the Fisher matrices may depend on the value of the numerical displacement chosen to compute finite difference of $h(t)$ for a specific parameter, due to numerical instability. Indeed, Fisher matrices for EMRIs are known to feature large condition numbers $\kappa = \max(\lambda_i)/\min(\lambda_i)$, i.e. the ratio between the largest and the smallest eigenvalues [152]. We computed Γ_{ij} using high-precision numerics with fluxes with 300 digits of input precision, which lead to Fisher matrices of ~ 185 digits of final precision, and $\kappa \sim \mathcal{O}(10^{14})$. Calculations of $\mathbf{\Gamma}$ and its inverse are extremely stable leading to discrepancies among Fisher matrices derived with different numerical shifts $\lesssim 0.1\%$. Differences on the source parameters and on the correlations coefficients are also very small, $\lesssim 1\%$. Further details regarding checks on the fisher matrices are provided in Appendix B.

The numerical derivatives for the waveform parameters $\vec{\theta} = (\ln M, \ln m_p, a/M, d, r_0)$ and $\vec{\theta} = (\theta_S, \phi_S, \theta_L, \phi_L)$, computed with a centered 11-point and 9-point stencil respectively, are given by

$$\begin{aligned}
\partial_{\theta_i} h(f, \vec{\theta}) &= \frac{1}{1260\delta\theta_i} \vec{P}^{(11)} \cdot \vec{D}^{(11)} + \mathcal{O}(\delta\theta_i^{10}) \ , \\
\partial_{\theta_i} h(f, \vec{\theta}) &= \frac{1}{840\delta\theta_i} \vec{P}^{(9)} \cdot \vec{D}^{(9)} + \mathcal{O}(\delta\theta_i^{8}) \ ,
\end{aligned} \tag{8.5}$$

where

- $\vec{P}^{(9)} = (3, -32, 168, -672, 0, 672, -168, 32, -3)$,
- $\vec{P}^{(11)} = (-1, 25/2, -75, 300, -1050, 1050, -300, 75, -25/2, 1)$,
- $\vec{D}^{(8)} = (h_{i-4}, h_{i-3}, \ldots, h_{i+3}, h_{i+4})$,
- $\vec{D}^{(11)} = (h_{i-5}, h_{i-4}, \ldots, h_{i+4}, h_{i+5})$,

and $h_{i\pm n} = h(fs, \theta_i \pm n\delta\theta_i)$. For $\theta_i \neq 0$ ($\theta_i = 0$) we set $\delta\theta_i = \theta_i\epsilon_i$ ($\delta\theta_i = \epsilon_i$), with the numerical coefficients $\epsilon_i \ll 1$. The difference in the derivative order is due to the extreme stability of angular parameters which can be treated with a lower order method.

Derivatives with respect to the initial phase and the luminosity distance have an analytic expression since $\partial_{\ln D} h(f) = -h(f)$ and since ∂_{Φ_0} can be directly applied to the time domain waveform:

$$\partial_{\Phi_0} h(t, \vec{\theta}) = -\sqrt{3}\mathcal{A}F_+ \sin[2\Phi(t) + 2\Phi_0](1 + \cos^2\iota) - 2\sqrt{3}\mathcal{A}F_\times \cos[2\Phi(t) + 2\Phi_0]\cos\iota \ . \tag{8.6}$$

We have computed Eq. (8.5) varying the spacings ϵ_i in order to explore the behavior of the derivatives. The choice of ϵ_i is also relevant for the inversion of the Fisher matrix. Further detailes are provided in Appendix B.

Integration over the LISA noise spectral density has been performed using a composite Boole method [155]. We have checked that choosing a lower-order method for the derivatives, or a different method for the frequency integral, do not change our final results.

8.3 Results

We present here the results of the fisher analysis for circular EMRIs with massless scalar fields around rotating black holes. First, we show the errors obtained for the EMRI parameters focusing in particular on the scalar charge carried by the secondary. Finally, we focus on the specific case of shift-symmetric scalar Gauss Bonnet theories, recovering constraints on the fundamental coupling constant of the theory.

8.3.1 Errors on the EMRI parameters

The results of the parameter estimation are summarized in Fig. 8.1 and Fig. 8.2.

Figure 8.1 shows the probability distribution for the component masses, the spin of the primary, and the scalar charge of the secondary, for EMRIs observed one year before the plunge with $d = 0.05$ and SNR of 150.

This analysis shows that a single detection can provide a measurement of the scalar charge with a relative error smaller than 10%, with a probability distribution that does not have any support on $d = 0$ at more than $3 - \sigma$. Off-diagonal panels, yielding 68% and 98% joint probability confidence intervals between the source parameters, also show that the charge is highly correlated with the secondary mass and anti-correlated with the spin parameter and the mass of the primary.

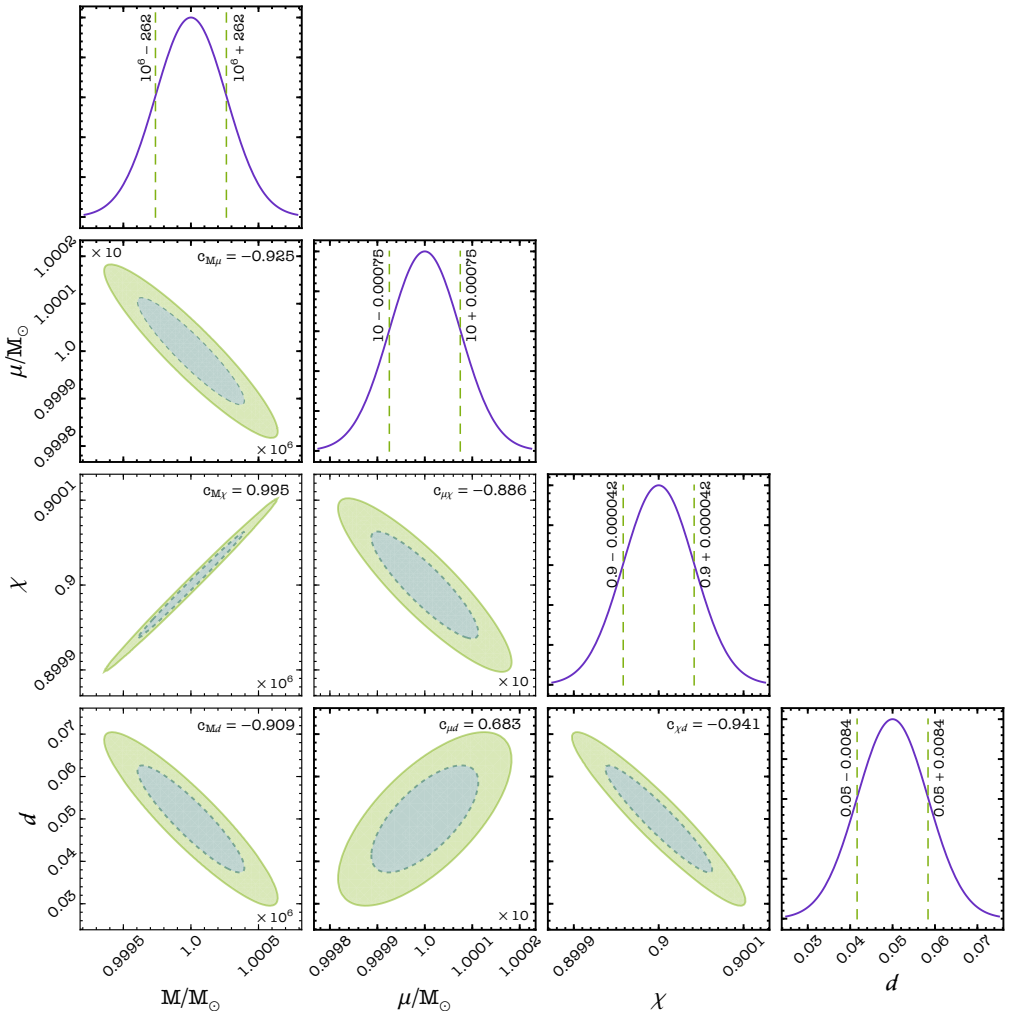

Figure 8.1. Corner plot for the probability distribution of the masses (M, μ), primary spin $\chi = a/M$ and secondary charge d, inferred after one year of observation with LISA. The mass of the secondary object is indicated here with μ. We considered a binary system with $d = 0.05$ and SNR of 150. Diagonal (off-diagonal) boxes refer to marginalized (joint) distributions. Vertical lines show the 1-σ interval for each waveform parameters. Colored contours within the joint distributions correspond to 68% and 95% probability confidence intervals. In the off-diagonal panels we also show the correlation coefficient between the parameters.

Figure 8.2 shows the error in the scalar charge as a function of the scalar charge itself, for EMRIs detected by LISA with SNR ranging from 30 to 150. The errors on d can also be accurately fitted with a simple law of the form $\sigma_{\rm fit} = \beta/d$, where $\beta \simeq 2.09 \times 10^{-3} (4.18 \times 10^{-4})$ for SNR of 30 (150). In the top panel we show the relative error σ_d/d and the analytical fit; in the bottom panel we show the $3-\sigma_d$ intervals around the injected values of the scalar charge.

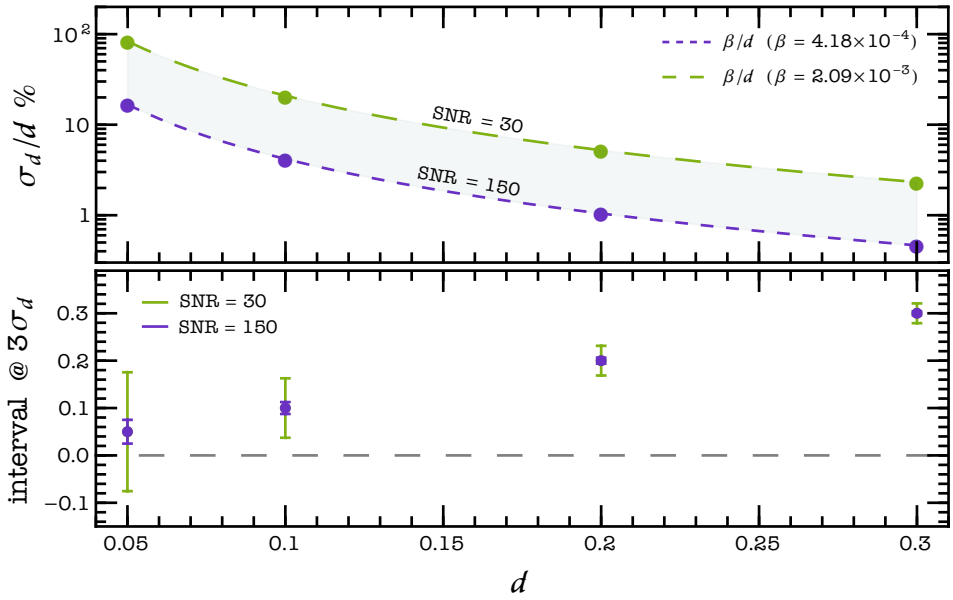

Figure 8.2. Uncertainties on the scalar charge for prototype EMRIs observed with different SNR after one year of observation by LISA. (Top panel) Relative error on the scalar charge as a function of d for EMRIs SNR of 30 and 150. (Bottom panel) 3-σ interval around the true values of the scalar charge inferred from LISA observations with the two values of the SNR also considered in the top panel. Dashed curves in the top panel refer to the analytic fit $\sigma_d = \beta/d$ with $\beta \simeq 4.18 \times 10^{-4}$ and $\beta \simeq 2.09 \times 10^{-4}$ for SNR of 150 and 30, respectively.

Our analysis shows that one year of EMRI observation can pinpoint a scalar charge smaller than ~ 0.3 with percent accuracy. For an SNR of 30 a charge $d \sim 0.1$ could be constrained to consistently exclude the value $d = 0$. For the louder signals we consider, LISA could constrain a scalar charge as small as $d \sim 0.05$ to be inconsistent with zero at $3-\sigma$ confidence level.

8.3.2 Constraints on a specific modified gravity theory

Detecting and measuring the scalar charge of a compact object would be of enormous importance, as first evidence of new physics, regardless of the origin of the charge or the nature of the compact object. Indeed, so far our analysis and results have been theory-agnostic. However, it is worth pointing out that in many cases the scalar charge is uniquely determined by theoretical parameters that mark deviations from GR or the Standard Model. In such cases, a measurement of the scalar charge can be used to measure these parameters. LISA will provide impressive precision for that.

We demonstrate this point using a simple but characteristic example. We assume that the secondary body is a black hole and the scalar field is massless (shift-symmetric). No-hair theorems then dictate that there cannot be a scalar charge unless the scalar field couples to the Gauss–Bonnet invariant, $R_{\rm GB} = R^2 - 4R_{\mu\nu}R^{\mu\nu} + R_{\mu\nu\alpha\beta}R^{\mu\nu\alpha\beta}$, as follows, $\alpha\,\varphi R_{\rm GB}$, where α is the new coupling constant [92]. In this case, the relation between α and the scalar charge d of a BH has the simple form $\alpha \simeq 2d\mu^2 - 73d^3\mu^2/240$ [156].

To study the constraints on α from LISA observations, we draw $N = 10^5$ samples of $(\mu, d)_{i=1,\dots N}$ from the joint probability distribution of the secondary mass and scalar charge obtained from the Fisher analysis. We then compute N values of α building the corresponding probability density functions. Figure 8.3 shows $\mathcal{P}(\sqrt{\alpha})$ for our prototype EMRIs, for $d = 0.05$ and $d = 0.2$. Vertical lines in each panel identify the 90% confidence intervals of the coupling constant. Even for $d = 0.05$ the probability distribution does not have support on $\alpha = 0$. This analysis demonstrates that, in theories where the scalar charge is determined by theoretical parameters, EMRI observations by LISA can be used to measure these parameters with unprecedented accuracy.

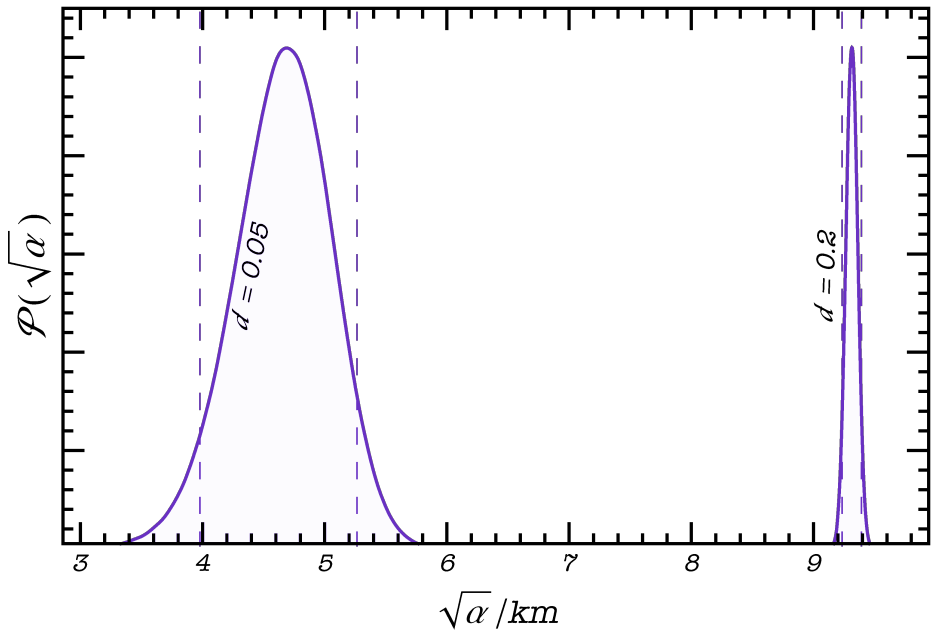

Figure 8.3. Probability distribution of the dimensionful coupling constant of shift-symmetric Gauss Bonnet gravity inferred from constraints made by LISA. Results refer to EMRIs with $d = (0.05, 0.2)$ and SNR of 150. Vertical lines identify 90% intervals around the injected values of the scalar charge, $\sqrt{\alpha} = 4.67^{+0.59}_{-0.69}$ km and $\sqrt{\alpha} = 9.311^{+0.078}_{-0.079}$ km for $d = 0.05$ and $d = 0.2$, respectively (our normalization for α is different from the one used in some of the literature [157, 158]). The height of the $\mathcal{P}(\sqrt{\alpha})$ distribution has been rescaled to unity.

Current upper bounds on $\sqrt{\alpha_{GB}}$ are ~ 1 km, where $\alpha_{\rm GB}$ indicates the Gauss-Bonnet coupling constant with the normalization used in some literature [111, 157–164], and it is related to the constant α of our analysis by $\alpha = 16\pi^{1/2}\alpha_{\rm GB}$, so that $\sqrt{\alpha} \simeq 5.33\sqrt{\alpha_{\rm GB}}$. From the orbital decay of the black hole low-mass X-ray binary A0620-00, Ref. [159] obtained $\sqrt{\alpha_{GB}} \lesssim 1.9$ km. Such constraint is more than six orders of magnitude stronger than the solar system bound [165]. From the mass measurement of the pulsar J0740+6620, Ref. [163] found $\sqrt{\alpha_{GB}} \lesssim 1.29$ km. Other bounds were obtained from GW events, in which the GR wavefrom is modified by taking into account the scalar dipole radiation. From binary black hole (BBH) GW events, Refs. [111], [160], [161], [157], and [162] found $\sqrt{\alpha_{GB}} \lesssim 5.6, 1.85, 4.3, 1.7$ and 4.5 km, respectively. The work of [160] also considered Einstein dilaton Gauss Bonnet theory with a massive scalar field, considering that current detectors are sensitive to the activation of dipolar radiation from massive fields for masses of the scalar in the range between $\sim 10^{-14}$ and 10^{-13} eV, and obtaining $\sqrt{\alpha_{GB}} \lesssim 2.47$ km for any mass of the field less than 6×10^{-14} eV and $\sqrt{\alpha_{GB}} \lesssim 1.85$ km in the massless limit. Finally, Ref. [164] found $\sqrt{\alpha_{GB}} \lesssim 1.33$ km from the GW event GW200115 associated to a NSBH binary, and $\sqrt{\alpha_{GB}} \lesssim 1.18$ km by combining NSBHs and BBHs events. Refs. [111, 157, 164, 166] also looked at constraining dynamical Chern-Simons gravity, without finding meaningful bounds. An upper bound for such theory was found by Ref. [167] from multimessanger NS observations, $\sqrt{\alpha_{dCS}} \lesssim 8.5$ km.

We will investigate upper bounds on the scalar charge carried by the secondary in a fully Bayesian analysis, currently in preparation [168].

In summary, our results demonstrate that EMRI observations by LISA will be able to detect and potentially measure scalar charges to exquisite accuracy. Our analysis and results are independent of the origin of the charge and are hence theory-agnostic. We have also shown that a further analysis can allow one to measure the coupling parameters for specific theories.

Chapter 9

EMRIs with massive scalar fields

So far, our analysis focused on massless scalar fields. In this chapter, we model EMRI with massive scalar fields and we show how, under certain assumptions, at leading order in the binary mass ratio, all the changes on the emitted gravitational waves are fully captured by two parameters: the scalar charge of the secondary body and the mass of the scalar field. These results are presented in Section 9.1, in which we derive the decoupled field equations for the gravitational and the scalar field. In Section 9.2 we present the solution of the massive scalar field equation in linear perturbation theory, and we compute the scalar energy fluxes for circular inspirals. The energy emission drives the EMRI's orbital evolution, discussed in Section 9.4. Finally, the last section is dedicated to the emitted GWs. First, we compute the faithfulness among GW signals arising in different scenarios, and in the end we perform a parameter estimation with the Fisher Information Matrix analysis to investigate the detectability of both the scalar charge and mass from LISA.

9.1 Theoretical framework

Massive scalars appear in cosmological models of dark energy and/or dark matter in extension of the Standard Model or General Relativity.

Massive scalars are expected to leave an observable imprint on compact objects only if their Compton wavelength, the inverse of their mass, is comparable to the wavelength of the emitted GW, i.e. to the length-scale of the source [169]. In geometrical ($G = c = 1$) units, if M is the length-scale of the source (e.g., for a BH system, the BH mass) and $\mu_s\hbar$ is the scalar field mass, the condition is roughly $\mu_s M \lesssim 1$. We note that [94]

$$\mu_s\,[\mathrm{eV}] \simeq \left(\frac{\mu_s M}{0.75}\right) \cdot \left(\frac{10^6 M_\odot}{M}\right) 10^{-16}\,\mathrm{eV}\,. \tag{9.1}$$

Hence, the scalars that GW observations can currently probe would have masses smaller than $\sim 10^{-16}$ eV (*ultra-light scalar fields*, see e.g. [170] and references therein).

Nonetheless, the assumption of a strictly vanishing mass and of shift symmetry, as for the previous studies, can be too restrictive. Certain scenarios, such a superradiance-induced clouds [94] or scalarization [25, 26, 96, 97, 171] rely of the presence of a mass or of interactions that violate shift symmetry to generate scalar charge. Measuring the mass of an ultra-light scalar is in itself an exciting prospect. Indeed, significant effort has already been put in constraining the mass of scalar fields using pulsar or LVK observations, *e.g.* [160, 169, 170, 172].

Here we show how EMRIs result to be very promising sources to set constraints on both the scalar charge and the scalar field mass. Before proceeding, we define here the dimensionless mass of the scalar field as

$$\bar{\mu}_s = \mu_s M \ , \tag{9.2}$$

which is used in the following for simplicity.

9.1.1 Set up

We consider theories described by the action:

$$S\left[\mathbf{g}, \varphi, \Psi\right] = S_0\left[\mathbf{g}, \varphi\right] + \alpha S_{\rm c}\left[\mathbf{g}, \varphi\right] + S_{\rm M}\left[\mathbf{g}, \varphi, \Psi\right] \ , \tag{9.3}$$

where

$$S_0 = \int d^4x \frac{\sqrt{-g}}{16\pi}\left(R - \frac{1}{2}\partial_\mu\varphi\partial^\mu\varphi - \frac{1}{2}\mu_s^2\varphi^2\right) , \tag{9.4}$$

with R being the Ricci scalar and μ_s the mass of the scalar field. The term $S_{\rm c}$ describes the coupling between the scalar and the gravitational field, and $S_{\rm M}$ is the action of the matter fields. By following the skeletonized approach [112] $S_{\rm M}$ is replaced by the action of a point-particle

$$S_{\rm p} = -\int m(\varphi)\sqrt{g_{\alpha\beta}\frac{dy_p^\alpha}{d\lambda}\frac{dy_p^\beta}{d\lambda}}d\lambda\,, \tag{9.5}$$

where $m(\varphi)$ is a scalar function of the massive scalar field. By varying the action (9.4) with respect to the fields $\mathbf{g}$ and φ, we obtain the fields equations, respectively

$$G_{\mu\nu} = -\frac{16\pi\alpha}{\sqrt{-g}}\frac{\delta S_c}{\delta g^{\mu\nu}} + 8\pi T^{\rm scal}_{\mu\nu} + 8\pi T^p_{\mu\nu}, \tag{9.6}$$

and

$$(\Box - \mu_s^2)\varphi = -\frac{8\pi\alpha}{\sqrt{-g}}\frac{\delta S_c}{\delta\varphi} + 16\pi\frac{\delta S_p}{\delta\varphi} \ . \tag{9.7}$$

$T^{\rm scal}_{\mu\nu}$ is the scalar-field stress-energy tensor,

$$T^{\rm scal}_{\mu\nu} = \frac{1}{16\pi}\left[\partial_\mu\varphi\partial_\nu\varphi - \frac{1}{2}g_{\mu\nu}\left(\partial\varphi\right)^2 - \frac{1}{2}\ g_{\mu\nu}\ \mu_s^2\varphi^2\right] \ , \tag{9.8}$$

and $T^p_{\mu\nu}$ is the stress-energy tensor for S_p,

$$T^p_{\mu\nu} = \int m\left(\varphi\right)\frac{\delta^{(4)}(x - y^p(\lambda))}{\sqrt{-g}}\frac{dy^p_\mu}{d\lambda}\frac{dy^p_\nu}{d\lambda}d\lambda \ . \tag{9.9}$$

We assume that α has negative mass dimensions in units where $c = \hbar = 1$ (*i.e.* it suppresses irrelevant operators), or positive length dimensions in the $G = c = \hbar = 1$ geometric units that we use here. Then we can relate α to q as done for massless fields in Chapter 4, $\alpha/M^n = (\alpha/m_p^n)q^n$, where n is a positive integer.

Moreover, since we focus on scalar masses that satisfy $\mu_s M \leq 1$, as heavier scalars are not expected to leave any imprint on EMRIs, we have $\mu_s m_p \ll 1$ and the scalar is far from being confined at scales m_p. The fact that it has not been already detected by observation of black holes of a few solar masses or in weak field [111]

implies that α/m_p^n is not much larger than 1. The $\alpha = 0$ case in particular is covered by no-hair theorems [20, 22] and hence the primary would be a Kerr black hole with $\varphi = 0$.

Combining all of the above, one can treat the deviations from the Kerr metric and the EMRI dynamics perturbatively, with q as a single book-keeping parameter. When $\mu_s M \ll 1$, the mass of the scalar can be neglected and one recovers the results of the massless case, while when $\mu_s M$ becomes $O(1)$ it is essential to include its contribution, as we do below.

We will only consider quantities to leading order in the mass ratio. Hence $T^{\rm scal}_{\mu\nu}$ and $\delta S_c/\delta\varphi$, which are quadratic in q, can be neglected, and we obtain

$$G^{\alpha\beta} = 8\pi \int m(\varphi) \frac{\delta^{(4)}\left(x - y_p(\lambda)\right)}{\sqrt{-g}} \frac{dy_p^\alpha}{d\lambda} \frac{dy_p^\beta}{d\lambda} d\lambda \ , \tag{9.10}$$

$$\left(\Box - \mu_s^2\right) \varphi = 16\pi \int m'\left(\varphi\right) \frac{\delta^{(4)}(x - y_p(\lambda))}{\sqrt{-g}} d\lambda \ . \tag{9.11}$$

The relation between $m(\varphi)$, its derivative and the mass and scalar charge of the secondary object are then obtained by proceeding as in the massless case (see Chapter 4). In a buffer region close to the secondary, small enough to be inside its world-tube, but far away such that the metric can be considered as a perturbation of flat spacetime, Eq. (9.11) reduces to

$$(\Box - \mu_s^2)\varphi_1 = 0 \ , \tag{9.12}$$

whose solution, in a reference frame $\{\tilde{x}_\mu\}$ centered on the particle, has the form

$$\varphi_1 \simeq \frac{m_p d}{\tilde{r}} e^{-\mu_s \tilde{r}} + O\left(\frac{m_p^2 d^2}{\tilde{r}^2} e^{-\mu_s \tilde{r}}\right) \ , \tag{9.13}$$

where d is the dimensionless scalar charge.

By inserting the solution (9.13) in the left hand side of (9.11) and evaluating it in $\tilde{r} = 0$ in the buffer region, we obtain

$$\left(\nabla^2 - \mu_s^2\right) \left(\frac{m_p d}{\tilde{r}} e^{-\mu_s \tilde{r}}\right) = -4\pi m_p d \delta^{(3)}(x - y_p) \tag{9.14}$$

Matching this solution with the right hand side of the scalar field equation (9.11) we then obtain $m'(0) = -m_p d/4$. Finally, by considering the weak-field limit the (tt)-component of the particle's stress-energy tensor reduces to the matter density of the particle $\rho = m_p \delta^{(3)}(x - y_p(\lambda))$ we obtain $m(0) = m_p$. The final matching conditions are then given by:

$$m(0) = m_p \ , \tag{9.15}$$

$$m'(0) = -\frac{m_p \ d}{4} \ . \tag{9.16}$$

The field equations are finally given by:

$$G^{\alpha\beta} = 8\pi m_{\rm p} \int \frac{\delta^{(4)}(x - y_p(\lambda))}{\sqrt{-g}} \frac{dy_p^\alpha}{d\lambda} \frac{dy_p^\beta}{d\lambda} d\lambda \ , \tag{9.17}$$

$$\left(\Box - \mu_s^2\right) \varphi = -4\pi d m_{\rm p} \int \frac{\delta^{(4)}(x - y_p(\lambda))}{\sqrt{-g}} d\lambda \ . \tag{9.18}$$

The field equation (9.17) for the gravitational field is the same that we have in General Relativity, while the scalar field equation (9.18) is a scalar wave equation with a source term controlled by the scalar charge of the secondary body.

9.2 Massive scalar perturbations

The field equations can be solved in perturbation theory. That one for the gravitational field, Eq. (9.17), is the same of the GR one, and the perturbations were presented in Chapter 5. In this section, we present the perturbations for the massive scalar field. Following [36, 173], we decouple the radial and the angular dependence of the scalar field by decomposing it in the zero-spin spheroidal harmonics $S_{\ell m}(\theta, \omega)$ as (the sum over the multipoles ℓ and m is implicit)

$$\varphi(t, r, \theta, \phi) = \int {\rm d}\omega \frac{\tilde{R}_{\ell m}(r, \omega)}{\sqrt{r^2 + a^2}} S_{\ell m}(\theta, \omega) e^{im\phi} e^{-i\omega t} \ . \tag{9.19}$$

Substituting it in Eq. (9.18), we obtain two decoupled equations, one for the radial and one for the angular dependence of the field, $\tilde{R}_{\ell m}$ and $S_{\ell m}(\theta, \omega)$, respectively.

The equation for the zero-spin spheroidal harmonic is

$$\left[\frac{1}{\sin\theta}\frac{d}{d\theta}\left(\sin\theta \frac{d}{d\theta}\right) - a^2(\omega^2 - \mu_s^2)\sin^2\theta - \frac{m^2}{\sin^2\theta} + \bar{\lambda}_{\ell m}\right] S_{\ell m} = 0 \ , \tag{9.20}$$

where $\bar{\lambda}_{\ell m}$ is the eigenvalue. The equation for $\tilde{R}_{\ell m}$ is

$$\frac{d^2 \tilde{R}_{\ell m}}{dr_\star^2} + V_s \tilde{R}_{\ell m} = J_{\ell m} \ , \tag{9.21}$$

where the tortoise coordinate $r_\star$ is defined in (5.14) and the effective potential V_s is given by

$$V_s = \left[\omega - \frac{am}{\rho^2}\right]^2 - \frac{\Delta}{\rho^8}\left[\lambda_{\ell m}\rho^4 + 2Mr^3 + a^2(\Delta - 2Mr) + \frac{\mu_s^2}{\rho^6}\right] \ , \tag{9.22}$$

with $\rho^2 = r^2 + a^2$, $\lambda_{\ell m} = \bar{\lambda}_{\ell m} + 2ma\sqrt{\omega^2 - \mu_s^2} - 2ma\omega$.

The source term $J_{\ell m}$, for a particle moving on a circular orbit with radius $r_{\rm p}$ and (prograde) angular frequency $\Omega_p = M^{1/2}/(r_p^{3/2} + aM^{1/2})$, is

$$J_{\ell m} = -d\frac{4\pi m_{\rm p}\Delta}{\sqrt{a^2 + r^2}} \frac{S^\star_{\ell m}(\pi/2)}{u^t} \delta(r - r_{\rm p})\delta(\omega - m\Omega_{\rm p}) \, . \tag{9.23}$$

where u^t is the time component of the particle four-velocity, $dt/d\tau$ given in Eq. (3.10).

The equation for $R_{\ell m}$ is solved using the method of the Green functions. The homogeneous solutions $R^-_{\ell m}/R^+_{\ell m}$ which satisfy the condition of purely ingoing/outgoing wave at the horizon/infinity have the following asymptotic behaviour:

$$\begin{cases} R^-_{\ell m} = e^{-ik_- r_\star} & \text{for } r \to r_+ \ , \\ R^-_{\ell m} = A_{\rm in} e^{-ik_+ r_\star} + A_{\rm out} e^{ik_+ r_\star} & \text{for } r \to \infty \ , \end{cases} \tag{9.24}$$

$$\begin{cases} R^+_{\ell m} = B_{\rm in} e^{-ik_- r_\star} + B_{\rm out} e^{ik_- r_\star} & \text{for } r \to r_+ \ , \\ R^+_{\ell m} = e^{ik_+ r_\star} & \text{for } r \to \infty \, . \end{cases} \tag{9.25}$$

with $k_+ = \sqrt{\omega^2 - \mu_s^2}$, $k_- = \omega - m\Omega_h$, $\Omega_+ = a/(2Mr_+)$, $r_+ = M + \sqrt{M^2 - a^2}$.

The general solution for $R_{\ell m}(\omega, r)$ is then obtained by integrating the former over $J_{\ell m}$:

$$\tilde{R}_{\ell m} = \tilde{R}^+_{\ell m} \int_{-\infty}^{r_\star} \frac{\tilde{R}^-_{\ell m} J_{\ell m} {\rm d}r_\star}{W} + \tilde{R}^-_{\ell m} \int_{r_\star}^{+\infty} \frac{\tilde{R}^+_{\ell m} J_{\ell m} {\rm d}r_\star}{W} \ , \tag{9.26}$$

where $W = \tilde{R}'^+_{\ell m} \tilde{R}^-_{\ell m} - \tilde{R}^+_{\ell m} \tilde{R}'^-_{\ell m}$ is the Wronskian and primes denote derivatives with respect to $r_\star$. We define the amplitudes $Z^\pm_{\ell m} = \tilde{R}_{\ell m}(r_\star \to \pm\infty)$ so that

$$Z^\mp_{\ell m} = \tilde{R}^\mp_{\ell m}(r_\star \to \mp\infty) \int_{-\infty}^{+\infty} \frac{\tilde{R}^\pm_{\ell m} J_{\ell m} {\rm d}r_\star}{W} \ . \tag{9.27}$$

The energy flux at the horizon $(-)$ and at infinity $(+)$ are then given by

$$\dot{E}^\mp_{\rm scal} = \frac{1}{16\pi} \sum_{\ell=1}^{\infty} \sum_{m=-\ell}^{\ell} \omega k_\mp |Z^\mp_{\ell m}|^2 \ , \tag{9.28}$$

with $\omega = m\Omega_{\rm p}$.

Moreover, we observe that since $\tilde{R}^+_{\ell m}(r_\star \to +\infty) = e^{-i\omega r_\star}$ $\Theta(m\Omega_{\rm p} - \mu_s)$ with Θ Heaviside function, we have

$$\left| Z^+_{\ell m} \right|^2 = \left| \int_{-\infty}^{+\infty} \frac{\tilde{R}^-_{\ell m} J_{\ell m} {\rm d}r_\star}{W} \right|^2 \Theta(m\Omega_{\rm p} - \mu_s) \, . \tag{9.29}$$

9.3 Energy fluxes: implementation and results

The energy fluxes for circular orbits around rotating central black holes, have been computed by implementing a code using the software `Mathematica` [121].

9.3.1 Numerical implementation

The spheroidal harmonics and their eigenvalues have been computed with the use of the Black Hole Perturbation Toolkit [120], using the package "Spheroidal Harmonics".

To find the general radial solution, we first obtained the homogeneous solution satisfying the boundary conditions of purely ingoing wave at the horizon and purely outgoing wave at infinity, i.e.

$$\tilde{R}_H(r) = \sum_{n=0}^{n_h} e^{-ik_- r_\star(r)} a_n (r - r_h)^n \ , \tag{9.30}$$

$$\tilde{R}_\infty(r) = \sum_{n=0}^{n_\infty} e^{ik_+ r_\star(r)} r^{\frac{i\mu_s^2 M}{\sqrt{\omega^2-\mu_s^2}}} \frac{b_n}{r^n} \ . \tag{9.31}$$

The coefficients (a_n, b_n) are obtained by solving the homogeneous equation at each order in $(r - r_h)$ and $1/r$, with $a_0 = b_0 = 1$. The higher order is set to $n_h = n_\infty = n_{\rm max} = 4$, which guarantees accurate boundary conditions. Indeed, the relative difference in the dominant $\ell = m = 1$ mode of the scalar flux computed with $n_{\rm max} = 3$ and $n_{\rm max} = 4$ is $\lesssim 10^{-10}\%$ within the integration domain $2.4M \leq r \leq 15M$ and $0.01 \leq \bar{\mu}_s \leq 1$. The dimensionless scalar field mass $\bar{\mu}_s$ is defined in Eq. (9.2) as $\bar{\mu}_s = \mu_s M$.

We integrate the field's equations from $r_1 = r_h + 2\epsilon$, with $\epsilon = 10^{-5}$, to a value at infinity, r_2, which is either fixed to (i) $r_2 = 1000/\text{Abs}[\omega]$ if $\omega > \mu_s$ or (ii) such that $\tilde{R}_\infty(r_2) \sim 10^{-50}$ if $\omega < \mu_s$. The last condition is chosen to avoid accuracy problems due to the exponential decay of $\tilde{R}_\infty(r_2)$ for wavelengths smaller than the scalar field Compton mass.

The total gravitational and scalar emissions have been computed by summing over the modes (ℓ, m), with $\ell_{\rm min} \leq \ell \leq \ell_{\rm max}$ and $-\ell \leq m \leq \ell$. For the gravitational (scalar) perturbations, $\ell_{\rm min} = 2$ ($\ell_{\rm min} = 1$). We chose $\ell_{\rm max} = 10$ both for the gravitational and the scalar computations. For the gravitational emission, the relative difference between the fluxes with $\ell_{\rm max} = 9$ and with $\ell_{\rm max} = 10$ is $\sim 0.1\%$ for $r = 2.5M$ and $\sim 10^{-4}\,\%$ for $r = 8M$. For the scalar emission, the relative differences for different values of the scalar field mass are reported in Table 9.1. We observe that the relative difference is $< 1\%$ for $r = 2.5M$ and $< 10^{-2}\,\%$ for $r = 8M$, with scalar field mass in the range $0.001 \leq \bar{\mu}_s \leq 0.1$. For larger values of the scalar mass, $\bar{\mu}_s \sim 1$, the relative difference for $r = 2.5M$ is larger.

$\bar{\mu}_s$	r/M	$\dot{E}_{\rm scal}^{\ell_{\rm max}=10}$	$\dot{E}_{\rm scal}^{\ell_{\rm max}=9}$	Rel. Diff.
0.001	2.5	7.56×10^{-4}	7.53×10^{-4}	$< 1\%$
	8	1.54×10^{-5}	1.54×10^{-5}	$< 10^{-3}\%$
0.01	2.5	7.55×10^{-4}	7.52×10^{-4}	$< 1\%$
	8	1.44×10^{-5}	1.44×10^{-5}	$< 10^{-3}\%$
0.1	2.5	6.40×10^{-4}	6.37×10^{-4}	$< 1\%$
	8	-4.04×10^{-7}	-4.04×10^{-7}	$< 10^{-2}\%$
1	2.5	-3.15×10^{-6}	-3.54×10^{-6}	$\simeq 10\%$
	8	-4.98×10^{-13}	-4.98×10^{-13}	$< 10^{-7}\ \%$

Table 9.1. Relative difference between scalar energy flux computed up to $\ell = 10$ and values computed up to $\ell = 9$. The primary spin is $a/M = 0.9$.

Finally, in order to derive the EMRI phase evolution, we interpolate the GW fluxes over the radial coordinate using a built-in function of `Mathematica`. For a fixed primary spin and scalar field mass, we compute the fluxes over a grid of 251

points uniformly spaced in $u = (r - 0.9\ r_{\rm ISCO})^{1/2}$ within $[u(r_{\rm min}), u(r_{\rm max})]$, where $r_{\rm max} = r_{\rm min} + 13M$ and $r_{\rm min} = r_{\rm ISCO} + 0.1M$, with $r_{\rm ISCO}$ being the value of the radial coordinate at the ISCO as a function of the primary spin a.

In order to have an estimate of the error brought by the interpolation, we computed the scalar fluxes for some orbital radii which don't lie on the grid defined above, and compared them with those obtained through the grid interpolation. The results are given in Table 9.2. The relative difference is $\lesssim 10^{-3}$ for $\bar{\mu}_s \lesssim 0.1$. For higher values of the scalar field mass, the relative difference increases, since the flux at infinity vanishes for the modes with lower m and the total flux experiences large variations between close points on the grid.

$\bar{\mu}_s$	r/M	$\dot{E}^{\ell_{\rm max}=10}_{\rm scal}$	$\dot{E}^{\rm int}_{\rm scal}$	Rel. Diff.
0.001	2.5	7.56×10^{-4}	7.56×10^{-4}	$< 10^{-8}$ %
	8	1.54×10^{-5}	1.54×10^{-5}	$< 10^{-3}$ %
0.01	2.5	7.55×10^{-4}	7.55×10^{-4}	$< 10^{-8}$ %
	8	1.44×10^{-5}	1.44×10^{-5}	$< 10^{-3}$ %
0.1	2.5	6.40×10^{-4}	6.399×10^{-4}	$< 10^{-8}$ %
	8	-4.04×10^{-7}	-2.81×10^{-7}	$\simeq 30\%$
1	2.5	-3.15×10^{-6}	-1.20×10^{-6}	$\simeq 60\%$
	8	-4.98×10^{-13}	-3.62×10^{-13}	$\simeq 30\%$

Table 9.2. Relative difference between scalar energy flux computed up to $\ell = 10$ and the interpolated values, identified by the superscript "int". The primary spin is $a/M = 0.9$.

In the following we present the results of our computations.

9.3.2 Results

The massive scalar energy fluxes feature particular characteristics, which regard the emission at the infinity and the emission at the horizon.

Indeed, the flux at infinity identically vanishes for frequencies smaller than the scalar field mass, $\omega < \mu_s$, see Eq. (9.29). This is a typical behaviour for massive scalar fields (see e.g. [172, 174, 175]). Therefore, for every combination of (ℓ, m) a specific radius $r_{\rm s}$ exists such that for $r > r_{\rm s}$ the energy flux at infinity vanishes. This suppression may lead to non-detectable imprints in the GW emission, as we discuss in the faithfulness analysis.

Unlike the emission at infinity, the flux at horizon is present for each value of the orbital frequency, and contributes to the binary's orbital evolution throughout the entire inspiral. Moreover it shows a new important feature, the appearence of resonances, which are not present if the scalar field is massless.

Resonances occur when the binary orbital frequencies are comparable with those of the scalar quasi-normal modes of the BH background spacetime. In this case the energy emission grows towards a peak which can be either positive or negative depending on the BH spin and on the superradiance condition $\omega < m\Omega_+$, where Ω_+ is the horizon angular velocity, $\Omega_+ = a/(2Mr_+)$, and r_+ the radius of the BH horizon, $r_+ = M + \sqrt{M^2 - a^2}$ (see Eq. (3.2)). If the peak is negative the scalar radiation can be strong enough to counterbalance the gravitational emission, giving rise to floating orbits [176–178]. Determining whether floating orbits persist at post-adiabatic level or how quickly the secondary moves through a resonance requires self-force calculations [178]. Hereafter, we neglect resonances, which is a

rather conservative approach. Taking them into account is expected to make the waveform more distinguishable from a EMRI waveform in GR and hence improve parameter estimation and our ability to detect a new scalar.

The results of the energy fluxes computations are shown in Fig.9.1, where the total scalar energy flux is plotted as a function of the orbital radius, for different values of the scalar field mass. The inset shows a zoom of the same plot, to highlight the behavior of the flux for $\bar{\mu}_s = 0.7$ and $\bar{\mu}_s = 1$. The continuous light-blue line is relative to the massless case, $\bar{\mu}_s = 0$. For a fixed r_p, by increasing the value of the scalar field mass, the energy flux decreases. Moreover, for high values of $\bar{\mu}_s$, $\bar{\mu}_s = 0.7$ and 0.9, the total flux becomes negative for r larger then a certain value, due to the suppression of the flux at infinity.

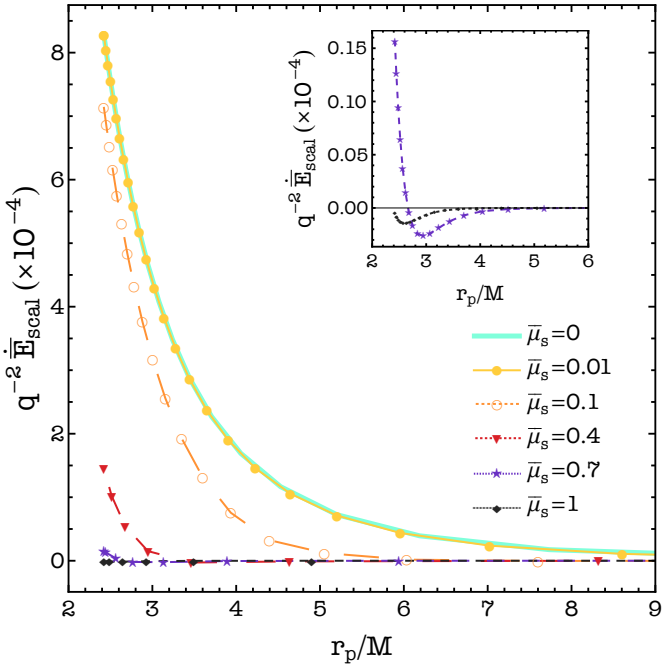

Figure 9.1. Total massive scalar flux up to $\ell = 10$ as a function of the orbital radius r_p, for different values of the scalar field mass. Resonances are excluded. The inset shows the fluxes for $\bar{\mu}_s = (0.7, 1)$. The primary spin is fixed to $a/M = 0.9$. The continuous line is relative to the massless case.

9.4 Orbital Evolution of EMRIs with massive scalar fields

The energy emission through gravitational and scalar waves drives the EMRI evolution. The adiabatic inspiral is built considering the balance law $\dot{E} = -\dot{E}_{GW}$ and integrating the differential equations (6.4) to obtain the radial and phase evolution, as explained for the massless case in Chapter 6. From the orbital evolution, we computed the accumulated dephasing of Eq. (6.6) in 1 year of observation before the plung, for inspirals with and without the scalar charge, for several values of the scalar field mass. The plunge is defined in Eq. (7.8) as $r_{\rm plunge} = r_{\rm ISCO} + \delta r$, with $\delta r = 0.1M$.

The results are presented in Fig. 9.2, which shows the accumulated dephasing as a function of the observing time, for different values of the scalar field mass and $d = 0.1$. The top panel considers a primary with $M = 10^6 M_\odot$, while the bottom panel with $M = 2.3 \times 10^5 M_\odot$. The primary spin is $a/M = 0.9$. The mass of the secondary is $m_p = 10 M_\odot$ in each inspiral. The horizontal dashed line at $\Delta\phi = \pm 0.1$ rad indicates the threshold of LISA's phase resolution for signals with SNR = 30, see Eq. (6.5). The markers indicates the orbital radius reached by the inspiral with $d = 0$ for the corresponding time of observation.

We focused on values of the scalar field mass $0.1 \lesssim \bar{\mu}_s \lesssim 1$, as for lighter values we expect a qualitative behaviour similar to the massless case. Such values are considered in the next analysis concerning the GW signals.

For each $\bar{\mu}_s$, regardless of M, $\Delta\phi$ decreases during the evolution before increasing in the last few months of the inspiral. This behavior is due to the presence of the scalar flux at infinity, which shifts the total scalar emission from negative to positive values, thus accelerating the inspirals with $(d, \bar{\mu}_s) \neq 0$. For $M = 10^6 M_\odot$ the crossing between negative and positive values of the dephasing occurs for $\bar{\mu}_s \lesssim 0.3$ ($\mu_s \lesssim 4 \times 10^{-17}$eV), while for $M = 2.3 \times 10^5 M_\odot$ it happens for $\bar{\mu}_s \lesssim 0.1$ ($\mu_s \lesssim 6 \times 10^{-17}$eV). This analysis shows that light fields, with $\bar{\mu}_s \ll 1$, lead in general to differences in the phase evolution which in modulo are larger than the detectability threshold, thus potentially measurable by LISA. The actual constraints on the scalar field properties require though to fully take into account correlations between the waveform parameters, as discussed in Section 9.6.

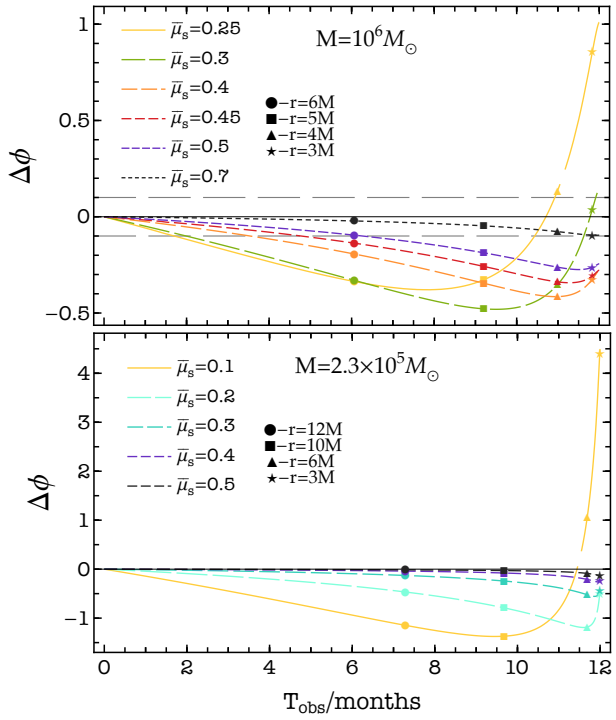

Figure 9.2. (Top) Dephasing accumulated in one year before the plunge, plotted as a function of the time of observation for a binary system with $M = 10^6 M_\odot$, $a/M = 0.9$ and $m_p = 10 M_\odot$, for different values of the scalar field mass. The difference in the phase evolution is computed between an inspiral with $d = 0$ and one with $d = 0.1$. (Bottom) Same as top panel but for a primary mass of $M = 2.3 \times 10^6 M_\odot$. Different values of the scalar field mass are considered.

9.5 Faithfulness among gravitational waves signals

The GW templates have been built by following the Analytic Kludge of [135] presented in Chapter 6. We adapted the template to inspirals driven by the fully-relativistic energy fluxes, computed as previously explained.

We computed the faithfulness among the GW signals emitted in different scenarios, in order to estimate the LISA ability to distinguish among them. With respect to the circular massless case discussed in Chapters 6 and 8, the new parameter $\bar{\mu}_s$ is added to the set of parameters which describe EMRIs, i.e. $\vec{\theta} = \{M, m_p, a/M, d_L, \theta_S, \phi_S, \theta_L, \phi_L, r_0, \phi_0, d, \bar{\mu}_s\}$. The value of the threshold under which two signals are considered distinguishable is assumed $\mathcal{F}_{\rm thr} = 0.994$, for signals with SNR $\rho = 30$ [145].

9.5.1 Results

The results of the faithfulness computations are summarized in Fig. 9.3.

First, we studied the distinguishability between the baseline GR model, i.e. assuming $(d, \bar{\mu}_s) = (0, 0)$, and waveforms with non-vanishing values of the charge and of the scalar field mass. The top panel of Fig. 9.3 shows the faithfulness between the 'plus' polarization h_+ computed in these two scenarios, for EMRIs with secondary mass of one and ten solar masses, as a function of d and $\bar{\mu}_s$. As previously discussed, large values of $\bar{\mu}_s$ tend to suppress the GW flux at infinity, and hence the overall dissipative contribution of the scalar sector, as the energy emission at the horizon is subdominant.

Indeed, the faithfulness deteriorates rapidly as the scalar field mass decreases. For $0.05 < d < 0.1$, it lies below $\mathcal{F}_{\rm thr}$ for $\bar{\mu}_s \lesssim 0.3$ for the binaries we considered. Larger values of the scalar charge ($d = 0.3$) allow the two waveforms to be distinguishable for more massive scalar configurations, with $\bar{\mu}_s \gtrsim 0.7$. For a lighter secondary the faithfulness appears to reach $\mathcal{F}_{\rm thr}$ at a larger $\bar{\mu}_s$.

However, the $d = 0.3$ case is an outlier in this respect and also exhibits some additional peaks and troughs for larger values of $\bar{\mu}_s$, which persists for larger values of d. The corresponding fluxes do not exhibit any remarkable difference from those corresponding to lower values of d or $\bar{\mu}_s$, so it is not clear what causes these changes in the faithfulness for larger values of d and $\bar{\mu}_s$. Numerical errors were analysed by varying the precision p of the fluxes which serve as input parameters for the faithfullness computations. Results are listed in Table 9.3 for different values of input precision and EMRI configurations. Our analysis shows that the results are stable under large the increase of the flux precision, from $p = 40$ to $p = 60$.

$m_p/M_\odot$	d	$\bar{\mu}_s$	$\mathcal{F}_{\rm p=40}$	$\mathcal{F}_{\rm p=50}$	$\mathcal{F}_{\rm p=55}$	$\mathcal{F}_{\rm p=60}$
10	0.1	0.1	0.356456	0.356472	0.356461	0.356462
	0.3	0.4	0.420629	0.420662	0.420632	0.420632
1	0.1	0.1	0.359169	0.359168	0.359168	0.359166
	0.3	0.4	0.466751	0.466753	0.466751	0.466750

Table 9.3. Values of the faithfullness computed with different input precision. The precision p of the fluxes ranges between 40 and 60 digits.

We also note that for $\bar{\mu}_s \lesssim 0.03$ ($\mu_s \lesssim 4 \cdot 10^{-18}$eV) the GR and the scalar waveforms are clearly distinguishable, with $\mathcal{F} \lesssim 0.4$, regardless of the charge. Such

estimates are complementary to other bounds which are expected to provide information on the existence of scalar fields in the gravity sector from future astrophysical probes. As an example, in both panels of Fig. 9.3 we drew as shaded regions the parameter space which can be potentially ruled out by superradiance constraints inferred from observations of massive BH binaries [94]. Our results suggest that, depending on d, EMRIs provide a new powerful channel to constrain both light and heavy fields, which do not fall within the superradiance window.

As a step forward in this analysis we exploited the faithfulness to assess the minimum $\bar{\mu}_s$ which can be distinguished from the massless case. The bottom panel of Fig. 9.3 shows indeed the values of $\mathcal{F}$ computed between the gravitational waveform with 'plus' polarization with either $\bar{\mu}_s = 0$ or $\bar{\mu}_s \neq 0$, and fixed scalar charge. We considered the same binaries analysed in the top panel.

Our results show that, for charges as small as $d \sim 0.05$, LISA could be able to distinguish fields with $\bar{\mu}_s \gtrsim 0.01$ ($\mu_s \sim 10^{-18}$eV) from their massless counterpart. This bound is larger by almost an order of magnitude if $d \gtrsim 0.3$.

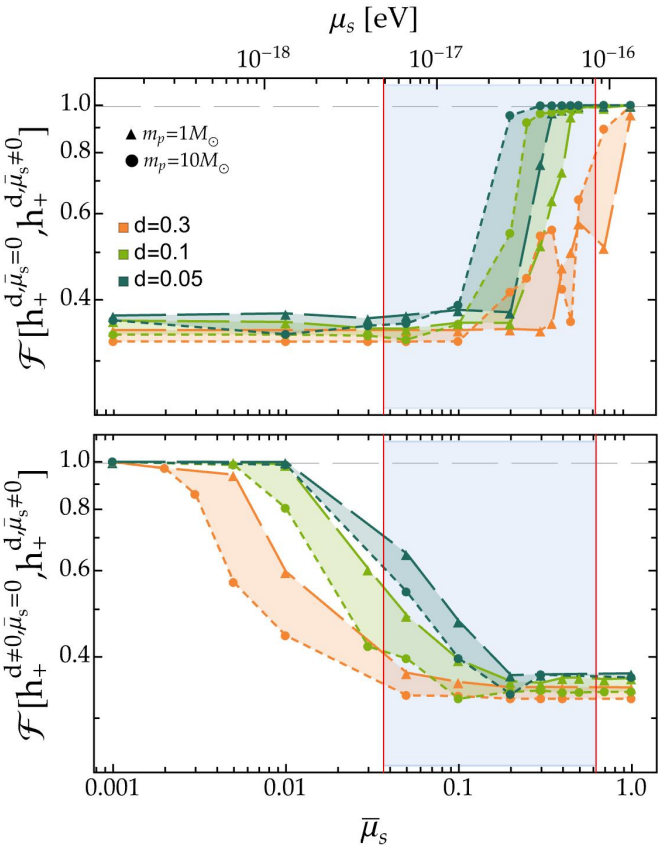

Figure 9.3. (Top) Faithfulness between a GW signal with 'plus' polarisation with $d = 0$ and one with $d \neq 0$, $\bar{\mu}_s \neq 0$ for 12 months of observation before the plunge. We fix the primary mass and spin to $M = 10^6 M_\odot$ and $a/M = 0.9$, respectively, while considering different values m_p and d. The shaded region corresponds to the range of scalar field masses which could be excluded by superradiance bounds (courtesy of R. Brito). (Bottom) Faithfulness between two signals with the same value of $d \neq 0$, one having $\bar{\mu}_s = 0$ and the other with $\bar{\mu}_s \neq 0$. The horizontal dashed line corresponds to the threshold value $\mathcal{F}_{\rm thr}$. We consider the same EMRI configurations as in the top panel.

9.6 Parameter estimation with the Fisher Information Matrix Analysis

Here we present the FIM analysis for massive scalar fields. First we show its numerical implementation and then the obtained results.

9.6.1 Numerical implementation

We applied the fisher analysis to LISA observations of prototype EMRIs injecting $M = 10^6 M_\odot$, $a/M = 0.9$, $\theta_S = \phi_S = \pi/2$, $\theta_L = \phi_L = \pi/4$, $d = 0.1$ and considering four values of $m_p = (1.4, 4.6, 10, 15) M_\odot$ and two values of $\bar{\mu}_s = (0.018, 0.036)$, which lie outside the superradiance window highlighted in Fig. 9.3, and for which the flux at infinity is significant throughout the entire inspiral.

Unlike the faithfulness analysis, we performed the fisher computations by considering only the fundamental mode of the scalar flux, i.e. assuming $\ell_{\rm max} = 1$ in the sum (9.28). This choice was dictated by the computational cost needed to invert the Fisher matrix, whose stability requires very accurate fluxes, computed on the grid $(r/M, a/M, \bar{\mu}_s)$ with 205 digits of input precision.

Derivatives of the analytic template with respect to the binary parameters are fully numerical, obtained by using a 11-points stencil. To compute finite differences we have sampled the spin parameter between $0.89 \leq a/M \leq 0.91$ in steps of $\Delta a/M = 0.01$, and the scalar field mass in an interval of 11, equally spaced points, in steps of $\Delta\bar{\mu}_s = 0.002$ (centered around the two injected values we considered, i.e. $\bar{\mu}_s = 0.018$ and $\bar{\mu}_s = 0.036$). Finite differences require a careful choice of a step-size which controls the shift for each of the twelve parameters of the waveform, and which is discussed in Appendix B.2.

9.6.2 Results

The results of the FIM computations are summarized in Fig 9.1, in which the left and right columns shows the joint and marginal posterior distributions on $\bar{\mu}_s$ and d, respectively. The upper raw is relative to $\bar{\mu}_s = 0.036$, while the bottom raw to $\bar{\mu}_s = 0.018$.

A summary of the 1-σ uncertainties inferred for $\bar{\mu}_s$ and d is reported in Table 9.4, together with their correlation coefficients, which show how $\bar{\mu}_s$ and d are strongly (anti-) correlated.

$m_p[M_\odot]$	$\bar{\mu}_s$	σ_d/d	$\sigma_{\bar{\mu}_s}/\bar{\mu}_s$	$c_{d\bar{\mu}_s}$
1.4	0.018	345%	2364%	0.997
	0.036	363%	391%	0.992
4.6	0.018	92%	243%	0.995
	0.036	97%	8%	−0.485
10	0.018	49%	53%	0.984
	0.036	45%	24%	−0.990
15	0.018	38%	22%	0.938
	0.036	26%	21%	−0.986

Table 9.4. 1-σ relative uncertainties and correlation coefficients on the charge and on the scalar field mass for the configurations shown in Fig. 9.4. We assume $d = 0.1$ for all the binaries.

Errors on d decrease as the mass ratio m_p/M increases, for both values of $\bar{\mu}_s$. Binaries with $m_p \gtrsim 10M_\odot$ are able to exclude the $d = 0$ case at more than 90% credible level. For the EMRI configuration with $m_p = 4.6M_\odot$, errors slightly deteriorate, with the null scenario ruled out at one sigma.

Constraints on $\bar{\mu}_s$ show more variability. For the lowest injected value, $\bar{\mu}_s = 0.018$, errors follow the same hierarchy observed for the scalar charge, with the measurement accuracy improving for heavier secondaries. In this setup however, $\bar{\mu}_s$ remains unconstrained for the EMRI with $m_p = 4.6M_\odot$. This picture changes completely for the $\bar{\mu}_s = 0.036$ case, in which the strongest bound is led by the lightest secondary. Binaries with $m_p = 10M_\odot$ and $m_p = 15M_\odot$ provide larger, and almost identical, errors. The dependence on such results on the secondary mass is mostly dictated by two ingredients: (i) correlations among the scalar charge and the field's mass, (ii) the EMRI orbital configuration within the observational window we have considered, which spans one year of evolution until the plunge. Very light secondaries start their inspiral at smaller initial radii, where the scalar flux has a smaller relative contribution compared to the dominant quadrupolar mode, and the signal features a very slow evolution with little variation in the frequency content.

In comparison with the massless case, where the relative error on the scalar charge for the binary with $m_p = 10M_\odot$ is $\simeq 4\%$, here it is larger: $\sigma_d/d \simeq 45\%$ and 49% for $\bar{\mu}_s = 0.036$ and $\bar{\mu}_s = 0.018$ respectively. This is expected due to correlations with $\bar{\mu}_s$ which enters now as an additional parameter. Nevertheless, in all cases in which the probability distribution of $\bar{\mu}_s$ is constrained by the data, we are able to exclude the massless scenario at more than 90% credible level.

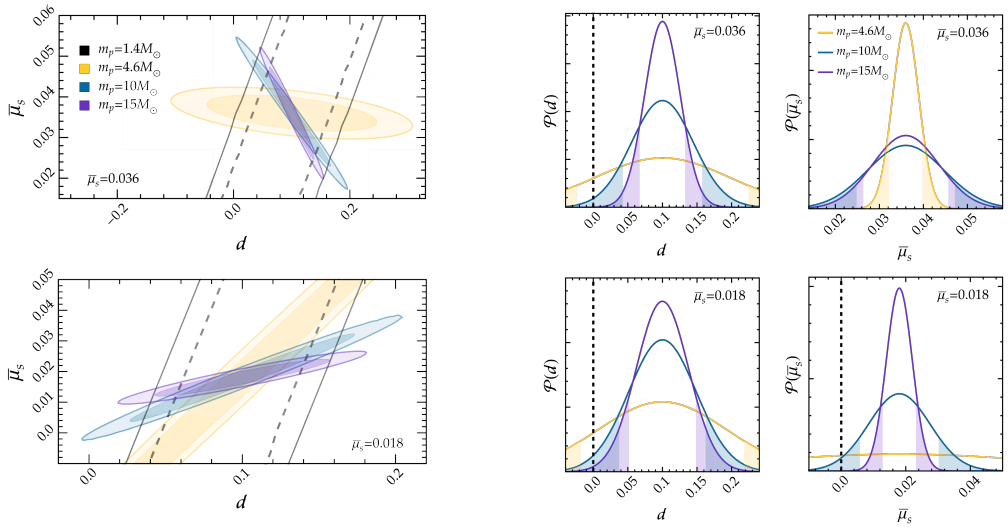

Figure 9.4. (Left column) Credible intervals at 68% and 90% for the joint posterior distribution of the charge d and the scalar field mass $\bar{\mu}_s$. We consider EMRIs with injected parameters $d = 0.1$, $M = 10^6 M_\odot$, $a = 0.9M$, different values of the secondary mass, $\bar{\mu}_s = 0.036$ (top row), and $\bar{\mu}_s = 0.018$ (bottom row). (Right column) Marginal distributions for d and $\bar{\mu}_s$. The white area between shaded regions provides 90% of the probability distribution. The vertical dashed lines identify the GR scenario with $d = \bar{\mu}_s = 0$.

Finally, to quantify the bias that could arise in the error analysis by neglecting multipoles larger than $\ell = 1$ for the scalar flux, we have performed a Fisher analysis

for a configuration with $\bar{\mu}_s = 0.018$, by also including the $\ell = 2$ and the $\ell = 3$ modes within the sum (9.28). The probability distributions for the charge and for the scalar field mass obtained by adding the $\ell = 2$ component are presented in Fig. 9.5. Dashed and solid curves correspond to assuming either $\ell_{\rm max} = 1$, or $\ell_{\rm max} = 2$. As expected, constraints on both $\bar{\mu}_s$ and d improve by adding the quadrupole contribution, making our choice rather conservative in terms of the constraints that LISA would be able to infer from EMRI observations. Table 9.5 shows a comparison of the relative errors obtained by also adding the $\ell = 3$ mode. For the binary configurations we considered, our results suggest that the uncertainties on both the parameters tend to saturate already with the inclusion of the third multipole.

$m_p[M_\odot]$	$\sigma_d^{(1)}/d$	$\sigma_d^{(2)}/d$	$\sigma_d^{(3)}/d$	$\sigma_{\bar{\mu}_s}^{(1)}/\bar{\mu}_s$	$\sigma_{\bar{\mu}_s}^{(2)}/\bar{\mu}_s$	$\sigma_{\bar{\mu}_s}^{(3)}/\bar{\mu}_s$
4.6	92%	75%	78%	243%	198%	190%
10	49%	42%	44%	53%	44%	41%
15	38%	33%	35%	22%	18%	17%

Table 9.5. Relative percentage errors on the parameters $(d, \bar{\mu}_s)$ for $m_p = (4.6, 10, 15)M_\odot$ assuming different $\ell_{\rm max}$ in the scalar energy flux sum (9.28). The value of $\ell_{\rm max}$ is indicated in parenthesis in the superscripts, i.e. $\sigma_d^{(1)} = \sigma_d^{\ell_{\rm max}=1}$. The injected values are $d = 0.1$ and $\bar{\mu}_s = 0.018$.

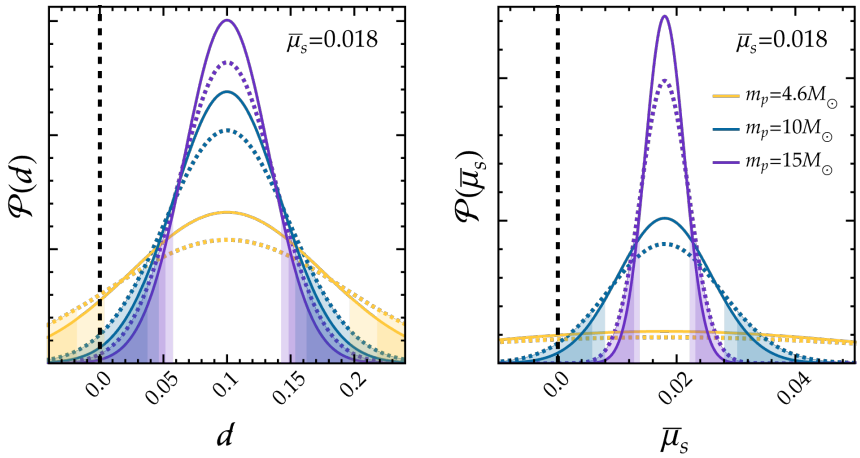

Figure 9.5. Marginal distributions for d (left plot) and μ_s (right plot). Dashed and continuous curves are relative to inspirals in which the scalar flux takes into account only the $\ell_{\rm max} = 1$ or up to $\ell_{\rm max} = 2$, respectively. The vertical lines identify the GR scenario with $d = \bar{\mu}_s = 0$.

Chapter 10

Conclusions and future prospects

The study carried out in this thesis show that Extreme Mass Ratio Inspirals represent a golden class of sources to test General Relativity in the strong field regime, and to search for new fundamental fields coupled to gravity. The peculiar orbital configuration expected for EMRIs entering the LISA band would allow to track their evolution by following tens of thousand cycles before the plunge. Continuous observations of GWs emitted during this long inspiral will eventually provide a detailed map of the binary spacetime, leading to accurate measurements of the source parameters, able to pinpoint even small departures from General Relativity. Historically, this has promoted EMRIs as a tool to probe Kerr deviations from the *primary* BH.

In this thesis we have discussed a new theoretical approach to model EMRIs in alternative gravity theories with additional fundamental scalar fields. This framework builds on a decoupling of scales which allows to disentangle GR deviations between the primary and the secondary component of the binary, with those of the massive BH being subdominant. This pushes for a change of perspective in the understanding of EMRIs beyond GR. Rather than working on GR deviations from the massive component of the binary, which can be safely described (at the leading order) by the Kerr metric, we focused on the imprint left by the extra field on the *secondary*, which carries a scalar charge able to affect the EMRIs dynamics and hence its GW emission.

We provided the first direct analysis of the capability of the space interferometer LISA to constrain the features of massless and ultra-light fields from EMRI observations, forecasting LISA measurements for the scalar charge of the secondary and for the scalar field mass.

We modeled EMRIs in a vast family of modified gravity theories belonging to two classes, depending on whether: (i) BHs satisfy no-hair theorems, such that their stationary solutions are described by the Kerr metric or, (ii) BHs are endowed with a scalar profile, i.e. they carry a scalar charge. For class (ii) we considered theories with dimensionful coupling constants α, such that (in geometrical units $G = c = 1$) $[\alpha] = (mass)^{\mathrm{n}}$ with n positive integer. In this case, deviations from GR are fully controlled by the dimensionless parameter $\zeta = \alpha/\mathrm{mass}^{\mathrm{n}}$, given by the ratio of the coupling and the BH mass.

We showed that for asymmetric binaries in both classes of theories the spacetime of the primary can be adequately described by the Kerr metric. Indeed, while case

(i) is trivial, for case (ii) the scalar charge of the primary is suppressed with respect to the one carried by the secondary at order $\mathcal{O}(q)$, with q being the binary mass ratio. This provides large simplification for the EMRI modeling, and allows to consider realistic astrophysical setups with (fast) rotating black holes. The secondary component of the binary can instead be treated as a point-particle with a given mass, carrying a non-negligible scalar charge.

Our formalism is valid for shift-symmetric theories, i.e. for massless scalars, and for more general models with massive scalars, so long we assume $\mu_s M \lesssim 1$, where μ_s and M are the scalar field and the primary BH mass, respectively.

In this framework we have developed a coherent formalism, valid at the leading order in q, which leads to a decoupled set of field's equations for the gravitational and the scalar sector. Equations for the metric tensor are identical to GR, while those for the scalar field reduce to a wave equation with a source term controlled by the scalar charge carried by the secondary. For shift-symmetric models the charge encloses all the details of the underlying theory of gravity, and universally captures deviations from GR in the EMRI dynamics, allowing to model the system in a theory-agnostic fashion. In the case of massive scalars, GR changes are also controlled by the field mass, which enters the scalar wave equation.

Moving in the background spacetime of the primary MBH, the small compact object produces gravitational and scalar perturbations, which carry energy and angular momentum away from the binary. In our approach the scalar emission adds linearly to the gravitational contribution, and acts as additional radiation-reaction term in the usual GR adiabatic scheme, driving the EMRI evolution to a faster plunge.

The extra emission leaves an imprint on the emitted gravitational waves. However, since gravitational perturbations are identical to GR, the simplifications introduced by our approach also allow to use the same waveform models derived for EMRIs in Einstein gravity, but assuming that the adiabatic evolution of the orbital elements includes the extra contribution given by the scalar fluxes. This leads to ready-to-use agnostic templates, only dependent on the scalar charge and on the scalar field mass (together with the usual binary parameters), which we have exploited for different data analysis science cases.

Hereafter we discuss the main results of each model taken into consideration.

Equatorial circular EMRIs with a massless scalar field

As a first science case we have investigated circular equatorial EMRIs around rotating black holes, assuming massless scalar fields.

Our analysis shows that the spin of the primary has a strong influence on the GW emission of the binary. Indeed, increasing the MBH rotation rate, the radius at which the secondary plunges shrinks, allowing the inspiral to reach larger frequencies, and boosting the overall energy loss. In addition, we have shown that for a fixed orbital distance the ratio between the scalar and the gravitational fluxes also increases with the spin. Assuming $a/M = 0.9$, the value of $\dot{E}_{\rm scal}/d^2$ can be as large as $\sim 11\%$ of $\dot{E}_{\rm grav}$ when the secondary sits at $r/M \sim 8$, decreasing to $\sim 3\%$ for closer distances. The spin affects all GW observables, as the accumulated phase, which also increases with a/M.

The difference in the phase evolution between EMRIs modelled with and without scalar charge suggests that LISA could be able to detect values of the scalar charge

d as small as $d \sim 10^{-3}$ for $a/M = 0.9$, which would correspond to a difference of 10^3 radians in 1 year of observation before the plunge. While such numbers are significant, the dephasing analysis only provides a preliminary figure of merit to investigate whether the scalar emission can lead to detectable effects.

We have carried out a more quantitative investigation by taking account correlations among the different parameters entering the GW signal. Analyses based on the faithfulness between GW templates computed with and without the scalar charge lowered previous bounds, showing that LISA can be able to detect $d \sim 0.005 - 0.01$ in 1 year of evolution before the merger.

Finally, we have performed a full parameter estimation using a Fisher matrix approach, which yield constraints on the scalar charge with a percentage accuracy. For a prototype EMRI with $(10^6 - 10)M_\odot$, $a/M = 0.9$ and SNR $= 150$ we obtained relative errors $\lesssim 10\%$ for $d \gtrsim 0.1$, and $\sim 20\%$ for $d = 0.05$.

Our theory-agnostic approach allows to translate agnostic constraints on the charge, to bounds on the coupling of a specific theory. We have considered as an example the shift-symmetric scalar Gauss Bonnet gravity. In this case, if the secondary object is a black hole, the relationship $d(\alpha)$ between the scalar charge and the Gauss Bonnet coupling constant is given by $\alpha \simeq 2dm_p^2 - 73d^3m_p^2/240$ [156], where m_p is the mass of the secondary. For $d = 0.05$ ($d = 0.2$) this yields $\sqrt{\alpha} = 4.67^{+0.59}_{-0.69}$ km ($\sqrt{\alpha} = 9.311^{+0.078}_{-0.079}$ km) at 90% confidence level.

Overall such results suggest that a single LISA detection may provide measurements of the scalar charge with an unprecedented level of accuracy.

Equatorial eccentric EMRIs with a massless scalar field

We have improved our model by adding astrophysical ingredients to the EMRI evolution. We first focused on the eccentricity, which is expected to play a key role in the dynamics of such systems.

Along with the gravitational/scalar energy and angular momentum fluxes, we have recomputed some of the figures of merit considered for the circular case, i.e. the difference in the accumulated phase and the faithfulness. We have explored a variety of binary configurations, with initial apastron fixed to $r_a = 11M$ and different values of the initial periastron, so that the initial eccentricity varies from $e_{\rm in} = 0$ to $e_{\rm in} \simeq 0.5$. The scalar charge has been fixed to $d = 0.01$. Our analysis shows that after $4 - 6$ months of observation, EMRI inspirals can accumulate a dephasing larger than the detectability threshold. For a given time of observation such dephasing increases for larger values of the initial eccentricity.

Furthermore, we have investigated the distinguishability between GW signals emitted by eccentric EMRIs carrying a non-vanishing scalar charge, for different values of d. We confirmed the results found for the circular orbits, finding that the eccentricity further reduces the overlap with GR templates. One year of observation in the LISA band would be enough to distinguish signals with a scalar charge as small as $d \sim 0.01$.

As a take home message, eccentricity appears to enhance the effect of the scalar emission, and its impact on the EMRI evolution.

Equatorial circular EMRIs with a massive scalar field

As a complementary study, we have investigated a more complex theoretical model, in which EMRIs evolve in the presence of a massive scalar field. As a first case study we considered circular equatorial orbits with a spinning primary.

For a fixed orbital configuration our numerical calculations show that the total scalar energy flux decreases as the mass of the field grows. Moreover, at variance with the massless case, new features emerge during the inspiral. Indeed, the scalar emission at infinity is suppressed for frequencies smaller then the field mass. More interestingly, we observed the appearance of scalar resonances, which can in principle lead to floating orbits, i.e. to configurations in which the binary stalls, dramatically changing its inspiral phase. Given that a full treatment of this phenomenom requires next to leading order calculations, we have neglected their effect on the EMRI dynamics. Therefore, our results can be considered conservative.

We have carried a dephasing analysis on an extended sample of EMRI parameters, which hints that one year of evolution can potentially lead to a simultaneous measurement of both the scalar charge and of the scalar mass. The suppression of the flux at infinity above a certain frequency leads to a rich phenomenology, with the dephasing that changes sign, namely the binary accelerates or decelerates, depending on the EMRI orbital radius. Studies based on the faithfulness confirms the phase analysis, yielding GW signals distignuishbale from GR for $\mu_s \lesssim 0.01$, within a range of charges $d = (0.05, 0.1, 0.3)$. For larger values of the scalar field mass, the suppression of the scalar emission at infinity is such to render the signal undistinguishable from its GR counterpart.

In order to investigate the simultaneous measurability of the scalar charge and the mass of the field, we have performed a Fisher study assuming EMRIs with various source parameters. We considered secondaries with $m_p = (1.4, 4.6, 10, 15)M_\odot$, carrying a scalar charge $d = 0.01$ and inspiralling around a primary with mass $M = 10^6 M_\odot$ and spin $a/M = 0.9$. We focused on ultra-light scalar fields, i.e. $\bar{\mu}_s = 0.018$ ($\simeq 2.4 \times 10^{-18}$eV) and $\bar{\mu}_s = 0.036$ ($\simeq 4.8 \times 10^{-18}$eV). This analysis shows that LISA will be potentially able to measure the charge and the scalar mass for binaries with $m_p \gtrsim 10M_\odot$ at more than 90% confidence level, with relative errors ranging between $\sim 50\%$ and $\sim 20\%$ for both μ_s and d. Interestingly, lighter secondaries, with $m_p = 1.4M_\odot$, lead both quantities to be unconstrained. As discussed above this constraints could change, and possibily improve, with the inclusion of scalar resonances.

Future prospects

The EMRI models discussed in this thesis can be improved in several directions, with the twofold goal of having a general description of (very) asymmetric sources on a wide range of orbital configurations, and to treat the largest class of GR extensions.

From an astrophysical point of view, EMRI secondaries are expected to complete eccentric and inclined orbits around the primary. Therefore, the inclusion of non-equatorial configurations is mandatory to characterise realistic binaries on generic inspirals. In this regard we are currently working on a new project which focuses to study circular inclined trajectories with a rotating primary, and a massless scalar field [179] .

Moreover, compact binaries do not evolve in vacuum, but rather in environments polluted by any form of matter and fields. The astrophysical arena in which EMRIs coalesce can modify the GW signal through a variety of effects, as gravitational drag, accretion and tidal resonances. While a coherent description of such effects in the EMRI modelling in GR is currently missing, they could provide a possible source of degeneracy with the scalar emission, which can hamper our ability to distinctively reconstruct the scalar field parameters [58, 110, 131, 180–186]. For this reason it would be desiderable to extend the model we investigated by includinge one or multiple environmental effects.

From a theoretical point of view, our adiabatic framework could be improved by considering fully-relativistic Teukolsky waveforms. However, in order to provide accurate waveforms for LISA searches and parameter estimation, the GW phase needs to be modeled by going beyond the adiabatic order, including at least all the terms up to $O(q)$, which then require self-force calculations. A recent work with post-adiabatic corrections has been provided in [117], which presented the first- and second-order perturbative fields equations and the equations of motion for the secondary object, treated as a non-spinning point particle. The case of a spinning particle have been studied in GR by [127, 187] and in scalar tensor theories by [188]. Orbital resonances, which contribute to the phase at $O(q^{-1/2})$, should also be investigated. Moreover, for ultra-light scalar fields, the appearance of additional resonances due to the scalar field mass should also be taken into account.

On the data analysis side, a fully Bayesian analysis based on Markov Chain Monte Carlo simulations, is currently under preparation [168]. Such an analysis is expected to provide further information on the degeneracies between the source parameters, and to clarify the LISA capablity to constrain the scalar field properties.

Finally, our formalism could be extended to multiple fields, couplings, and to different fields such as vector fields. The straightforward case which considers a minimal coupling with vector fields have been investigated in [189, 190].

The achievement of each future line of research presented here would represent a further step in the description of asymmetric binary system in scenarios beyond the Einstein theory and the Standard Model of Particle Physics, allowing to use asymmetric binary systems to unveil or constrain the existence of new fundamental fields that may be present in our Universe.

Appendix A

Tests on the equatorial eccentric fluxes

In this Appendix we present different checks done for the equatorial eccentric energy and angular momentum fluxes, showing the errors brought by the interpolation methods and providing comparisons between our computations and known results published in literature.

A.1 Error estimates for the interpolation method

We have tested the the method used to interpolate energy and angular momentum fluxes, by comparing values of ($\dot{E}_{\rm grav,scal}$, $\dot{L}_{\rm grav,scal}$) outside the numerical grid with those predicted by the interpolation. The percentage relative differences δ between these two quantities are shown in Table A.1 and A.2, for some orbital configurations.

e	p/M	$\dot{E}^{\rm int}_{\rm grav}$	$\dot{E}_{\rm grav}$	$\delta\%$	$\dot{E}^{\rm int}_{\rm scal}$	$\dot{E}_{\rm scal}$	$\delta\%$
0.1	4	3.625×10^{-3}	3.631×10^{-3}	0.2	1.785×10^{-4}	1.785×10^{-4}	0.008
	10	5.433×10^{-5}	5.132×10^{-5}	6	6.865×10^{-6}	6.722×10^{-6}	2
0.4	4	4.838×10^{-3}	4.848×10^{-3}	0.2	1.964×10^{-4}	1.964×10^{-4}	0.002
	10	6.576×10^{-5}	6.164×10^{-5}	7	6.705×10^{-6}	6.528×10^{-6}	3

Table A.1. Relative percentage difference between interpolated fluxes and values computed outside the grid of interpolation. The spin of the primary is fixed to $a/M = 0.9$. The superscript "int" identifies the interpolated values.

e	p/M	$\dot{L}^{\rm int}_{\rm grav}$	$\dot{L}_{\rm grav}$	$\delta\%$	$\dot{L}^{\rm int}_{\rm scal}$	$\dot{L}_{\rm scal}$	$\delta\%$
0.1	4	3.164×10^{-2}	3.169×10^{-2}	0.2	6.266×10^{-3}	6.267×10^{-3}	0.001
	10	1.659×10^{-3}	1.635×10^{-3}	1	8.679×10^{-4}	8.647×10^{-4}	0.4
0.4	4	3.377×10^{-2}	3.383×10^{-2}	0.2	5.752×10^{-3}	5.752×10^{-3}	0.0006
	10	1.576×10^{-3}	1.547×10^{-3}	2	7.227×10^{-4}	7.189×10^{-4}	0.6

Table A.2. Same as Table A.1 but for the angular momentum fluxes.

A.2 Comparison with previous results

The numerical output of our code have been tested by comparing the energy and angular momentum fluxes for the scalar and gravitational sector against known results published in literature [75, 76, 191]. In Table A.3 we provide a comparison showing the relative difference δ between the calculations of $\dot{E}_{\rm scal,grav}$ and of $\dot{L}_{\rm scal,grav}$ for different EMRI orbital set up. Moreover, in Table A.4 we also show the comparison of our results for the scalar emission on eccentric orbits with $a/M = 0$, $p = 8M$ and $e = 0.1$, with an independent computation (courtesy of N. Warburton computed using the code of [76]). For all configurations considered, our results provide a remarkable agreement with previous computations.

sector	a	p	e	$\dot{E}$	$\delta\%$	$\dot{L}$	$\delta\%$
scal - (tot)	0.9	10	0.2	2.686e-5	3e-5	8.359e-4	3e-5
scal - (tot)	0.9	10	0.5	2.468e-5	7e-1	6.296e-4	3e-4
scal - (tot)	0	10	0.2	3.213e-5	4e-5	9.626e-4	3e-5
scal - (tot)	0	10	0.5	3.329e-5	1e-3	7.845e-4	6e-4
scal - (tot)	0.2	6.15	0.4	3.427e-4	3e-2	3.926e-3	2e-2
grav - (+)	0.9	12.152	0.3731	2.737e-5	14		
grav - (+)	0.5	6	0.1	7.106e-4	2e-3	1.055e-2	2e-3
grav - (+)	0.5	6	0.2	7.785e-4	3e-4	1.085e-2	6e-5
grav - (+)	0.5	6	0.5	1.195e-3	8e-2	1.229e-2	7e-2
grav - (−)	0.5	6	0.1	-1.274e-6	1e-1	-1.882e-5	2e-3
grav - (−)	0.5	6	0.2	-1.430e-6	5e-1	-1.973e-5	2e-3
grav - (−)	0.5	6	0.5	-1.126e-6	8	-1.657e-5	3e-2

Table A.3. Comparison between the total (tot), horizon (−) and infinity (+) scalar and gravitational fluxes from previous works. The scalar fluxes are compared with [76], while the gravitational ones with [70]. For each quantity and binary configuration specified by the primary spin, the orbital eccentricity and the semi-latus rectum, we show the numerical result obtained with our code and the relative percentage difference with the literature value (when available). Note that fluxes from Ref. [76] have a global factor 4 of difference compared to our values, due to a different normalization of the scalar field.

ℓ	m	n	$\dot{E}^{(-)}$	$\delta\%$	$\dot{E}^{(+)}$	$\delta\%$
0	0	1	1.138e-8	1e-5	2.060e-8	2e-4
0	0	5	1.527e-16	4e-7	1.926e-17	2e-6
1	1	1	1.857e-8	3e-10	3.256e-7	1e-11
1	-1	1	1.073e-10	4e-10	1.981e-9	4e-12
1	1	5	1.007e-14	2e-9	5.299e-15	3e-8
1	-1	5	4.461e-22	1e-6	1.993e-18	5e-7
2	2	2	1.285e-10	1e-10	2.440e-8	1e-12
2	-2	2	3.955e-14	9e-10	2.391e-10	4e-12
2	2	10	1.755e-23	5e-5	1.842e-23	4e-4
2	-2	10	4.697e-35	4e-1	6.366e-30	2e-1
8	8	10	5.882e-26	5e-10	6.868e-18	8e-8

Table A.4. Values of the scalar energy flux at the horizon and at infinity that we obtained for different mode combinations, for a primary BH with spin $a/M = 0$, and a secondary on eccentric orbits with $p = 8M$ and $e = 0.1$. For each quantity we show the relative errors with respect to the values obtained by an independent code (Courtesy of Niels Warburton, and derived with the code developed in [76]).

Appendix B

Checks on the Fisher matrices

This Appendix provides the checks we did on the Fisher matrices for both the analysis on massless and ultra-light scalar fields. The Fisher construction require the computations of the template derivatives with respect to the EMRI parameters. We computed fully numerical derivatives through finite differences which require a careful choice of a step-size ϵ, which controls the shift for each of the waveform parameters, as explained in detail in Chapter 8.

B.1 Massless scalar field

We have performed various checks in order to assess the stability and convergence of our numerical calculations. The correlation matrix in Figure B.1 shows the maximum relative error, $|\Gamma_{kn}(\epsilon_i)/\Gamma_{kn}(\epsilon_j)-1|\times 100$, between Fisher matrices computed for different values of the spacing, where $\epsilon_{i=1,\dots 5} = (10^{-5}, 5\times10^{-6}, 10^{-6}, 5\times10^{-7}, 10^{-7})$ for the scalar charge and $\epsilon_{i=1,\dots 5} = (10^{-7}, 5\times10^{-8}, 10^{-8}, 5\times10^{-9}, 10^{-9})$ for the other parameters. Values refer to EMRIs with $d = 0.2$, although the other configurations discussed in the paper yield similar results. The Fisher matrices computed with various ϵ_i differ less than one part over 10^5.

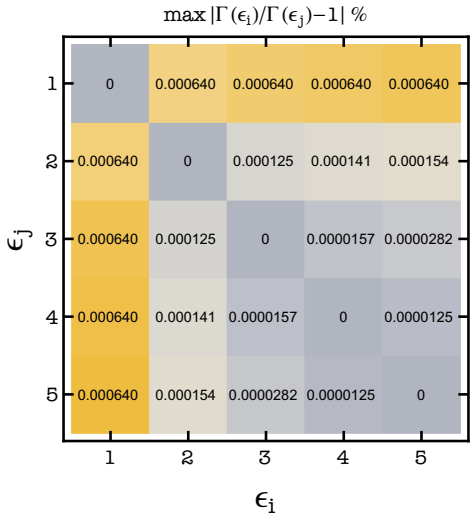

Figure B.1. Maximum relative (percentage) errors between Fisher matrices computed assuming different values of the spacing used for the numerical derivatives. The Fisher matrices have been computed for EMRIs with $d = 0.2$.

In the case of EMRIs, it is well known that computations of the Fisher matrix may lead to ill-conditioned problems, and be plagued by numerical instabilities [192, 193]. The intrinsic high sensitivity of EMRIs to small perturbations of the system reflects their ability to provide exquisite constraints on the waveform parameters and hence it is a blessing in disguise. This large amount of information is reflected on the magnitude of the elements of the Fisher matrix, although not all of them have the same size. For all the EMRI configurations analysed, the components of $\mathbf{\Gamma}$ corresponding to $(M, \mu, a/M, r_0, d)$ are always predominant with respect to the rest of the waveform parameters, with differences of several orders of magnitude. These differences lead to large condition numbers, i.e., the ratios between the largest to the smallest of the Fisher eigenvalues $\lambda_{i=1,...11}$, which in our case are of the order $\kappa = \max(\lambda_i)/\min(\lambda_i) \sim \mathcal{O}(10^{14})$. Nonetheless, the high precision computation we perform leads to stable inversion of the Fisher matrices, independent of the numerical shift. The correlation matrix in Figure B.2 shows the maximum relative error between the square root of the diagonal components of the covariance matrices, i.e., the parameter errors, computed by inverting the Fisher matrix derived with different ϵ_i, for the $d = 0.2$ case. We see from this analysis that a large fraction of errors agree with each other to well below the 1% level, and the few remaining cases feature differences of at most 1%. Correlation coefficients are also very stable, with differences smaller than 1%.

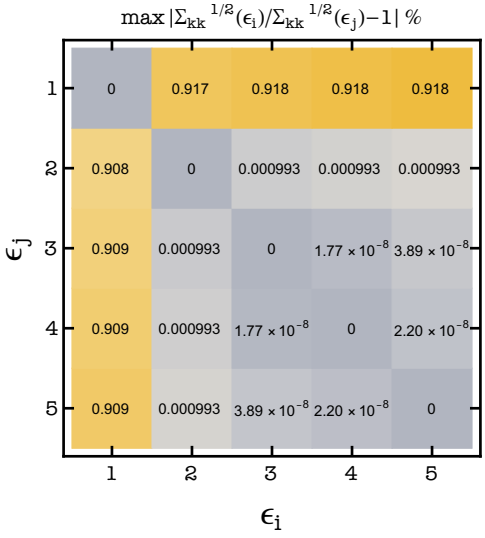

Figure B.2. Maximum relative (percentage) errors between (square root of) the diagonal components of the covariance matrices, i.e., the parameter errors, obtained with different values of the shifts considered for the numerical derivatives. We consider the same EMRI configurations shown in Figure B.1.

For the sake of completeness we show in Figure B.3 the errors on masses, spins, initial phase and radius, and on the charge, for two EMRI configurations with $d = 0.05$ and $d = 0.2$. The various panels demonstrate again the stability of our error calculations. The constraints inferred for $(M, \mu, a/M, r_0, \Phi_0)$ are also consistent with previous results on LISA parameter estimation, performed with different approaches and GW templates [127, 194, 195].

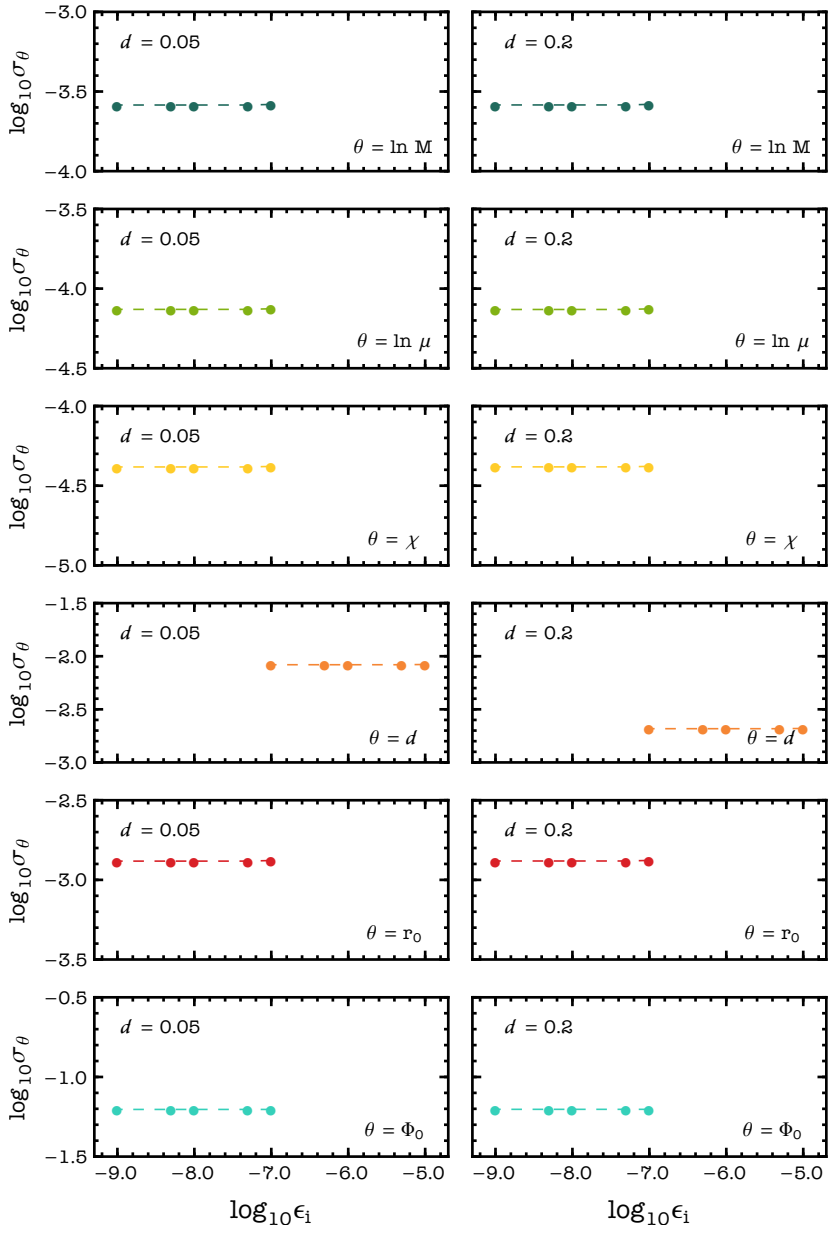

Figure B.3. Errors on the EMRI parameters as a function of the numerical shift used for partial derivatives of the Fisher matrix. We consider binaries with $d = 0.05$ (left panel) and $d = 0.2$ (right panel) with SNR of 150 as observed by LISA one year before the plunge.

We have further checked the stability of our calculations perturbing the Fisher matrices and studied the results of the inversion. Following previous work [182], we build a matrix $\mathbf{R}$ with the same dimensionality as $\mathbf{\Gamma}$, with entries randomly drawn from a uniform distribution $U \in [-10^{-3}, 10^{-3}]$. We then compute the inverse $(\mathbf{\Gamma}+\mathbf{R})^{-1}$ and determine the maximum relative error with respect to the unperturbed configuration, $\Delta\mathbf{\Gamma_R} = \max(\mathbf{\Gamma}+\mathbf{R})^{-1}/\mathbf{\Gamma}^{-1} - \mathbf{I})$. This procedure has been iterated 100 times, in order to build up statistics for the maximum error. Figure B.4 shows the cumulative distribution of $\Delta\mathbf{\Gamma_R}$ for two EMRIs with different values of the charge, as a function of the derivative spacing. The picture suggests that the calculations are very stable, as in the majority of cases more than 90% of the population has $\Delta\mathbf{\Gamma_R} \lesssim 0.1\%$. We find similar results for all the other binaries analysed.

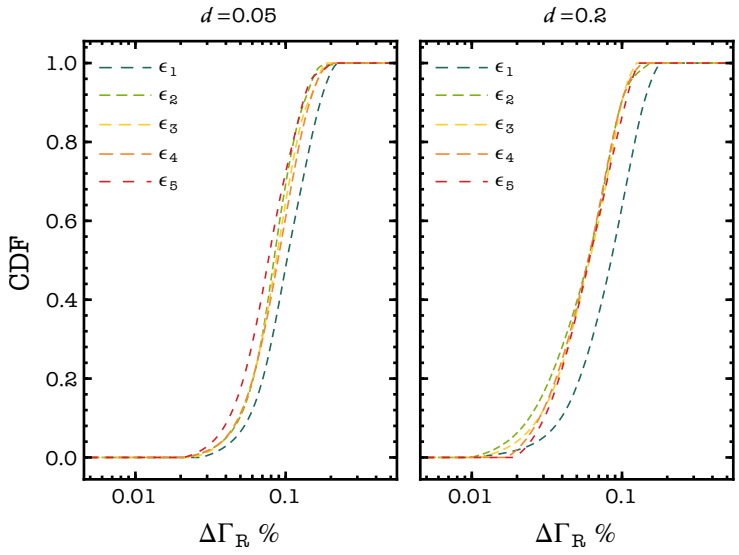

Figure B.4. Cumulative distribution for the maximum relative error between unperturbed and perturbed Fisher matrices with elements shifted by random numbers drawn from a uniform distribution. Colored curves refer to $\mathbf{\Gamma}$ computed with a different choice of the numerical derivative spacing. The uniform distribution is defined within $[-10^{-3}, 10^{-3}]$.

B.1.1 Singular values decomposition

Beside direct inversion of the Fisher matrix, we have derived the covariance on $\vec{\theta}$ also applying a truncated singular value (SVD) decomposition approach [151,196,197] on $\mathbf{\Gamma}$. Any matrix $\mathbf{A} \in \mathbb{R}^{n\times n}$ can be written in terms of its SVD as

$$\mathbf{A} = \mathbf{U}\mathbf{S}\mathbf{V}^{\mathrm{T}} \ , \tag{B.1}$$

where $\mathbf{U}$ and $\mathbf{V}$, with columns called *singular vectors*, are orthonormal matrices $\mathbf{U}\mathbf{U}^{\mathrm{T}} = \mathbf{U}^{\mathrm{T}}\mathbf{U} = \mathbf{V}^{\mathrm{T}}\mathbf{V} = \mathbf{V}\mathbf{V}^{\mathrm{T}} = \mathbf{I}$, and

$$\mathbf{S} = \mathrm{diag}(s_1, s_2, \dots s_n) \ , \tag{B.2}$$

where $\sigma_i \geq 0$ are the *singular values*. From the SVD computing the inverse of $\mathbf{A}$ is also straightforward, since

$$\mathbf{A}^{-1} = \mathbf{V}\mathbf{S}^{-1}\mathbf{U}^{\mathrm{T}} \,. \tag{B.3}$$

The singular vectors define the dimensions of the variance of the data, ordered in magnitude such that the first one is the largest, while the rank r of the initial matrix correspond to the number of non-zero σ_i. Given the form of $\mathbf{S}$ we can also recast $\mathbf{A}$ as

$$\mathbf{A} = \mathbf{U}\mathbf{S}\mathbf{V}^{\mathrm{T}} = \sum_{i=1}^{r} \sigma_i \mathbf{u}_i \mathbf{v}_i^{\mathrm{T}} \,, \tag{B.4}$$

which tells that the original matrix can be decomposed into a sum of rank-1 layers with the first contributing the most. Note that before applying the SVD, we normalize the Fisher matrices to the variance of their components, namely $\mathbf{\Gamma}/\mathbf{N}$, where $\mathbf{N} = \mathrm{diag}(\mathbf{\Gamma}) \otimes \mathrm{diag}(\mathbf{\Gamma})$, to remove differences between the parameters given by their physical scales. Although, as discussed above, the accuracy of our calculations guarantee an extremely stable inversion, we have also applied the SVD to obtain the covariance on the source parameters. In particular we have removed the singular pieces of the Fisher by zeroing values of $\mathbf{S}^{-1}$ which are very large, i.e., corresponding to small s_i. Figure B.5 shows a scree plot of the d_i normalised to the first one, for a binary with $d = 0.05$ and $d = 0.2$ (other configurations feature the same behavior, regardless of the choice of ϵ_i as well).

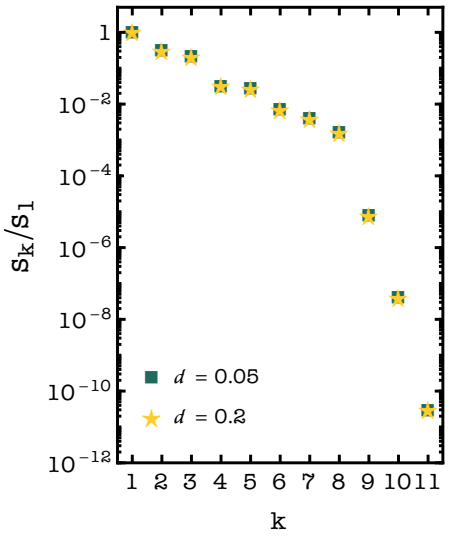

Figure B.5. Singular values normalised to their largest component for Fisher matrices with different values of the scalar charge and secondary mass. Calculations have been performed assuming $\epsilon = 10^{-5}$ for ∂_d and $\epsilon = 10^{-7}$ for the rest of the derivatives, although varying the spacing does not lead to significant changes in this figure.

The trend of the singular values exhibits a clear drop around the last component where a steep decrease in the magnitude of the s_i appears. Here we compute $\mathbf{\Gamma}^{-1}$ zeroing the last term of $\mathbf{S}^{-1}$. This procedure improves in general the errors, as it removes unmeasurable linear combinations of parameters from the Fisher matrix [151]. Indeed, as shown in Figure B.6 in which we compare relative errors on the scalar charge using direct inversion and the SVD approach, the latter yields a significant reduction of the errors. In the results shown in the main part of the paper we have reported the more conservative, direct inversion results, but the SVD

analysis suggests that LISA might be able to measure scalar charge with even higher precision.

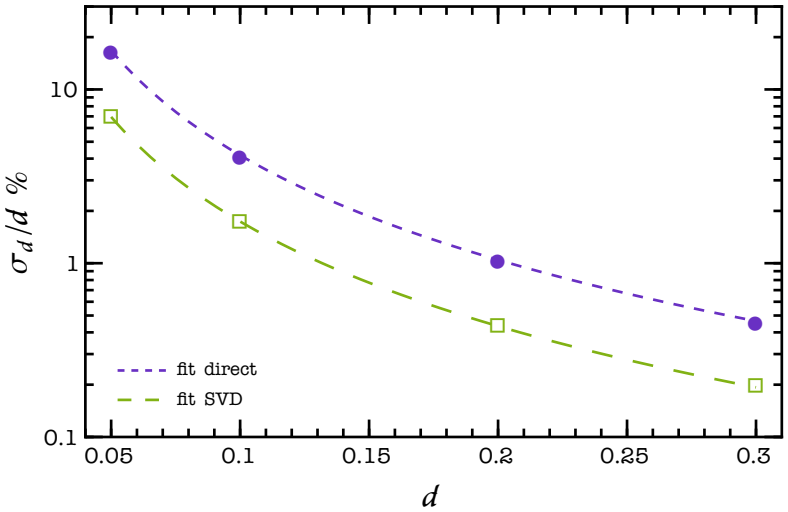

Figure B.6. Relative error on the scalar charge in the cases of direct inversion and singular value decomposition. Filled and empty dots refer to errors computed to direct inversion or truncated SVD approach. Dashed lines identify analytic fit for the errors $\sigma_d = \beta/d$, with $\beta \simeq 4.18 \times 10^{-4}$, and $\beta \simeq 1.74 \times 10^{-4}$ for the two methods considered to invert the Fisher matrices.

B.2 Massive scalar field

A summary of the stability analysis for the fisher matrices computed for ultra-light scalar fields is displayed in Fig. B.7, which shows the errors on some parameters as functions of the step-size ϵ. Moreover, to further assess the overall stability of the Fisher matrices we have studied how the errors on the parameters change under small perturbations. To this aim we have built a matrix $\mathbf{R}$ with entries randomly drawn from a uniform distribution $U \in [-10^{-3}, 10^{-3}]$. We have then computed the inverse $(\mathbf{\Gamma} + \mathbf{R})^{-1}$ and the maximum relative error with respect to the unperturbed configuration, $\Delta\mathbf{\Gamma}_\mathbf{R} = \max[(\mathbf{\Gamma}+\mathbf{R})^{-1}/[\mathbf{\Gamma}^{-1} - \mathbf{I}]$. We have iterated this procedure 100 times, to build up statistics for the maximum error. The cumulative distribution of $\Delta\mathbf{\Gamma}_\mathbf{R}$ for some of the EMRI configurations we considered is shown in Fig. B.8, proving that our calculations are extremely stable with more than 90% of the population having $\Delta\mathbf{\Gamma}_\mathbf{R} \lesssim 0.1\%$. Similar results hold for all the binaries we focused on.

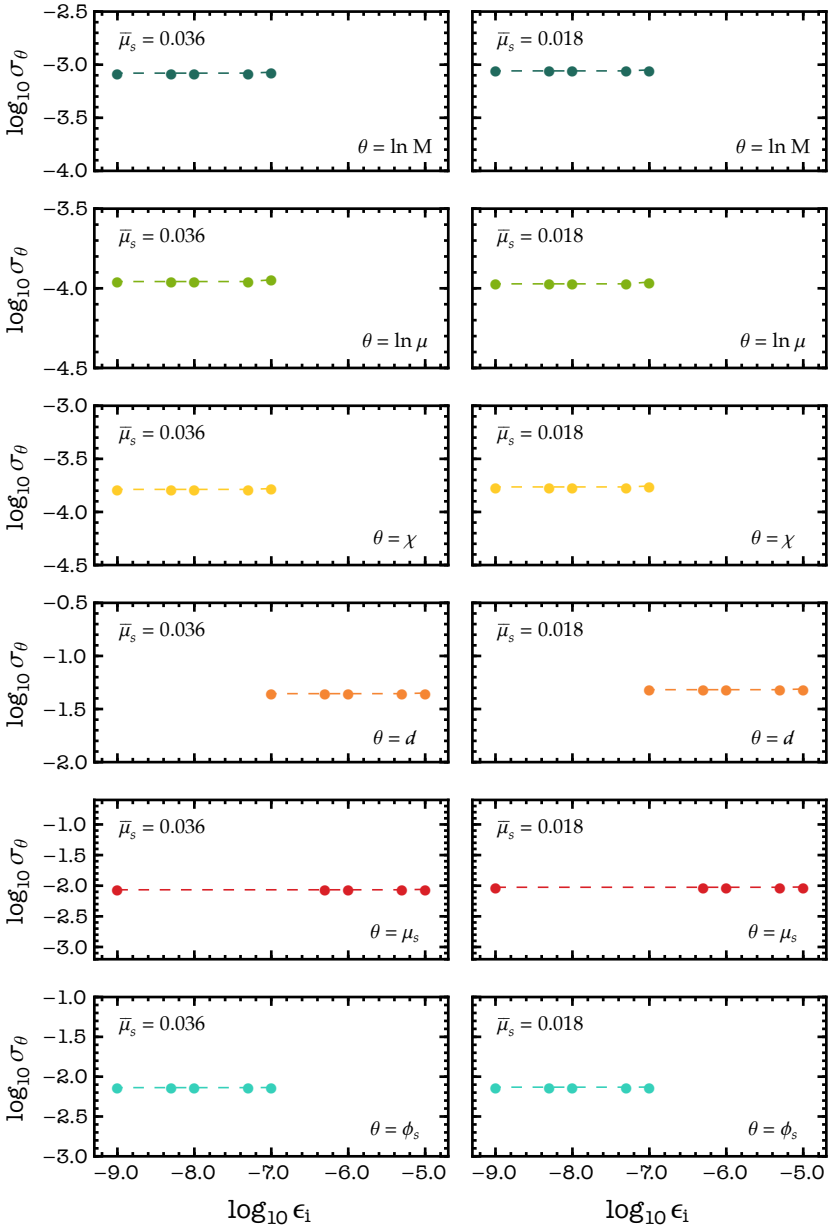

Figure B.7. Errors on the binary parameter as a function of the shift. Injected parameters are $M = 10^6 M_\odot$, $m_p = 10 M_\odot$, $a/M = 0.9$, $d = 0.1$, and $\bar{\mu}_s = 0.036$, 0.018 for the left and right column, respectively.

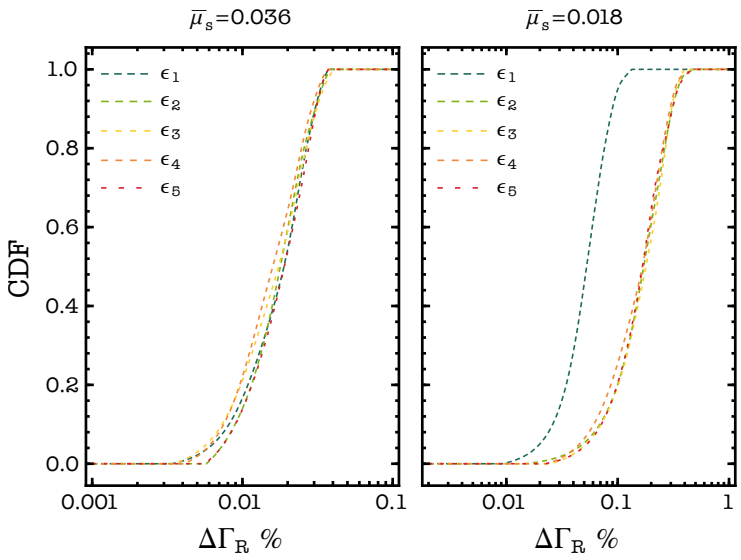

Figure B.8. Cumulative distribution for the maximum relative error between unperturbed and perturbed Fisher matrices with elements shifted by random numbers drawn from a uniform distribution. Curves with various colors refer to Fisher matrices computed with a different choice of the numerical derivative shifts, also shown in Fig. B.7. We consider EMRI with $M = 10^6 M_\odot$, $m_p = 10 M_\odot$, $a/M = 0.9$, $d = 0.1$, and $\bar{\mu}_s = 0.036$, 0.018 for the left and right column, respectively.

Bibliography

[1] LIGO Scientific, Virgo Collaboration, B. P. Abbott *et al.*, "Observation of Gravitational Waves from a Binary Black Hole Merger," *Phys. Rev. Lett.* **116** no. 6, (2016) 061102, arXiv:1602.03837 [gr-qc].

[2] VIRGO Collaboration, F. Acernese *et al.*, "Advanced Virgo: a second-generation interferometric gravitational wave detector," *Class. Quant. Grav.* **32** no. 2, (2015) 024001, arXiv:1408.3978 [gr-qc].

[3] LIGO Scientific Collaboration, J. Aasi *et al.*, "Advanced LIGO," *Class. Quant. Grav.* **32** (2015) 074001, arXiv:1411.4547 [gr-qc].

[4] KAGRA Collaboration, T. Akutsu *et al.*, "KAGRA: 2.5 Generation Interferometric Gravitational Wave Detector," *Nature Astron.* **3** no. 1, (2019) 35–40, arXiv:1811.08079 [gr-qc].

[5] LIGO Scientific, Virgo Collaboration, B. P. Abbott *et al.*, "GWTC-1: A Gravitational-Wave Transient Catalog of Compact Binary Mergers Observed by LIGO and Virgo during the First and Second Observing Runs," *Phys. Rev. X* **9** no. 3, (2019) 031040, arXiv:1811.12907 [astro-ph.HE].

[6] LIGO Scientific, Virgo Collaboration, R. Abbott *et al.*, "GWTC-2: Compact Binary Coalescences Observed by LIGO and Virgo During the First Half of the Third Observing Run," *Phys. Rev. X* **11** (2021) 021053, arXiv:2010.14527 [gr-qc].

[7] LIGO Scientific, VIRGO, KAGRA Collaboration, R. Abbott *et al.*, "GWTC-3: Compact Binary Coalescences Observed by LIGO and Virgo During the Second Part of the Third Observing Run," arXiv:2111.03606 [gr-qc].

[8] M. Punturo *et al.*, "The Einstein Telescope: A third-generation gravitational wave observatory," *Class. Quant. Grav.* **27** (2010) 194002.

[9] D. Reitze *et al.*, "Cosmic Explorer: The U.S. Contribution to Gravitational-Wave Astronomy beyond LIGO," *Bull. Am. Astron. Soc.* **51** no. 7, (2019) 035, arXiv:1907.04833 [astro-ph.IM].

[10] LISA Collaboration, P. Amaro-Seoane *et al.*, "Laser Interferometer Space Antenna," arXiv:1702.00786 [astro-ph.IM].

[11] M. Maggiore *et al.*, "Science Case for the Einstein Telescope," *JCAP* **03** (2020) 050, arXiv:1912.02622 [astro-ph.CO].

[12] E. Barausse *et al.*, "Prospects for Fundamental Physics with LISA," *Gen. Rel. Grav.* **52** no. 8, (2020) 81, arXiv:2001.09793 [gr-qc].

[13] LISA Collaboration, K. G. Arun *et al.*, "New horizons for fundamental physics with LISA," *Living Rev. Rel.* **25** no. 1, (2022) 4, arXiv:2205.01597 [gr-qc].

[14] E. Berti *et al.*, "Testing General Relativity with Present and Future Astrophysical Observations," *Class. Quant. Grav.* **32** (2015) 243001, arXiv:1501.07274 [gr-qc].

[15] E. Berti, K. Yagi, and N. Yunes, "Extreme Gravity Tests with Gravitational Waves from Compact Binary Coalescences: (I) Inspiral-Merger," *Gen. Rel. Grav.* **50** no. 4, (2018) 46, arXiv:1801.03208 [gr-qc].

[16] E. Berti, K. Yagi, H. Yang, and N. Yunes, "Extreme Gravity Tests with Gravitational Waves from Compact Binary Coalescences: (II) Ringdown," *Gen. Rel. Grav.* **50** no. 5, (2018) 49, arXiv:1801.03587 [gr-qc].

[17] L. Barack *et al.*, "Black holes, gravitational waves and fundamental physics: a roadmap," *Class. Quant. Grav.* **36** no. 14, (2019) 143001, arXiv:1806.05195 [gr-qc].

[18] S. W. Hawking, "Black holes in general relativity," *Commun. Math. Phys.* **25** (1972) 152–166.

[19] J. E. Chase, "Event horizons in static scalar-vacuum space-times," *Communications in Mathematical Physics* **19** no. 4, (Dec., 1970) 276–288.

[20] J. D. Bekenstein, "Novel ''no-scalar-hair'' theorem for black holes," *Phys. Rev. D* **51** no. 12, (1995) R6608.

[21] S. W. Hawking, "Black holes in the Brans-Dicke theory of gravitation," *Commun. Math. Phys.* **25** (1972) 167–171.

[22] T. P. Sotiriou and V. Faraoni, "Black holes in scalar-tensor gravity," *Phys. Rev. Lett.* **108** (2012) 081103, arXiv:1109.6324 [gr-qc].

[23] L. Hui and A. Nicolis, "No-Hair Theorem for the Galileon," *Phys. Rev. Lett.* **110** (2013) 241104, arXiv:1202.1296 [hep-th].

[24] T. P. Sotiriou and S.-Y. Zhou, "Black hole hair in generalized scalar-tensor gravity: An explicit example," *Phys. Rev. D* **90** (2014) 124063, arXiv:1408.1698 [gr-qc].

[25] H. O. Silva, J. Sakstein, L. Gualtieri, T. P. Sotiriou, and E. Berti, "Spontaneous scalarization of black holes and compact stars from a Gauss-Bonnet coupling," *Phys. Rev. Lett.* **120** no. 13, (2018) 131104, arXiv:1711.02080 [gr-qc].

[26] D. D. Doneva and S. S. Yazadjiev, "New Gauss-Bonnet Black Holes with Curvature-Induced Scalarization in Extended Scalar-Tensor Theories," *Phys. Rev. Lett.* **120** no. 13, (2018) 131103, arXiv:1711.01187 [gr-qc].

[27] G. Antoniou, A. Bakopoulos, and P. Kanti, "Evasion of No-Hair Theorems and Novel Black-Hole Solutions in Gauss-Bonnet Theories," *Phys. Rev. Lett.* **120** no. 13, (2018) 131102, arXiv:1711.03390 [hep-th].

[28] B. A. Campbell, N. Kaloper, and K. A. Olive, "Classical hair for Kerr-Newman black holes in string gravity," *Phys. Lett. B* **285** (1992) 199–205.

[29] S. Mignemi and N. R. Stewart, "Charged black holes in effective string theory," *Phys. Rev. D* **47** (1993) 5259–5269, arXiv:hep-th/9212146.

[30] P. Kanti, N. E. Mavromatos, J. Rizos, K. Tamvakis, and E. Winstanley, "Dilatonic black holes in higher curvature string gravity," *Phys. Rev. D* **54** (1996) 5049–5058, arXiv:hep-th/9511071.

[31] N. Yunes and L. C. Stein, "Non-Spinning Black Holes in Alternative Theories of Gravity," *Phys. Rev. D* **83** (2011) 104002, arXiv:1101.2921 [gr-qc].

[32] B. Kleihaus, J. Kunz, and E. Radu, "Rotating Black Holes in Dilatonic Einstein-Gauss-Bonnet Theory," *Phys. Rev. Lett.* **106** (2011) 151104, arXiv:1101.2868 [gr-qc].

[33] C. A. R. Herdeiro and E. Radu, "Kerr black holes with scalar hair," *Phys. Rev. Lett.* **112** (2014) 221101, arXiv:1403.2757 [gr-qc].

[34] G. Antoniou, A. Bakopoulos, and P. Kanti, "Black-Hole Solutions with Scalar Hair in Einstein-Scalar-Gauss-Bonnet Theories," *Phys. Rev. D* **97** no. 8, (2018) 084037, arXiv:1711.07431 [hep-th].

[35] S. Babak, J. Gair, A. Sesana, E. Barausse, C. F. Sopuerta, C. P. L. Berry, E. Berti, P. Amaro-Seoane, A. Petiteau, and A. Klein, "Science with the space-based interferometer LISA. V: Extreme mass-ratio inspirals," *Phys. Rev. D* **95** no. 10, (2017) 103012, arXiv:1703.09722 [gr-qc].

[36] S. A. Teukolsky, "Rotating black holes - separable wave equations for gravitational and electromagnetic perturbations," *Phys. Rev. Lett.* **29** (1972) 1114–1118.

[37] S. A. Teukolsky, "Perturbations of a rotating black hole. 1. Fundamental equations for gravitational electromagnetic and neutrino field perturbations," *Astrophys. J.* **185** (1973) 635–647.

[38] S. A. Teukolsky and W. H. Press, "Perturbations of a rotating black hole. III - Interaction of the hole with gravitational and electromagnet ic radiation," *Astrophys. J.* **193** (1974) 443–461.

[39] L. Barack and A. Pound, "Self-force and radiation reaction in general relativity," *Rept. Prog. Phys.* **82** no. 1, (2019) 016904, arXiv:1805.10385 [gr-qc].

[40] T. Hinderer and E. E. Flanagan, "Two timescale analysis of extreme mass ratio inspirals in Kerr. I. Orbital Motion," *Phys. Rev. D* **78** (2008) 064028, arXiv:0805.3337 [gr-qc].

[41] A. Pound, B. Wardell, N. Warburton, and J. Miller, "Second-Order Self-Force Calculation of Gravitational Binding Energy in Compact Binaries," *Phys. Rev. Lett.* **124** no. 2, (2020) 021101, arXiv:1908.07419 [gr-qc].

[42] N. Warburton, A. Pound, B. Wardell, J. Miller, and L. Durkan, "Gravitational-Wave Energy Flux for Compact Binaries through Second Order in the Mass Ratio," *Phys. Rev. Lett.* **127** no. 15, (2021) 151102, arXiv:2107.01298 [gr-qc].

[43] B. Wardell, A. Pound, N. Warburton, J. Miller, L. Durkan, and A. Le Tiec, "Gravitational Waveforms for Compact Binaries from Second-Order Self-Force Theory," *Phys. Rev. Lett.* **130** no. 24, (2023) 241402, arXiv:2112.12265 [gr-qc].

[44] A. Maselli, N. Franchini, L. Gualtieri, and T. P. Sotiriou, "Detecting scalar fields with Extreme Mass Ratio Inspirals," *Phys. Rev. Lett.* **125** no. 14, (2020) 141101, arXiv:2004.11895 [gr-qc].

[45] "LIGO, VIRGO AND KAGRA OBSERVING RUN PLANS website." (observing.docs.ligo.org).

[46] "Stellar Graveyard Picture." (media.ligo.northwestern.edu/gallery/mass-plot).

[47] LIGO Scientific, Virgo Collaboration, R. Abbott *et al.*, "GW190814: Gravitational Waves from the Coalescence of a 23 Solar Mass Black Hole with a 2.6 Solar Mass Compact Object," *Astrophys. J. Lett.* **896** no. 2, (2020) L44, arXiv:2006.12611 [astro-ph.HE].

[48] LIGO Scientific, Virgo Collaboration, R. Abbott *et al.*, "GW190521: A Binary Black Hole Merger with a Total Mass of $150M_{\odot}$," *Phys. Rev. Lett.* **125** no. 10, (2020) 101102, arXiv:2009.01075 [gr-qc].

[49] LIGO Scientific, Virgo Collaboration, R. Abbott *et al.*, "Properties and Astrophysical Implications of the 150 $M_{\odot}$ Binary Black Hole Merger GW190521," *Astrophys. J. Lett.* **900** no. 1, (2020) L13, arXiv:2009.01190 [astro-ph.HE].

[50] "ESA website." (esa.int).

[51] eLISA Collaboration, P. A. Seoane *et al.*, "The Gravitational Universe," arXiv:1305.5720 [astro-ph.CO].

[52] LISA Collaboration, P. A. Seoane *et al.*, "Astrophysics with the Laser Interferometer Space Antenna," *Living Rev. Rel.* **26** no. 1, (2023) 2, arXiv:2203.06016 [gr-qc].

[53] L. Ferrarese and H. Ford, "Supermassive black holes in galactic nuclei: Past, present and future research," *Space Sci. Rev.* **116** (2005) 523–624, arXiv:astro-ph/0411247.

[54] Event Horizon Telescope Collaboration, K. Akiyama *et al.*, "First M87 Event Horizon Telescope Results. I. The Shadow of the Supermassive Black Hole," *Astrophys. J. Lett.* **875** (2019) L1, arXiv:1906.11238 [astro-ph.GA].

[55] Event Horizon Telescope Collaboration, K. Akiyama *et al.*, "First Sagittarius A* Event Horizon Telescope Results. I. The Shadow of the Supermassive Black Hole in the Center of the Milky Way," *Astrophys. J. Lett.* **930** no. 2, (2022) L12.

[56] C. P. L. Berry, S. A. Hughes, C. F. Sopuerta, A. J. K. Chua, A. Heffernan, K. Holley-Bockelmann, D. P. Mihaylov, M. C. Miller, and A. Sesana, "The unique potential of extreme mass-ratio inspirals for gravitational-wave astronomy," arXiv:1903.03686 [astro-ph.HE].

[57] E. Barausse and L. Rezzolla, "The Influence of the hydrodynamic drag from an accretion torus on extreme mass-ratio inspirals," *Phys. Rev. D* **77** (2008) 104027, arXiv:0711.4558 [gr-qc].

[58] N. Yunes, B. Kocsis, A. Loeb, and Z. Haiman, "Imprint of Accretion Disk-Induced Migration on Gravitational Waves from Extreme Mass Ratio Inspirals," *Phys. Rev. Lett.* **107** (2011) 171103, arXiv:1103.4609 [astro-ph.CO].

[59] J. R. Gair, L. Barack, T. Creighton, C. Cutler, S. L. Larson, E. S. Phinney, and M. Vallisneri, "Event rate estimates for LISA extreme mass ratio capture sources," *Class. Quant. Grav.* **21** (2004) S1595–S1606, arXiv:gr-qc/0405137.

[60] P. Amaro-Seoane, J. R. Gair, M. Freitag, M. Coleman Miller, I. Mandel, C. J. Cutler, and S. Babak, "Astrophysics, detection and science applications of intermediate- and extreme mass-ratio inspirals," *Class. Quant. Grav.* **24** (2007) R113–R169, arXiv:astro-ph/0703495.

[61] C. P. L. Berry, R. H. Cole, P. Cañizares, and J. R. Gair, "Importance of transient resonances in extreme-mass-ratio inspirals," *Phys. Rev. D* **94** no. 12, (2016) 124042, arXiv:1608.08951 [gr-qc].

[62] V. Vázquez-Aceves, L. Zwick, E. Bortolas, P. R. Capelo, P. Amaro-Seoane, L. Mayer, and X. Chen, "Revised event rates for extreme and extremely large mass-ratio inspirals," *Mon. Not. Roy. Astron. Soc.* **510** no. 2, (2022) 2379–2390, arXiv:2108.00135 [astro-ph.GA].

[63] Z. Pan and H. Yang, "Formation Rate of Extreme Mass Ratio Inspirals in Active Galactic Nuclei," *Phys. Rev. D* **103** no. 10, (2021) 103018, arXiv:2101.09146 [astro-ph.HE].

[64] P. Amaro-Seoane, "Relativistic dynamics and extreme mass ratio inspirals," *Living Rev. Rel.* **21** no. 1, (2018) 4, arXiv:1205.5240 [astro-ph.CO].

[65] E. Poisson and C. M. Will, *Gravity: Newtonian, post-newtonian, relativistic*. Cambridge University Press, 2014.

[66] N. Yunes and F. Pretorius, "Fundamental Theoretical Bias in Gravitational Wave Astrophysics and the Parameterized Post-Einsteinian Framework," *Phys. Rev. D* **80** (2009) 122003, arXiv:0909.3328 [gr-qc].

[67] A. Pound and B. Wardell, "Black hole perturbation theory and gravitational self-force," arXiv:2101.04592 [gr-qc].

[68] S. A. Hughes, "The Evolution of circular, nonequatorial orbits of Kerr black holes due to gravitational wave emission," *Phys. Rev. D* **61** no. 8, (2000) 084004, arXiv:gr-qc/9910091. [Erratum: Phys.Rev.D 63, 049902 (2001), Erratum: Phys.Rev.D 65, 069902 (2002), Erratum: Phys.Rev.D 67, 089901 (2003), Erratum: Phys.Rev.D 78, 109902 (2008), Erratum: Phys.Rev.D 90, 109904 (2014)].

[69] S. A. Hughes, "Evolution of circular, nonequatorial orbits of Kerr black holes due to gravitational wave emission. II. Inspiral trajectories and gravitational wave forms," *Phys. Rev. D* **64** (2001) 064004, arXiv:gr-qc/0104041. [Erratum: Phys.Rev.D 88, 109902 (2013)].

[70] K. Glampedakis and D. Kennefick, "Zoom and whirl: Eccentric equatorial orbits around spinning black holes and their evolution under gravitational radiation reaction," *Phys. Rev. D* **66** (2002) 044002, arXiv:gr-qc/0203086.

[71] S. Drasco and S. A. Hughes, "Gravitational wave snapshots of generic extreme mass ratio inspirals," *Phys. Rev. D* **73** no. 2, (2006) 024027, arXiv:gr-qc/0509101. [Erratum: Phys.Rev.D 88, 109905 (2013), Erratum: Phys.Rev.D 90, 109905 (2014)].

[72] L. Barack, "Gravitational self force in extreme mass-ratio inspirals," *Class. Quant. Grav.* **26** (2009) 213001, arXiv:0908.1664 [gr-qc].

[73] S. Isoyama, R. Fujita, N. Sago, H. Tagoshi, and T. Tanaka, "Impact of the second-order self-forces on the dephasing of the gravitational waves from quasicircular extreme mass-ratio inspirals," *Phys. Rev. D* **87** no. 2, (2013) 024010, arXiv:1210.2569 [gr-qc].

[74] E. E. Flanagan and T. Hinderer, "Transient resonances in the inspirals of point particles into black holes," *Phys. Rev. Lett.* **109** (2012) 071102, arXiv:1009.4923 [gr-qc].

[75] N. Warburton and L. Barack, "Self force on a scalar charge in Kerr spacetime: circular equatorial orbits," *Phys. Rev. D* **81** (2010) 084039, arXiv:1003.1860 [gr-qc].

[76] N. Warburton and L. Barack, "Self force on a scalar charge in Kerr spacetime: eccentric equatorial orbits," *Phys. Rev. D* **83** (2011) 124038, arXiv:1103.0287 [gr-qc].

[77] N. Warburton, "Self force on a scalar charge in Kerr spacetime: inclined circular orbits," *Phys. Rev. D* **91** no. 2, (2015) 024045, arXiv:1408.2885 [gr-qc].

[78] D. Lovelock, "The Einstein tensor and its generalizations," *J. Math. Phys.* **12** (1971) 498–501.

[79] D. Lovelock, "The four-dimensionality of space and the einstein tensor," *J. Math. Phys.* **13** (1972) 874–876.

[80] T. P. Sotiriou, "Gravity and Scalar Fields," *Lect. Notes Phys.* **892** (2015) 3–24, arXiv:1404.2955 [gr-qc].

[81] T. Damour and G. Esposito-Farese, "Tensor multiscalar theories of gravitation," *Class. Quant. Grav.* **9** (1992) 2093–2176.

[82] Y. Fujii and K. Maeda, *The scalar-tensor theory of gravitation*. Cambridge Monographs on Mathematical Physics. Cambridge University Press, 7, 2007.

[83] V. Faraoni, *Cosmology in scalar tensor gravity*. 2004.

[84] P. G. Bergmann, "Comments on the scalar tensor theory," *Int. J. Theor. Phys.* **1** (1968) 25–36.

[85] R. V. Wagoner, "Scalar tensor theory and gravitational waves," *Phys. Rev. D* **1** (1970) 3209–3216.

[86] G. W. Horndeski, "Second-order scalar-tensor field equations in a four-dimensional space," *Int. J. Theor. Phys.* **10** (1974) 363–384.

[87] T. P. Sotiriou and V. Faraoni, "f(R) Theories Of Gravity," *Rev. Mod. Phys.* **82** (2010) 451–497, arXiv:0805.1726 [gr-qc].

[88] K. S. Stelle, "Renormalization of Higher Derivative Quantum Gravity," *Phys. Rev. D* **16** (1977) 953–969.

[89] S. Alexander and N. Yunes, "Chern-Simons Modified General Relativity," *Phys. Rept.* **480** (2009) 1–55, arXiv:0907.2562 [hep-th].

[90] T. P. Sotiriou, "Black Holes and Scalar Fields," *Class. Quant. Grav.* **32** no. 21, (2015) 214002, arXiv:1505.00248 [gr-qc].

[91] D. Doneva and S. S. Yazadjiev, "No-hair theorems for noncanonical self-gravitating static multiple scalar fields," *Phys. Rev. D* **102** no. 8, (2020) 084055, arXiv:2008.01965 [gr-qc].

[92] T. P. Sotiriou and S.-Y. Zhou, "Black hole hair in generalized scalar-tensor gravity," *Phys. Rev. Lett.* **112** (2014) 251102, arXiv:1312.3622 [gr-qc].

[93] M. Saravani and T. P. Sotiriou, "Classification of shift-symmetric Horndeski theories and hairy black holes," *Phys. Rev. D* **99** no. 12, (2019) 124004, arXiv:1903.02055 [gr-qc].

[94] R. Brito, V. Cardoso, and P. Pani, "Superradiance: New Frontiers in Black Hole Physics," *Lect. Notes Phys.* **906** (2015) pp.1–237, arXiv:1501.06570 [gr-qc].

[95] T. Damour and G. Esposito-Farèse, "Nonperturbative strong-field effects in tensor-scalar theories of gravitation," *Phys. Rev. Lett.* **70** (Apr, 1993) 2220–2223. https://link.aps.org/doi/10.1103/PhysRevLett.70.2220.

[96] A. Dima, E. Barausse, N. Franchini, and T. P. Sotiriou, "Spin-induced black hole spontaneous scalarization," *Phys. Rev. Lett.* **125** no. 23, (2020) 231101, arXiv:2006.03095 [gr-qc].

[97] D. D. Doneva, F. M. Ramazanoğlu, H. O. Silva, T. P. Sotiriou, and S. S. Yazadjiev, "Scalarization," arXiv:2211.01766 [gr-qc].

[98] M. Visser, "The Kerr spacetime: A Brief introduction," in *Kerr Fest: Black Holes in Astrophysics, General Relativity and Quantum Gravity*. 6, 2007. arXiv:0706.0622 [gr-qc].

[99] B. Carter, "Global structure of the Kerr family of gravitational fields," *Phys. Rev.* **174** (1968) 1559–1571.

[100] J. M. Bardeen, W. H. Press, and S. A. Teukolsky, "Rotating black holes: Locally nonrotating frames, energy extraction, and scalar synchrotron radiation," *Astrophys. J.* **178** (1972) 347.

[101] P. Amaro-Seoane, J. R. Gair, A. Pound, S. A. Hughes, and C. F. Sopuerta, "Research Update on Extreme-Mass-Ratio Inspirals," *J. Phys. Conf. Ser.* **610** no. 1, (2015) 012002, arXiv:1410.0958 [astro-ph.CO].

[102] J. R. Gair, S. Babak, A. Sesana, P. Amaro-Seoane, E. Barausse, C. P. L. Berry, E. Berti, and C. Sopuerta, "Prospects for observing extreme-mass-ratio inspirals with LISA," *J. Phys. Conf. Ser.* **840** no. 1, (2017) 012021, arXiv:1704.00009 [astro-ph.GA].

[103] E. Newman and R. Penrose, "An Approach to gravitational radiation by a method of spin coefficients," *J. Math. Phys.* **3** (1962) 566–578.

[104] A. Pound, "Motion of small objects in curved spacetimes: An introduction to gravitational self-force," *Fund. Theor. Phys.* **179** (2015) 399–486, arXiv:1506.06245 [gr-qc].

[105] S. A. Hughes, "Adiabatic and post-adiabatic approaches to extreme mass ratio inspiral," in *14th Marcel Grossmann Meeting on Recent Developments in Theoretical and Experimental General Relativity, Astrophysics, and Relativistic Field Theories*, vol. 2, pp. 1953–1959. 2017. arXiv:1601.02042 [gr-qc].

[106] Y. Mino, "Perturbative approach to an orbital evolution around a supermassive black hole," *Phys. Rev. D* **67** (2003) 084027, arXiv:gr-qc/0302075.

[107] W. Schmidt, "Celestial mechanics in Kerr space-time," *Class. Quant. Grav.* **19** (2002) 2743, arXiv:gr-qc/0202090.

[108] K. Glampedakis and S. Babak, "Mapping spacetimes with LISA: Inspiral of a test-body in a 'quasi-Kerr' field," *Class. Quant. Grav.* **23** (2006) 4167–4188, arXiv:gr-qc/0510057.

[109] U. Ruangsri and S. A. Hughes, "Census of transient orbital resonances encountered during binary inspiral," *Phys. Rev. D* **89** no. 8, (2014) 084036, arXiv:1307.6483 [gr-qc].

[110] P. Gupta, L. Speri, B. Bonga, A. J. K. Chua, and T. Tanaka, "Modeling transient resonances in extreme-mass-ratio inspirals," *Phys. Rev. D* **106** no. 10, (2022) 104001, arXiv:2205.04808 [gr-qc].

[111] R. Nair, S. Perkins, H. O. Silva, and N. Yunes, "Fundamental Physics Implications for Higher-Curvature Theories from Binary Black Hole Signals in the LIGO-Virgo Catalog GWTC-1," *Phys. Rev. Lett.* **123** no. 19, (2019) 191101, arXiv:1905.00870 [gr-qc].

[112] D. M. Eardley, "Observable effects of a scalar gravitational field in a binary pulsar," *Astrophysical Journal, vol. 196, Mar. 1, 1975, pt. 2, p. L59-L62.* **196** (1975) L59–L62.

[113] T. Damour and G. Esposito-Farese, "Tensor-multi-scalar theories of gravitation," *Classical and Quantum Gravity* **9** no. 9, (1992) 2093.

[114] F.-L. Julié, "Reducing the two-body problem in scalar-tensor theories to the motion of a test particle : a scalar-tensor effective-one-body approach," *Phys. Rev. D* **97** no. 2, (2018) 024047, arXiv:1709.09742 [gr-qc].

[115] F.-L. Julié, "On the motion of hairy black holes in Einstein-Maxwell-dilaton theories," *JCAP* **01** (2018) 026, arXiv:1711.10769 [gr-qc].

[116] F.-L. Julié, H. O. Silva, E. Berti, and N. Yunes, "Black hole sensitivities in Einstein-scalar-Gauss-Bonnet gravity," arXiv:2202.01329 [gr-qc].

[117] A. Spiers, A. Maselli, and T. P. Sotiriou, "Measuring scalar charge with compact binaries: High accuracy modelling with self-force," arXiv:2310.02315 [gr-qc].

[118] S. Chandrasekhar, *The mathematical theory of black holes*. 1985.

[119] E. W. Leaver, "An Analytic representation for the quasi normal modes of Kerr black holes," *Proc. Roy. Soc. Lond. A* **402** (1985) 285–298.

[120] "Black Hole Perturbation Toolkit." (bhptoolkit.org).

[121] W. R. Inc., "Mathematica, Version 12.3.1." https://www.wolfram.com/mathematica. Champaign, IL, 2021.

[122] L. C. Stein and N. Yunes, "Effective Gravitational Wave Stress-energy Tensor in Alternative Theories of Gravity," *Phys. Rev. D* **83** (2011) 064038, arXiv:1012.3144 [gr-qc].

[123] J. L. Blázquez-Salcedo, C. F. B. Macedo, V. Cardoso, V. Ferrari, L. Gualtieri, F. S. Khoo, J. Kunz, and P. Pani, "Perturbed black holes in Einstein-dilaton-Gauss-Bonnet gravity: Stability, ringdown, and gravitational-wave emission," *Phys. Rev. D* **94** no. 10, (2016) 104024, arXiv:1609.01286 [gr-qc].

[124] M. Sasaki and T. Nakamura, "Gravitational Radiation From a Kerr Black Hole. 1. Formulation and a Method for Numerical Analysis," *Prog. Theor. Phys.* **67** (1982) 1788.

[125] M. Sasaki and H. Tagoshi, "Analytic black hole perturbation approach to gravitational radiation," *Living Rev. Rel.* **6** (2003) 6, arXiv:gr-qc/0306120.

[126] A. Zenginoglu, "A Geometric framework for black hole perturbations," *Phys. Rev. D* **83** (2011) 127502, arXiv:1102.2451 [gr-qc].

[127] G. A. Piovano, R. Brito, A. Maselli, and P. Pani, "Assessing the detectability of the secondary spin in extreme mass-ratio inspirals with fully relativistic numerical waveforms," *Phys. Rev. D* **104** no. 12, (2021) 124019, arXiv:2105.07083 [gr-qc].

[128] R. A. Isaacson, "Gravitational Radiation in the Limit of High Frequency. II. Nonlinear Terms and the Ef fective Stress Tensor," *Phys. Rev.* **166** (1968) 1272–1279.

[129] S. W. Hawking and J. B. Hartle, "Energy and angular momentum flow into a black hole," *Commun. Math. Phys.* **27** (1972) 283–290.

[130] P. Gupta, B. Bonga, A. J. K. Chua, and T. Tanaka, "Importance of tidal resonances in extreme-mass-ratio inspirals," *Phys. Rev. D* **104** no. 4, (2021) 044056, arXiv:2104.03422 [gr-qc].

[131] B. Bonga, H. Yang, and S. A. Hughes, "Tidal resonance in extreme mass-ratio inspirals," *Phys. Rev. Lett.* **123** no. 10, (2019) 101103, arXiv:1905.00030 [gr-qc].

[132] A. Ori and K. S. Thorne, "The Transition from inspiral to plunge for a compact body in a circular equatorial orbit around a massive, spinning black hole," *Phys. Rev. D* **62** (2000) 124022, arXiv:gr-qc/0003032.

[133] A. Apte and S. A. Hughes, "Exciting black hole modes via misaligned coalescences: I. Inspiral, transition, and plunge trajectories using a generalized Ori-Thorne procedure," *Phys. Rev. D* **100** no. 8, (2019) 084031, arXiv:1901.05901 [gr-qc].

[134] H. Guo, Y. Liu, C. Zhang, Y. Gong, W.-L. Qian, and R.-H. Yue, "Detection of scalar fields by extreme mass ratio inspirals with a Kerr black hole," *Phys. Rev. D* **106** no. 2, (2022) 024047, arXiv:2201.10748 [gr-qc].

[135] L. Barack and C. Cutler, "LISA capture sources: Approximate waveforms, signal-to-noise ratios, and parameter estimation accuracy," *Phys. Rev. D* **69** (2004) 082005, arXiv:gr-qc/0310125.

[136] S. Babak, H. Fang, J. R. Gair, K. Glampedakis, and S. A. Hughes, "'Kludge' gravitational waveforms for a test-body orbiting a Kerr black hole," *Phys. Rev. D* **75** (2007) 024005, arXiv:gr-qc/0607007. [Erratum: Phys.Rev.D 77, 04990 (2008)].

[137] A. J. K. Chua and J. R. Gair, "Improved analytic extreme-mass-ratio inspiral model for scoping out eLISA data analysis," *Class. Quant. Grav.* **32** (2015) 232002, arXiv:1510.06245 [gr-qc].

[138] A. J. K. Chua, C. J. Moore, and J. R. Gair, "Augmented kludge waveforms for detecting extreme-mass-ratio inspirals," *Phys. Rev. D* **96** no. 4, (2017) 044005, arXiv:1705.04259 [gr-qc].

[139] A. J. K. Chua, M. L. Katz, N. Warburton, and S. A. Hughes, "Rapid generation of fully relativistic extreme-mass-ratio-inspiral waveform templates for LISA data analysis," *Phys. Rev. Lett.* **126** no. 5, (2021) 051102, arXiv:2008.06071 [gr-qc].

[140] M. L. Katz, A. J. K. Chua, L. Speri, N. Warburton, and S. A. Hughes, "Fast extreme-mass-ratio-inspiral waveforms: New tools for millihertz gravitational-wave data analysis," *Phys. Rev. D* **104** no. 6, (2021) 064047, arXiv:2104.04582 [gr-qc].

[141] C. Cutler, "Angular resolution of the LISA gravitational wave detector," *Phys. Rev. D* **57** (1998) 7089–7102, arXiv:gr-qc/9703068.

[142] T. A. Apostolatos, C. Cutler, G. J. Sussman, and K. S. Thorne, "Spin induced orbital precession and its modulation of the gravitational wave forms from merging binaries," *Phys. Rev. D* **49** (1994) 6274–6297.

[143] E. E. Flanagan and S. A. Hughes, "Measuring gravitational waves from binary black hole coalescences: 2. The Waves' information and its extraction, with and without templates," *Phys. Rev. D* **57** (1998) 4566–4587, arXiv:gr-qc/9710129.

[144] L. Lindblom, B. J. Owen, and D. A. Brown, "Model Waveform Accuracy Standards for Gravitational Wave Data Analysis," *Phys. Rev. D* **78** (2008) 124020, arXiv:0809.3844 [gr-qc].

[145] K. Chatziioannou, A. Klein, N. Yunes, and N. Cornish, "Constructing Gravitational Waves from Generic Spin-Precessing Compact Binary Inspirals," *Phys. Rev. D* **95** no. 10, (2017) 104004, arXiv:1703.03967 [gr-qc].

[146] T. Robson, N. J. Cornish, and C. Liu, "The construction and use of LISA sensitivity curves," *Class. Quant. Grav.* **36** no. 10, (2019) 105011, arXiv:1803.01944 [astro-ph.HE].

[147] P. C. Peters and J. Mathews, "Gravitational radiation from point masses in a Keplerian orbit," *Phys. Rev.* **131** (1963) 435–439.

[148] C. Zhang, Y. Gong, D. Liang, and B. Wang, "Gravitational waves from eccentric extreme mass-ratio inspirals as probes of scalar fields," *JCAP* **06** (2023) 054, arXiv:2210.11121 [gr-qc].

[149] C. Cutler and E. E. Flanagan, "Gravitational waves from merging compact binaries: How accurately can one extract the binary's parameters from the inspiral wave form?," *Phys. Rev. D* **49** (1994) 2658–2697, arXiv:gr-qc/9402014.

[150] E. Poisson and C. M. Will, "Gravitational waves from inspiraling compact binaries: Parameter estimation using second postNewtonian wave forms," *Phys. Rev. D* **52** (1995) 848–855, arXiv:gr-qc/9502040.

[151] M. Vallisneri, "Use and abuse of the Fisher information matrix in the assessment of gravitational-wave parameter-estimation prospects," *Phys. Rev. D* **77** (2008) 042001, arXiv:gr-qc/0703086.

[152] J. R. Gair, M. Vallisneri, S. L. Larson, and J. G. Baker, "Testing General Relativity with Low-Frequency, Space-Based Gravitational-Wave Detectors," *Living Rev. Rel.* **16** (2013) 7, arXiv:1212.5575 [gr-qc].

[153] L. M. Milne-Thomson, *The calculus of finite differences*. American Mathematical Soc., 2000.

[154] L. M. Milne-Thomson, *The calculus of finite differences / by L. M. Milne-Thomson*. Macmillan and Co, London, 1951.

[155] W. H. Press, S. A. Teukolsky, W. T. Vetterling, and B. P. Flannery, "Numerical Recipes in FORTRAN: The Art of Scientific Computing,".

[156] F.-L. Julié and E. Berti, "Post-Newtonian dynamics and black hole thermodynamics in Einstein-scalar-Gauss-Bonnet gravity," *Phys. Rev. D* **100** no. 10, (2019) 104061, arXiv:1909.05258 [gr-qc].

[157] S. E. Perkins, R. Nair, H. O. Silva, and N. Yunes, "Improved gravitational-wave constraints on higher-order curvature theories of gravity," *Phys. Rev. D* **104** no. 2, (2021) 024060, arXiv:2104.11189 [gr-qc].

[158] E. Barausse, N. Yunes, and K. Chamberlain, "Theory-Agnostic Constraints on Black-Hole Dipole Radiation with Multiband Gravitational-Wave Astrophysics," *Phys. Rev. Lett.* **116** no. 24, (2016) 241104, arXiv:1603.04075 [gr-qc].

[159] K. Yagi, "A New constraint on scalar Gauss-Bonnet gravity and a possible explanation for the excess of the orbital decay rate in a low-mass X-ray binary," *Phys. Rev. D* **86** (2012) 081504, arXiv:1204.4524 [gr-qc].

[160] K. Yamada, T. Narikawa, and T. Tanaka, "Testing massive-field modifications of gravity via gravitational waves," *PTEP* **2019** no. 10, (2019) 103E01, arXiv:1905.11859 [gr-qc].

[161] S. Tahura, K. Yagi, and Z. Carson, "Testing Gravity with Gravitational Waves from Binary Black Hole Mergers: Contributions from Amplitude Corrections," *Phys. Rev. D* **100** no. 10, (2019) 104001, arXiv:1907.10059 [gr-qc].

[162] H.-T. Wang, S.-P. Tang, P.-C. Li, M.-Z. Han, and Y.-Z. Fan, "Tight constraints on Einstein-dilation-Gauss-Bonnet gravity from GW190412 and GW190814," *Phys. Rev. D* **104** no. 2, (2021) 024015, arXiv:2104.07590 [gr-qc].

[163] A. Saffer and K. Yagi, "Tidal deformabilities of neutron stars in scalar-Gauss-Bonnet gravity and their applications to multimessenger tests of gravity," *Phys. Rev. D* **104** no. 12, (2021) 124052, arXiv:2110.02997 [gr-qc].

[164] Z. Lyu, N. Jiang, and K. Yagi, "Constraints on Einstein-dilation-Gauss-Bonnet gravity from black hole-neutron star gravitational wave events," *Phys. Rev. D* **105** no. 6, (2022) 064001, arXiv:2201.02543 [gr-qc]. [Erratum: Phys.Rev.D 106, 069901 (2022), Erratum: Phys.Rev.D 106, 069901 (2022)].

[165] L. Amendola, C. Charmousis, and S. C. Davis, "Solar System Constraints on Gauss-Bonnet Mediated Dark Energy," *JCAP* **10** (2007) 004, arXiv:0704.0175 [astro-ph].

[166] N. Yunes, K. Yagi, and F. Pretorius, "Theoretical Physics Implications of the Binary Black-Hole Mergers GW150914 and GW151226," *Phys. Rev. D* **94** no. 8, (2016) 084002, arXiv:1603.08955 [gr-qc].

[167] H. O. Silva, A. M. Holgado, A. Cárdenas-Avendaño, and N. Yunes, "Astrophysical and theoretical physics implications from multimessenger neutron star observations," *Phys. Rev. Lett.* **126** no. 18, (2021) 181101, arXiv:2004.01253 [gr-qc].

[168] L. Speri and et al., "Fast Emri Waveforms to test General Relativity," in preparation.

[169] J. Antoniadis *et al.*, "A Massive Pulsar in a Compact Relativistic Binary," *Science* **340** (2013) 6131, arXiv:1304.6875 [astro-ph.HE].

[170] R. Brito, S. Ghosh, E. Barausse, E. Berti, V. Cardoso, I. Dvorkin, A. Klein, and P. Pani, "Gravitational wave searches for ultralight bosons with LIGO and LISA," *Phys. Rev. D* **96** no. 6, (2017) 064050, arXiv:1706.06311 [gr-qc].

[171] T. Damour and G. Esposito-Farese, "Nonperturbative strong field effects in tensor - scalar theories of gravitation," *Phys. Rev. Lett.* **70** (1993) 2220–2223.

[172] F. M. Ramazanoğlu and F. Pretorius, "Spontaneous Scalarization with Massive Fields," *Phys. Rev. D* **93** no. 6, (2016) 064005, arXiv:1601.07475 [gr-qc].

[173] S. L. Detweiler, "KLEIN-GORDON EQUATION AND ROTATING BLACK HOLES," *Phys. Rev. D* **22** (1980) 2323–2326.

[174] J. Alsing, E. Berti, C. M. Will, and H. Zaglauer, "Gravitational radiation from compact binary systems in the massive Brans-Dicke theory of gravity," *Phys. Rev. D* **85** (2012) 064041, arXiv:1112.4903 [gr-qc].

[175] E. Berti, L. Gualtieri, M. Horbatsch, and J. Alsing, "Light scalar field constraints from gravitational-wave observations of compact binaries," *Phys. Rev. D* **85** (2012) 122005, arXiv:1204.4340 [gr-qc].

[176] W. H. Press and S. A. Teukolsky, "Floating Orbits, Superradiant Scattering and the Black-hole Bomb," *Nature* **238** (1972) 211–212.

[177] V. Cardoso, S. Chakrabarti, P. Pani, E. Berti, and L. Gualtieri, "Floating and sinking: The Imprint of massive scalars around rotating black holes," *Phys. Rev. Lett.* **107** (2011) 241101, arXiv:1109.6021 [gr-qc].

[178] N. Yunes, P. Pani, and V. Cardoso, "Gravitational Waves from Quasicircular Extreme Mass-Ratio Inspirals as Probes of Scalar-Tensor Theories," *Phys. Rev. D* **85** (2012) 102003, arXiv:1112.3351 [gr-qc].

[179] M. Della Rocca *et al.*, "in preparation,".

[180] V. Cardoso and A. Maselli, "Constraints on the astrophysical environment of binaries with gravitational-wave observations," *Astron. Astrophys.* **644** (2020) A147, arXiv:1909.05870 [astro-ph.HE].

[181] V. Cardoso, K. Destounis, F. Duque, R. Panosso Macedo, and A. Maselli, "Gravitational Waves from Extreme-Mass-Ratio Systems in Astrophysical Environments," *Phys. Rev. Lett.* **129** no. 24, (2022) 241103, arXiv:2210.01133 [gr-qc].

[182] L. Speri and J. R. Gair, "Assessing the impact of transient orbital resonances," *Phys. Rev. D* **103** no. 12, (2021) 124032, arXiv:2103.06306 [gr-qc].

[183] L. Annulli, V. Cardoso, and R. Vicente, "Stirred and shaken: Dynamical behavior of boson stars and dark matter cores," *Phys. Lett. B* **811** (2020) 135944, arXiv:2007.03700 [astro-ph.HE].

[184] O. A. Hannuksela, K. W. K. Wong, R. Brito, E. Berti, and T. G. F. Li, "Probing the existence of ultralight bosons with a single gravitational-wave measurement," *Nature Astron.* **3** no. 5, (2019) 447–451, arXiv:1804.09659 [astro-ph.HE].

[185] E. Barausse, V. Cardoso, and P. Pani, "Can environmental effects spoil precision gravitational-wave astrophysics?," *Phys. Rev. D* **89** no. 10, (2014) 104059, arXiv:1404.7149 [gr-qc].

[186] B. Kocsis, N. Yunes, and A. Loeb, "Observable Signatures of EMRI Black Hole Binaries Embedded in Thin Accretion Disks," *Phys. Rev. D* **84** (2011) 024032, arXiv:1104.2322 [astro-ph.GA].

[187] G. A. Piovano, A. Maselli, and P. Pani, "Extreme mass ratio inspirals with spinning secondary: a detailed study of equatorial circular motion," *Phys. Rev. D* **102** no. 2, (2020) 024041, arXiv:2004.02654 [gr-qc].

[188] H. Guo, C. Zhang, Y. Liu, R.-H. Yue, Y. Gong, and B. Wang, "Detecting the secondary spin with extreme mass ratio inspirals in Scalar-Tensor theory," arXiv:2305.00652 [gr-qc].

[189] C. Zhang and Y. Gong, "Detecting electric charge with extreme mass ratio inspirals," *Phys. Rev. D* **105** no. 12, (2022) 124046, arXiv:2204.08881 [gr-qc].

[190] C. Zhang, H. Guo, Y. Gong, and B. Wang, "Detecting vector charge with extreme mass ratio inspirals onto Kerr black holes," *JCAP* **06** (2023) 020, arXiv:2301.05915 [gr-qc].

[191] S. E. Gralla, J. L. Friedman, and A. G. Wiseman, "Numerical radiation reaction for a scalar charge in Kerr circular orbit," arXiv:gr-qc/0502123.

[192] E. K. Porter, "An Overview of LISA Data Analysis Algorithms," arXiv:0910.0373 [gr-qc].

[193] E. K. Porter and N. J. Cornish, "Fisher versus Bayes: A comparison of parameter estimation techniques for massive black hole binaries to high redshifts with eLISA," *Phys. Rev. D* **91** no. 10, (2015) 104001, arXiv:1502.05735 [gr-qc].

[194] E. A. Huerta and J. R. Gair, "Importance of including small body spin effects in the modelling of extreme and intermediate mass-ratio inspirals," *Phys. Rev. D* **84** (2011) 064023, arXiv:1105.3567 [gr-qc].

[195] E. A. Huerta, J. R. Gair, and D. A. Brown, "Importance of including small body spin effects in the modelling of intermediate mass-ratio inspirals. II Accurate parameter extraction of strong sources using higher-order spin effects," *Phys. Rev. D* **85** (2012) 064023, arXiv:1111.3243 [gr-qc].

[196] A. Pai and K. G. Arun, "Singular value decomposition in parametrised tests of post-Newtonian theory," *Class. Quant. Grav.* **30** (2013) 025011, arXiv:1207.1943 [gr-qc].

[197] M. Wade, J. D. E. Creighton, E. Ochsner, and A. B. Nielsen, "Advanced LIGO's ability to detect apparent violations of the cosmic censorship conjecture and the no-hair theorem through compact binary coalescence detections," *Phys. Rev. D* **88** no. 8, (2013) 083002, arXiv:1306.3901 [gr-qc].